Numerical Methods for the Estimation of the Impact of Geometric Uncertainties on the Performance of Electromagnetic Devices

Numerische Verfahren zur Bestimmung des Einflusses geometrischer Unsicherheiten auf die Leistungsfähigkeit elektromagnetischer Geräte
Zur Erlangung des akademischen Grades Doktor-Ingenieur (Dr.-Ing.)
genehmigte Dissertation von Jacopo Corno M.Sc. aus Milano, Italy
Fachbereich: Fachbereich 18 - Elektrotechnik und Informationstechnik
Tag der Einreichung: 26 June 2017, Tag der Prüfung: 26 September 2017
Darmstadt — D 17

Referent: Prof. dr. Sebastian Schöps
Korreferent: Prof. dr. Carlo de Falco
Publication: Darmstadt, 2017

TECHNISCHE
UNIVERSITÄT
DARMSTADT

GRADUATE SCHOOL
computational engineering

Numerical Methods for the Estimation of the Impact of Geometric Uncertainties on the Performance of Electromagnetic Devices
Numerische Verfahren zur Bestimmung des Einflusses geometrischer Unsicherheiten auf die Leistungsfähigkeit elektromagnetischer Geräte

Genehmigte Dissertation von Jacopo Corno M.Sc. aus Milano, Italy

Referent: Prof. dr. Sebastian Schöps
Korreferent: Prof. dr. Carlo de Falco

Tag der Einreichung: 26 June 2017
Tag der Prüfung: 26 September 2017

Darmstadt — D 17

Bitte zitieren Sie dieses Dokument als:
URN: urn:nbn:de:tuda-tuprints-urn:nbn:de:tuda-tuprints-70389
URL: http://tuprints.ulb.tu-darmstadt.de/http://tuprints.ulb.tu-darmstadt.de/id/eprint/7038

Abstract

This work addresses the application of Isogeometric Analysis to the simulation of particle accelerator cavities and other electromagnetic devices whose performance is mainly determined by their geometry. By exploiting the properties of B-Spline and Non-Uniform B-Spline basis functions, the Isogeometric approximation allows for the correct discretisation of the spaces arising from Maxwell's equations and for the exact representation of the computational domain. This choice leads to substantial improvements in both the overall accuracy and computational effort.

The suggested framework is applied to the evaluation of the sensitivity of these devices with respect to geometrical changes using Uncertainty Quantification methods and to shape optimisation processes. The particular choice of basis functions simplifies the construction of the geometry deformations significantly.

Finally, substructuring methods are proposed to further reduce the computational cost due to matrix assembly and to allow for hybrid coupling of Isogeometric Analysis and more classical Finite Element Methods. Considerations regarding the stability of such methods are addressed.

The methods are illustrated by simple numerical tests and real world device simulations with particular emphasis on particle accelerator cavities.

Zusammenfassung

Diese Arbeit befasst sich mit der Anwendung der isogeometrischen Analyse auf die Simulation von Beschleunigerkavitäten und anderen elektomagnetischen Geräten, deren Leistung hauptsächlich mit ihrer Geometrie zusammenhängt. Durch die inhärenten Strukturen der B-Spline-Basis ermöglicht der isogeometrische Ansatz eine konforme Diskretisierung der Funktionenräume, die aus den Maxwellgleichungen hervorgehen, sowie eine exakte Darstellung des Rechengebietes. Die Wahl des isogeometrischen Ansatzes führt zu nicht zu vernachlässigenden Verbesserungen von Genauigkeit und Rechenaufwand.

Mit Hilfe des Ansatzes wird, zusammen mit Methoden der Unsicherheitsquantifizierung und Formoptimierung, auch die Empfindlichkeit der Geräte bezüglich Änderungen der Geometrie untersucht. Hierbei wird die Berücksichtigung von Deformationen durch die Wahl der speziellen Basisfunktionen vereinfacht.

Letztendlich wird erläutert, wie durch Zerlegungsmethoden der Rechenaufwand beim Assemblieren der Matrizen weiter reduziert werden kann, und eine Kopplung von isogeometrischer und klassischer Numerik wird, zusammen mit Anmerkungen zur Stabilität einer solchen Hybridmethode, erläutert.

Die vorgestellten Techniken werden an einfachen numerischen Testbeispielen und industriellen Geräten illustriert, wobei der Fokus auf Beschleunigerkavitäten gerichtet ist.

Sommario

Scopo principale di questo lavoro di tesi è la simulazione dei campi elettromagnetici all'interno di dispositivi le cui prestazioni siano strettamente correlate alla loro geometria, con particolare interesse al caso delle cavità risonanti utilizzate negli acceleratori di particelle. L'Analisi Isogeometrica utilizza come funzioni di base per l'approssimazione numerica B-Spline e Non-Uniform Rational B-Spline, le cui proprietà consentono di discretizzare correttamente gli spazi funzionali derivanti dalle equazioni di Maxwell e allo stesso tempo di rappresentare esattamente il dominio computazionale. Questa scelta ha come vantaggio un sostanziale miglioramento dell'accuratezza e una riduzione del costo computazionale.

Il metodo proposto viene applicato sia al calcolo della sensitività rispetto a deformazioni della geometria utilizzando metodi di Quantificazione dell'Incertezza che a processi di ottimizzazione di forma. La scelta fatta per le funzioni di base semplifica notevolmente la costruzione delle deformazioni geometriche.

Infine, vengono introdotti metodi di sottostrutturazione del dominio al fine di ridurre ulteriormente il costo computazionale dovuto all'assemblaggio delle matrici e di consentire l'accoppiamento dell'Analisi Isogeometrica con metodi più classici quali gli Elementi Finiti. Vengono inoltre presentate alcune considerazioni riguardo la stabilità dell'accoppiamento.

I procedimenti proposti vengono illustrati sia tramite test numerici su geometrie semplici, che tramite applicazioni a dispositivi reali, in particolare alle cavità degli acceleratori di particelle.

There once was a man who I knew,
who decided to study at TU.
Now his thesis is done,
but he wants to have fun,
so I guess he'll start writing Haiku.

Contents

List of Figures

List of Tables

1 Introduction and Motivation

Have you heard of thes' accelerators?
They're made of some strange resonators.
The design's not easy,
can make you a bit queasy,
unless you've a real good simulator.

The accurate representation of the geometry of electromagnetic devices such as, for example, energy transducers, magnetrons, waveguides, antennas and particle accelerators is crucial in determining the device performance.

Let us consider, for example, the case of particle accelerators. The final goal of such devices is to transfer energy to a charged-particle beam by applying an electric field. The simplest particle accelerator one can imagine is the electrostatic accelerator in which a constant electric field is used; in this situation each particle acquires an energy equal to the product of its electric charge multiplied by the potential drop that is maintained between the ends of the accelerator. It is clear, however, that electrostatic accelerators suffer from a great limitation: the maximum energy obtainable is restricted by the potential difference, which is typically no more than a few tens of MV.

Radio Frequency (RF) accelerators are able to bypass this limitation by exciting an harmonic time-varying electric field in one or more cavity resonators. The beam of particles needs to be localised in bunches, and to be properly phased with respect to the fields so that it arrives when the field has the correct polarity for acceleration. The time variation of the field removes the restriction that the energy gain be limited by a fixed potential drop [81].

In a similar fashion to a vibrating string, whose notes are governed by its length, one needs to take into account that the field distribution and its oscillating frequency in a RF cavity are governed by Maxwell's eigenvalue problem and are strictly related to the shape of the domain. Even small deviations can have a non-negligible effect on the final performance since they may disrupt the field/beam synchronisation or deflect the flying particles on the wrong trajectory.

Another example of a device highly sensitive to its shape are the deflecting magnets used for the Stern-Gerlach experiment [86]. The goal is to generate a highly homogeneous magnetic field with a large spatial gradient in a small region between the magnetic poles. Even in this case, the field quality is mainly influenced by the geometry.

Being able to represent the domain shape exactly is then of utmost importance in achieving accurate simulation results. It is worth mentioning that, since the design of such devices is typically carried out via Computer Aided Design (CAD) software, we consider as geometrically *exact* any method that does not lose any geometrical feature during the discretisation process. The main goal of this work is the investigation of numerical methods tailored for electromagnetic applications where the representation of the device geometry and of its possible deviations is of paramount importance.

One of the main application we are interested in is the simulation of the so called TeV-Energy Superconducting Linear Accelerator (TESLA) cavities [2]. These are superconducting RF cavities used in linear accelerators for electron/positron beams. As the name suggests, LINear ACcelerators (LINACs), are devices that accelerate charged particles to very high energies along a linear structure. For certain applications, this particular class of particle accelerators presents a set of advantages over other existing technologies such as synchrotrons or cyclotrons [81, 82].

TESLA cavities are designed so that an electric field with a strong longitudinal component is oscillating at 1.3 GHz, however, even small deformations of the geometry ($\sim$ nm) can cause a shift in frequency in the kHz range, which needs to be taken into account during operation. These deformations can be due, e.g., to the electromagnetic pressure on the domain wall (Lorentz Detuning) or to manufacturing imperfections [2, 39].

State of the art solvers for the simulation of accelerator cavities mostly rely on the Finite Element Method (FEM) [66]. Typically, tetrahedral meshes are used with basis functions up to third order and the discretisation leads to solving large generalised eigenvalue problems, with millions of degrees of freedom, in order to achieve a sufficiently good accuracy.

The application of FEM presents several shortcomings. First and foremost, the polynomial maps used for the elements of the mesh are unable to exactly replicate even simple geometries such as conic sections (i.e. circles, ellipses, etc...). When the domain geometry is responsible for the quality of the solution, the meshing step is immediately introducing an error in the modelling process. Mesh refinement can reduce this error, but never truly eliminate it. Moreover, if deformations are to be applied to the device, e.g. as a result of an optimisation procedure or a sensitivity analysis, any modifications to the domain boundary requires either the movement of the mesh with an ad hoc treatment, or, in the worst case, the remeshing of the domain, which may not only be a cumbersome procedure, but can also introduce undesired noise in the solution.

A second shortcoming of FEM is the solution smoothness. Classical FEM relies on basis functions with local support in each element and returns solutions with only C^0 continuity across the element boundaries. In cavity simulation one usually deals with vacuum and fields with high regularity, thus it is desirable to use a numerical scheme that can achieve higher smoothness of the solution. This is particularly true for particle tracking applications since the low regularity of the computed electromagnetic fields introduces spurious components that may have an impact on the particle trajectories [55].

In this thesis we propose the application of Isogeometric Analysis (IGA) [34, 58]. The main idea of this method is to exploit the classes of basis functions that CAD uses for the parametrisation of the geometry for the construction of the approximation spaces for the analysis. Such basis functions are called B-Splines and Non-Uniform Rational B-Splines (NURBS) [12, 83] and generalise the polynomial FEM bases and are able to parametrise a wider set of shapes.

This choice presents several advantages. First, geometries defined via CAD are exactly represented throughout the analysis independently of the level of refinement. Moreover, albeit local, IGA basis functions have a wider support that spans multiple elements. As a consequence, the global regularity of the solution is only limited by the choice of the discretisation order ($p-1$ continuous derivatives for p-th degree basis). This higher regularity also proves to be beneficial for the convergence order with respect to the number of degrees of freedom [62]. Finally, representing both the geometry and the discrete solution using the same set of splines allows to continuously vary the basis functions with the underlying shape and avoids the introduction of numerical noise in the mesh updating procedures associated with traditional FEM.

These properties have made IGA a prolific field of research and its applications have widened from structural mechanics [3] to fluid simulation [19, 27] and fluid structure interaction [6]. For the application to electromagnetic problems, in particular, IGA shows the ability of consistently discretising complexes of differential forms [25] which is a property of great importance for achieving spectrally correct discretisation of the Maxwell differential operator [23, 24].

A couple of drawbacks need, however, to be addressed. Firstly, CAD software restrict to curves and surfaces and obtaining a trivariate volume representation for IGA to be applied often requires manual intervention. A second issue is that, although the wide support of the basis functions typically gives higher accuracy with respect to the number of degrees of freedom, which renders the system matrices smaller than in classical FEM, IGA matrices are typically denser, which might hinder the efficiency. Finally, the inherent tensor product structure makes it difficult to perform local refinement since a straightforward approach pollutes the parametrisation of the entire domain. Possible solutions of this latter problem are still subject of research; here we cite T-Splines [44, 89] and hierarchical splines [20, 53, 95].

This thesis is divided into two parts, one detailing the mathematical models and tools proposed, the second one presenting their application.

The following chapter introduces Maxwell's equations, and the derivation of the cavity resonator Boundary Value Problem (BVP); quantities of interest for accelerator cavities are defined and a model for the simulation of Lorentz detuning is proposed. Chapter 3 gives an introduction to IGA with particular focus on the spectrally correct discretisation of the spaces arising from electromagnetic problems. In the subsequent chapter we present methods for Uncertainty Quantification (UQ). An algorithm for the tracking of eigenvalues across the parameter space is also proposed. Finally, chapter 5 introduces two substructuring techniques, one based on Mortaring and the other based on the State Space Concatenation (SSC) method introduced by Flisgen et al. [48, 49]. These approaches allow for the speed up of the computations and to overcome the local refinement issues mentioned above.

The first chapter of the second part presents the simulation results for the eigenvalue computation in a TESLA cavity, its field flatness optimisation and the evaluation of the Lorentz detuning. Chapter 7 shows test examples of uncertainty quantification and the computation of the sensitivity of a TESLA cavity to the presence of eccentric cells, whose deformations are derived from real measurements. In the subsequent chapter we perform some tests to verify the validity of the substructuring methods proposed and we combine them to obtain a full cavity simulation. Finally, in chapter 9 we show the optimisation procedure of a Stern-Gerlach magnet.

To the author's best knowledge, our work proposes for the first time the application of IGA to cavity simulation showing better accuracy with respect to FEM when dealing with geometry deformations and highly regular solutions. IGA also proves beneficial when dealing with UQ and shape optimisation since the domain can be deformed with a relatively low number of control points and no remeshing noise is introduced. These contributions were previously published in [32, 33, 80] in preparation for this thesis. One final contribution is the construction of the Lagrange multiplier space for the Mortar method arising from the IGA spaces and the proof of its stability. This work is presented here and in an article currently in preparation [26].

Part I
Mathematical Tools

2 Electromagnetic Fields in RF Cavities

Do you remember the time of creation?
"Let there be light!" was the first declaration.
That sure was concise,
I'll be more precise
and introduce you to Maxwell's equations.

RF cavities play an important role in modern particle accelerators since they are responsible for the actual transfer of energy to the particle beam itself. The main idea is to excite an oscillating electromagnetic field in these cavities in such a way that a charged particle travelling along the axis is always exposed to experiencing an accelerating electric field. For velocities close to the speed of light ($\beta = v/c \approx 1$ with v the velocity of the particles and c the speed of light) this is accomplished by traversing the accelerating region in half the RF period. For particle bunches with low velocity ($\beta \ll 1$) the accelerating length will have to accommodate for the acceleration of the bunch itself along the structure.

It is clear that the synchronisation between the particle beam and the oscillating electromagnetic field is of paramount importance to achieve the desired acceleration. Since both the frequency and the shape of such a field are strictly related to the cavity geometry, we are interested in the study and quantification of how even small deformations can affect the device performance.

The structure of the chapter is as follows: first we introduce the fundamental laws of electromagnetism, with particular attention to the eigenvalue problem arising in structures such as waveguides and resonating cavities. A closed form solution for the cylindrical cavity is given. In the second and third sections, we focus on standing-wave RF cavities and define some of the quantities of interest that characterise them. These figures of merit allow for the comparison of different cavities both in terms of the choice of the material and of their shape. In section 2.4 the geometry of the TESLA cavity that is the main focus of this work is presented. Finally we will discuss the effects of deformations on the cavities' eigenmodes and the model adopted to study the particular case of Lorentz detuning.

2.1 Maxwell's Equations

The fundamental macroscopic laws of classical electromagnetism involve four vector functions of position $\mathbf{r} \in \mathbb{R}^3$ and time $t \in \mathbb{R}$ denoted by $\mathbf{E}$ (electric field), $\mathbf{D}$ (electric displacement), $\mathbf{H}$ (magnetic field) and $\mathbf{B}$ (magnetic induction). These fields arise in the presence of static electric charges, whose distribution is given by the density function ρ, and flow of electric charges, i.e. currents, described by the vector density function **J**.

The equations relating these quantities were formulated during the XIX century by various scientists and collected by James Clerk Maxwell in 1861. Their modern differential form is given by:

$$\frac{\partial \mathbf{B}}{\partial t} + \nabla \times \mathbf{E} = 0 \tag{2.1a}$$

$$\nabla \cdot \mathbf{D} = \rho \tag{2.1b}$$

$$\frac{\partial \mathbf{D}}{\partial t} - \nabla \times \mathbf{H} = -\mathbf{J} \tag{2.1c}$$

$$\nabla \cdot \mathbf{B} = 0. \tag{2.1d}$$

Equation (2.1a) is Faraday's law which gives the relation between the time variation of the magnetic induction field and the circulation of the electric field. Gauß' law (2.1b) gives the effect of the charge density on the electric displacement. Relation (2.1c) is due to Ampère and Maxwell and defines the effect of transport and displacement currents on the circulation of the magnetic field. Finally, (2.1d) expresses the fact that no isolated magnetic charges have been observed in nature. The divergence conditions (2.1b)-(2.1d) are consequences of the fundamental field equations (2.1a) and (2.1c), as long as charge conservation is assumed [71, chapter 1].

Equations (2.1) needs to be completed by two constitutive laws that relate **E** and **H** to **D** and **B**, respectively. These laws depend on the properties of the materials filling the domain where the electromagnetic field is computed. In the easiest case one has two linear equations of the form:

$$\mathbf{D} = \varepsilon \mathbf{E} + \mathbf{P} \tag{2.2a}$$

$$\mathbf{B} = \mu (\mathbf{H} + \mathbf{M}) \tag{2.2b}$$

where ε and μ can be two positive, bounded, scalar functions of position (isotropic materials) or two tensor valued functions of position (anisotropic materials). Quantities **P** and **M** are the electric polarisation and the magnetisation respectively and are given by the electric dipoles and magnetic dipoles that the fields generate on the molecular level.

In Ohmic conductors an additional constitutive relation may be introduced, Ohm's law, relating the current density **J** to the electric field **E** via the material conductivity σ:

$$\mathbf{J} = \sigma \mathbf{E} + \mathbf{J}_s \tag{2.3}$$

where $\sigma = \sigma(\mathbf{r}) \geq 0$ and the vector function $\mathbf{J}_s$ describes the current density generated by a given source. Regions where $\sigma > 0$ are called conductors, while if $\sigma = 0$ the material is called dielectric.

In most accelerator cavities applications, and in the remainder of this thesis unless otherwise specified, the computational domain is restricted to vacuum so that $\sigma = 0$ and the material properties reduce to the scalar constants ε_0, the electric permittivity of free space, and μ_0, the magnetic permeability of free space. Furthermore, we can disregard **P** and **M** from the constitutive laws (2.2).

The final version of the first order Maxwell system in vacuum is given by:

$$\mu_0 \frac{\partial \mathbf{H}}{\partial t} + \nabla \times \mathbf{E} = 0 \tag{2.4a}$$

$$\nabla \cdot \mathbf{E} = \frac{\rho}{\varepsilon_0} \tag{2.4b}$$

$$\varepsilon_0 \frac{\partial \mathbf{E}}{\partial t} - \nabla \times \mathbf{H} = -\mathbf{J} \tag{2.4c}$$

$$\nabla \cdot \mathbf{H} = 0, \tag{2.4d}$$

where we have used the constitutive relations (2.2) to express everything in terms of **E** and **H** only.

To introduce proper boundary conditions, it is necessary to consider the situation in which the material parameters are not smooth, i.e. when a surface Γ separates two homogeneous media from each other: the constitutive parameters ε and μ are no longer continuous but piecewise continuous with finite jumps on Γ. In particular, it is straightforward to see [71, chapter 1] that the normal component of **E** is discontinuous at an abrupt change in ε and only the tangential continuity is ensured. Similarly, the normal component of **H** is discontinuous at an abrupt change in μ. These relations carries over to the definition of the boundary conditions that are commonly used in electromagnetic boundary value problems, where only the part of the vector field that is tangent to the boundary is specified. In the case of a Perfect Electric Conducting (PEC) boundary condition, since the electric field inside a perfect conductor is 0, we impose

$$\mathbf{E} \times \mathbf{n} = 0, \tag{2.5}$$

with **n** the outward normal to the domain of interest, while for a Perfect Magnetic Conducting (PMC) boundary condition we obtain

$$\mathbf{H} \times \mathbf{n} = 0. \tag{2.6}$$

Since no real material behaves as a perfect magnetic conductor, this condition is often employed as a symmetry condition.

Any numerical scheme for the approximation of Maxwell's equations in the presence of different materials must take into account these jump conditions. Furthermore, in the case of cavity simulation, since only vacuum is present in the computational domain, the electromagnetic field is globally smooth and a discretisation scheme that is able to guarantee the high regularity of the solution is desirable.

2.1.1 Curl-Curl and Wave Equation

In order to solve system (2.4), it is common to transform the set of first-order differential equations into a second-order equation with either **E** or **H** as the unknown. This is achieved by taking the **curl** of (2.4a) and substituting it into (2.4c). The resulting formula is the so called *curl-curl equation*:

$$\nabla \times \nabla \times \mathbf{E} = -\varepsilon_0 \mu_0 \frac{\partial^2 \mathbf{E}}{\partial t^2} - \mu_0 \frac{\partial \mathbf{J}}{\partial t}, \tag{2.7}$$

which is constrained by the divergence condition (2.4b).

By recalling the vector identity

$$\nabla \times \nabla \times \mathbf{v} = \nabla (\nabla \cdot \mathbf{v}) - \Delta \mathbf{v}, \tag{2.8}$$

and assuming a homogeneous charge free domain ($\nabla \cdot \mathbf{E} = 0$) one obtains the *wave equation* for the electric field:

$$\Delta \mathbf{E} = \varepsilon_0 \mu_0 \frac{\partial^2 \mathbf{E}}{\partial t^2} + \frac{1}{\varepsilon_0} \nabla \rho + \mu_0 \frac{\partial \mathbf{J}}{\partial t}, \tag{2.9}$$

which is a hyperbolic Partial Differential Equation (PDE). Similar expressions to (2.7) and (2.9) can be obtained for the magnetic field strength **H**.

Equation (2.9) is often used for analytical computations since it allows for easy separation of variables while numerical schemes usually solve the curl-curl equation which carries more information on the field discontinuity at material interfaces. As it is shown in the following part of the thesis, care must be taken in the discretisation of such a problem.

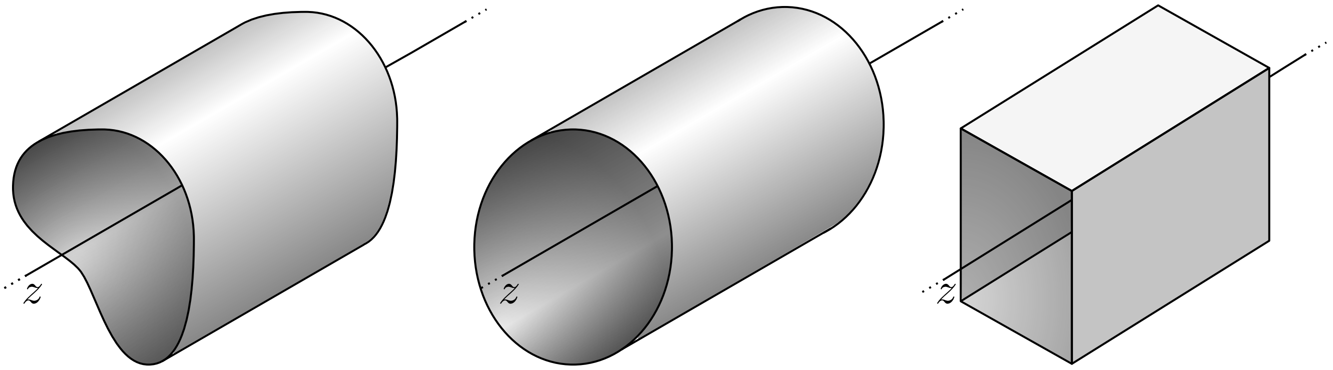

Figure 2.1: Waveguide structures with longitudinally uniform cross sections Γ_{wg}. From left to right: a generic waveguide, a circular waveguide and a rectangular waveguide.

One final, important, simplification can be performed in the case of slowly varying fields and absence of charges. Given (2.9), we discard the second time derivative of $\mathbf{E}$ and set $\rho = 0$ to get

$$\Delta \mathbf{E} = \mu_0 \frac{\partial \mathbf{J}}{\partial t}. \tag{2.10}$$

Equation (2.10) is integrated in time and we introduce the vector potential $\mathbf{A}^*$, with $\nabla \cdot \mathbf{A}^* = 0$, such that

$$\mathbf{E} = -\frac{\partial \mathbf{A}^*}{\partial t}. \tag{2.11}$$

This allows us to write the Poisson problem

$$-\Delta \mathbf{A}^* = \mu_0 \mathbf{J}, \tag{2.12}$$

which is usually referred to as the magnetostatic problem with Coulomb gauge [61, section 5.4].

2.1.2 Electromagnetic Field in a Waveguide

We consider the solution of Maxwell's equation in a waveguide structure, filled with vacuum, with a constant cross section Γ_{wg}. We assume that the boundary surfaces are made of a perfectly conducting material, and that the waveguide is oriented so that its axis corresponds to the z axis (see Fig. 2.1).

It is convenient to restate Maxwell's equations in time-harmonic form. Introducing the angular frequency $\omega \geq 0$, the electromagnetic fields are said to be time-harmonic if they can be expressed as:

$$\begin{aligned} \mathbf{E}(\mathbf{r}, t) &= \mathscr{R}\left\{\underline{\mathbf{E}}(\mathbf{r})\, e^{-\imath\omega t}\right\} \\ \mathbf{H}(\mathbf{r}, t) &= \mathscr{R}\left\{\underline{\mathbf{H}}(\mathbf{r})\, e^{-\imath\omega t}\right\}, \end{aligned} \tag{2.13}$$

where $\mathscr{R}\{\cdot\}$ denotes the real part of the complex expression it is applied to. $\underline{\mathbf{E}}$ and $\underline{\mathbf{H}}$ are complex valued vector functions of position only (phasor fields).

By substituting (2.13) into (2.9) and assuming absence of excitations, the governing equations inside the domain simplify into the time-harmonic wave equation

$$\Delta \underline{\mathbf{E}} + \frac{\omega^2}{c^2} \underline{\mathbf{E}} = 0 \tag{2.14a}$$

$$\Delta \underline{\mathbf{H}} + \frac{\omega^2}{c^2} \underline{\mathbf{H}} = 0, \tag{2.14b}$$

where we have introduced the speed of light in vacuum $c = 1/\sqrt{\varepsilon_0 \mu_0}$. Furthermore, given the symmetry of the problem and searching for propagating (k real) and evanescent (k imaginary) modes, we can further specify the spatial dependency in the z direction to be harmonic as well and write

$$\begin{aligned}\underline{\mathbf{E}}(\mathbf{r}) &= \underline{\mathbf{E}}(x,y)e^{\pm \imath k z}\\ \underline{\mathbf{H}}(\mathbf{r}) &= \underline{\mathbf{H}}(x,y)e^{\pm \imath k z},\end{aligned} \tag{2.15}$$

where k is, in general, a complex wave number and the ± sign depends on the direction of the travelling wave. Relations (2.15) can be used into (2.14) to obtain a two dimensional problem of the form

$$\Delta_\perp \underline{\mathbf{E}}(x,y) + \left(\frac{\omega^2}{c^2} - k^2\right)\underline{\mathbf{E}}(x,y) = 0 \tag{2.16a}$$

$$\Delta_\perp \underline{\mathbf{H}}(x,y) + \left(\frac{\omega^2}{c^2} - k^2\right)\underline{\mathbf{H}}(x,y) = 0. \tag{2.16b}$$

Here, $\Delta_\perp$ indicates the transverse Laplace operator

$$\Delta_\perp \mathbf{v}(x,y) = \Delta \mathbf{v}(x,y) - \frac{\partial^2}{\partial z^2}\mathbf{v}(x,y). \tag{2.17}$$

It is straightforward to see [61, chapter 8] that the problem can be solved independently for the longitudinal component $\underline{E}_z$ and for the transverse field $\underline{\mathbf{E}}_\perp = (\mathbf{e}_z \times \underline{\mathbf{E}}) \times \mathbf{e}_z$. The longitudinal components of the electric and magnetic fields can be obtained by solving the scalar Laplace equation with appropriate boundary conditions on $\partial\Omega$ ($\underline{E}_z = 0$, $\nabla \underline{H}_z \cdot \mathbf{n} = 0$).

The solution can be expressed as the superposition of an infinite number of waveguide modes

$$\underline{\mathbf{E}}(\mathbf{r}) = \sum_{i=1}^{\infty}\left(\alpha_i(z)\boldsymbol{\varphi}_i + \mathbf{e}_z \underline{E}_{z,i}(\mathbf{r})\right) \tag{2.18}$$

where the $\boldsymbol{\varphi}_i = \boldsymbol{\varphi}_i(x,y)$ solely depend on the transverse spatial coordinates. An analogous expression can be obtained for the magnetic field

$$\underline{\mathbf{H}}(\mathbf{r}) = \sum_{i=1}^{\infty}\left(\mathbf{e}_z \times \beta_i(z)\boldsymbol{\varphi}_i + \mathbf{e}_z \underline{H}_{z,i}(\mathbf{r})\right). \tag{2.19}$$

Given their physical units, α_i and β_i can be referred to as *modal voltages* and *modal currents* [47].

The vector functions $\boldsymbol{\varphi}_i$ are nothing else but the eigenfunctions of the transverse Laplace operator $\Delta_\perp$ on the cross section Γ_{wg}

$$\begin{aligned}\Delta_\perp \boldsymbol{\varphi}_i + \gamma_i^2 \boldsymbol{\varphi}_i &= 0 \quad \text{in } \Gamma_{\text{wg}}\\ \boldsymbol{\varphi}_i \times \mathbf{n} &= 0 \quad \text{on } \partial\Gamma_{\text{wg}},\end{aligned} \tag{2.20}$$

with $\gamma_i^2 = \omega^2/c^2 - k_i^2$. Problem (2.20) has an infinite number of solutions which constitutes an orthogonal set of basis functions on Γ_{wg} that can be sorted in ascending order according to their separation constants ($\gamma_1 \leq \gamma_2 \leq \gamma_3 \leq \ldots$).

For a given angular frequency ω, the waveguide number k is determined for each mode i:

$$k_i^2 = \frac{\omega^2}{c^2} - \gamma_i^2. \tag{2.21}$$

We define the cutoff frequency of mode i as

$$\omega_{\text{co}} = c\gamma_i, \tag{2.22}$$

and write the wave number as

$$k_i = \frac{\sqrt{\omega^2 - \omega_{\text{co}}^2}}{c}. \tag{2.23}$$

We note that for $\omega > \omega_{\text{co}}$, the wave number k_i is real which, in turn, means that waves of the i mode can propagate in the structure. Frequencies below the cutoff cannot propagate and are called *evanescent modes*.

In some particular cases, the modes φ_i can be computed analytically. For a rectangular waveguide of dimensions a and b, for example, there exists two sets of solutions [61, chapter 8] - [57, chapter 2]

$$\varphi_{\text{TE}}(x,y) = C_{\text{TE}} \begin{bmatrix} -\frac{n\pi}{b}\cos\left(\frac{m\pi}{a}x\right)\sin\left(\frac{n\pi}{b}y\right) \\ \frac{m\pi}{a}\sin\left(\frac{m\pi}{a}x\right)\cos\left(\frac{n\pi}{b}y\right) \end{bmatrix} \qquad m,n \geq 0,\ m+n > 0 \tag{2.24a}$$

$$\varphi_{\text{TM}}(x,y) = C_{TM} \begin{bmatrix} \frac{m\pi}{a}\cos\left(\frac{m\pi}{a}x\right)\sin\left(\frac{n\pi}{b}y\right) \\ \frac{n\pi}{b}\sin\left(\frac{m\pi}{a}x\right)\cos\left(\frac{n\pi}{b}y\right) \end{bmatrix} \qquad m,n \geq 1, \tag{2.24b}$$

with the corresponding eigenvalues

$$\lambda = \frac{c}{2\pi}\sqrt{\left(\frac{m\pi}{a}\right)^2 + \left(\frac{n\pi}{b}\right)^2}. \tag{2.25}$$

C_{TE} and C_{TM} are scaling constants that can be chosen, e.g., to ensure orthonormality of the eigenbasis. The two sets separate the solutions into Transverse Magnetic (TM) and Transverse Electric (TE) modes, according to the behaviour of the electric or magnetic field in the longitudinal direction. In particular we identify the modes as [61, chapter 8]:

$$\begin{array}{lll} \text{Transverse Magnetic (TM) :} & H_z = 0 & E_z|_S = 0 \\ \text{Transverse Electric (TE) :} & E_z = 0 & \left.\frac{\partial H_z}{\partial n}\right|_S = 0 \end{array}$$

where S indicates the boundary of the waveguide. Finally, the eigenmodes are further classified by the two indices corresponding to their horizontal (m) and vertical (n) extrema (or zero crossings) distribution.

In an analogous way we introduce the analytical solutions of the eigenvalue problem (2.20) in a circle of radius R. In polar coordinates (r,θ) the TE modes can be expressed as [57, chapter 3] - [99]

$$\varphi_{\text{TE}}^{(1)}(r,\theta) = C_{\text{TE}} \begin{bmatrix} \frac{mR^2}{\chi'_{mn} r} \mathrm{J}_m\left(\frac{\chi'_{mn} r}{R}\right)\sin(m\theta) \\ \frac{R}{\chi'_{mn}} \mathrm{J}'_m\left(\frac{\chi'_{mn} r}{R}\right)\cos(m\theta) \end{bmatrix} \tag{2.26a}$$

$$\varphi_{\text{TE}}^{(2)}(r,\theta) = C_{\text{TE}} \begin{bmatrix} -\frac{mR^2}{\chi'_{mn} r} \mathrm{J}_m\left(\frac{\chi'_{mn} r}{R}\right)\cos(m\theta) \\ \frac{R}{\chi'_{mn}} \mathrm{J}'_m\left(\frac{\chi'_{mn} r}{R}\right)\sin(m\theta) \end{bmatrix} \tag{2.26b}$$

and the TM ones as

$$\varphi_{\mathrm{TM}}^{(1)}(r,\theta) = C_{\mathrm{TM}} \begin{bmatrix} -\dfrac{R}{\chi_{mn} r} \mathrm{J}_m'\left(\dfrac{\chi_{mn} r}{R}\right)\cos(m\theta) \\ \\ \dfrac{mR^2}{\chi_{mn} r} \mathrm{J}_m\left(\dfrac{\chi_{mn} r}{R}\right)\sin(m\theta) \end{bmatrix} \tag{2.27a}$$

$$\varphi_{\mathrm{TM}}^{(2)}(r,\theta) = C_{\mathrm{TM}} \begin{bmatrix} -\dfrac{R}{\chi_{mn}} \mathrm{J}_m'\left(\dfrac{\chi_{mn} r}{R}\right)\sin(m\theta) \\ \\ -\dfrac{mR^2}{\chi_{mn} r} \mathrm{J}_m\left(\dfrac{\chi_{mn} r}{R}\right)\cos(m\theta) \end{bmatrix} \tag{2.27b}$$

with $m \geq 0$ and $n > 0$. The function $\mathrm{J}_m(\cdot)$ is the Bessel function of first kind of order m and $\mathrm{J}_m'(\cdot)$ is its derivative; the values χ_{mn} and χ_{mn}' identify the n-th zero of the m-th Bessel function and of the derivative of the m-th Bessel function respectively.

In circular waveguides the azimuthal index m is also used to divide the spectrum into monopole modes $(m = 0)$, dipole modes $(m = 1)$, quadrupole modes $(m = 2)$ and so on. With the exception of the monopole modes, all the other modes exist in two polarisations and this is expressed in the superscripts $\varphi^{(1)}$ or $\varphi^{(2)}$ in equations (2.26)-(2.27). The first eight modes in the unit circle are depicted in Figure 2.2.

2.1.3 Cavity Resonator

Following [71], from now on, let us consider a domain Ω open, bounded and simply connected representing the resonant cavity. Furthermore we assume that Ω is a Lipschitz polyhedron [71, chapter 3] and that the cavity walls are made of superconducting material, i.e. they can be considered as lossless, source-free, closed structures where the electromagnetic fields resonate with specific eigenmodes.

Since in accelerator cavities no currents are applied and no charges are present, by using time-harmonic relations (2.13), we can write the final formulation of Maxwell's equations in a RF cavity as

$$\nabla \times \nabla \times \underline{\mathbf{E}} = \varepsilon_0 \mu_0 \omega^2 \underline{\mathbf{E}} \qquad \text{in } \Omega \tag{2.28a}$$

$$\nabla \cdot \underline{\mathbf{E}} = 0 \qquad \text{in } \Omega \tag{2.28b}$$

$$\underline{\mathbf{E}} \times \mathbf{n} = 0 \qquad \text{on } \partial\Omega. \tag{2.28c}$$

On the cavity walls a PEC boundary condition (2.28c) is imposed which prescribes zero tangential electric field on the conducting walls.

In real cavities even superconducting materials have a non-zero surface resistance, albeit small compared to a normal metal. As a consequence of this a time-varying current is generated in a thin layer at the wall boundary (the so called *skin depth*) proportional to the tangential magnetic field that manages to penetrate the wall. This current, in turn, leads to power dissipation. To take into account this effect, more complicated boundary conditions than (2.28c) have to be considered, e.g. Surface Impedance Boundary Condition (SIBC) [71, chapter 1],[78, chapter 4].

The solution of (2.28) leads to an infinite set of real valued angular frequencies ω_n, with $0 < \omega_1 \leq \omega_2 \leq \cdots \leq \infty$, and a corresponding set of eigenfunctions $\underline{\mathbf{E}}_n$.

A particular type of RF cavities is the one obtained by closing a waveguide-like structure with two metallic end plates at a distance L between each other. The reflections of the fields at both ends generate standing waves which must fulfil the PEC boundary conditions. Explicitly, one gets [61, chapter 8] - [78, chapter 2]:

$$\underline{E}_z = \varphi(x,y)\cos\left(\frac{p\pi}{L}z\right) \qquad p \geq 0 \quad \text{(TM modes)} \tag{2.29}$$

$$\underline{H}_z = \varphi(x,y)\sin\left(\frac{p\pi}{L}z\right) \qquad p \geq 1 \quad \text{(TE modes)}. \tag{2.30}$$

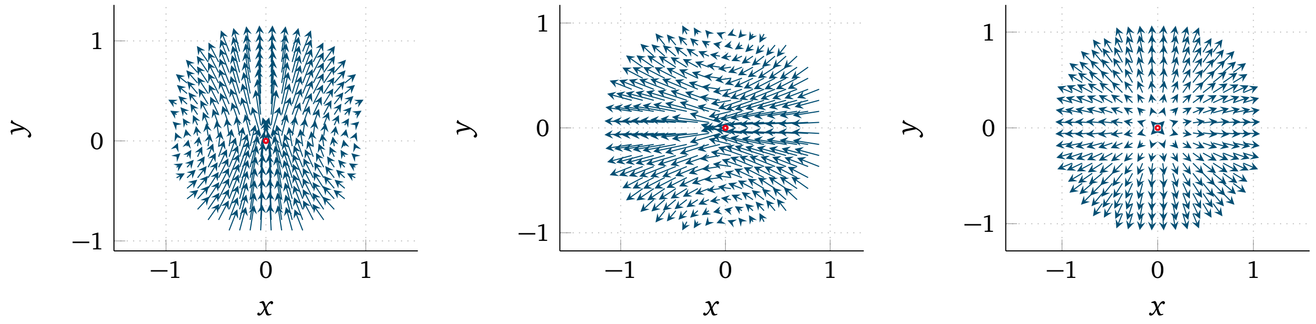

(a) $\text{TE}_{11}^{(1)}$ mode **(b)** $\text{TE}_{11}^{(2)}$ mode **(c)** $\text{TM}_{01}^{(1)}$ mode

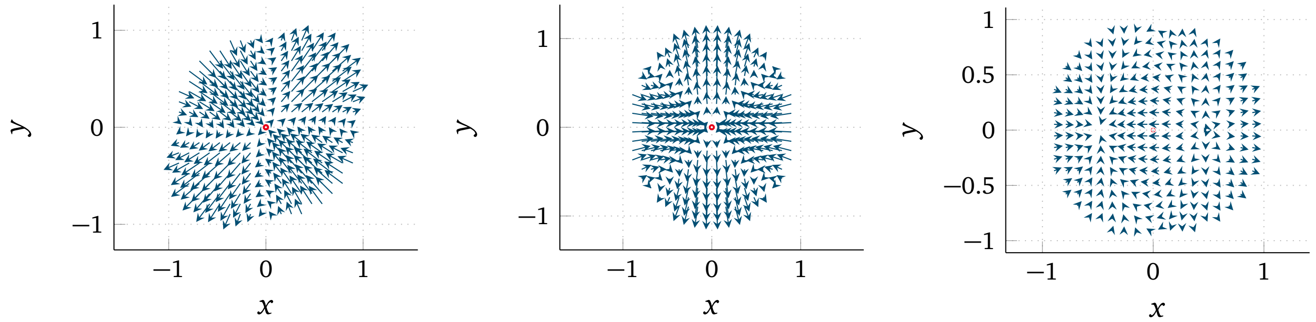

(d) $\text{TE}_{21}^{(1)}$ mode **(e)** $\text{TE}_{21}^{(2)}$ mode **(f)** $\text{TM}_{11}^{(1)}$ mode

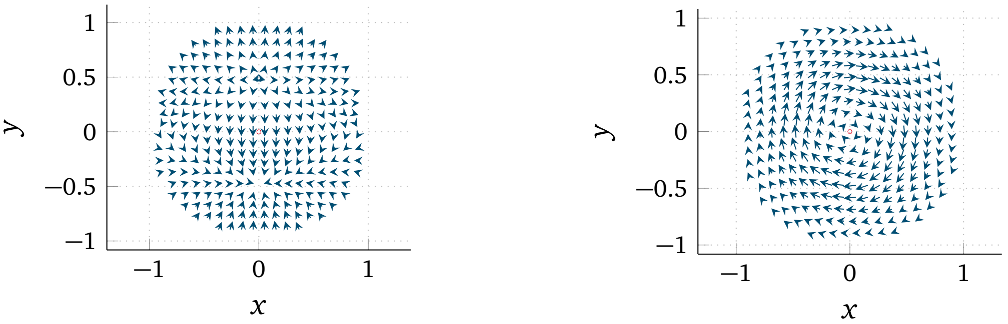

(g) $\text{TM}_{11}^{(2)}$ mode **(h)** $\text{TE}_{01}^{(1)}$ mode

Figure 2.2: The first eight 2D wavequide modes in the unit circle. Each mode is labelled as TM or TE. The first subscript is the azymuthal number m, the second one is the radial number n; the superscript identifies the polarisation.

Index p identifies the longitudinal distribution of the field extrema and, together with the previously introduced indeces m and n, allows for the classification of different modes.

The transverse components of the fields can be obtained using (2.14). For the TM modes we have

$$\underline{\mathbf{E}}_t = -\frac{p\pi}{L\gamma^2}\sin\left(\frac{p\pi}{L}z\right)\nabla_\perp\varphi(x,y) \tag{2.31}$$

and for the TE modes

$$\underline{\mathbf{H}}_t = -\frac{p\pi}{L\gamma^2}\cos\left(\frac{p\pi}{L}z\right)\nabla_\perp\varphi(x,y), \tag{2.32}$$

where $\gamma^2 = \omega^2/c^2 - k^2$ and $\nabla_\perp$ identifies the transverse gradient operator.

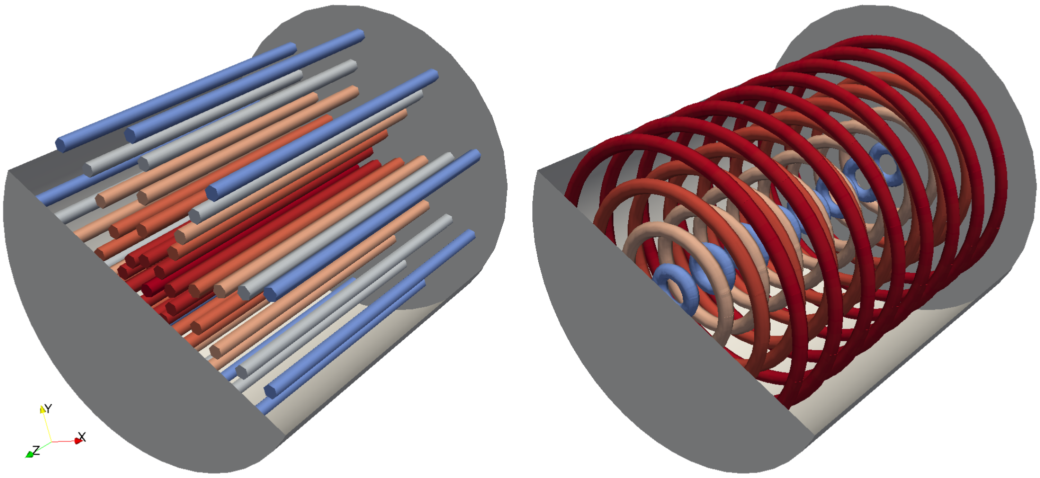

Figure 2.3: Electric field (left) and magnetif field (right) streamlines distribution for the accelerating mode TM_{010} in a pill-box cavity.

2.1.4 Pill-Box Cavity

A particular case of interest is the pill-box cavity, i.e. a cylindrical cavity, of radius R and length L. The lowest Transverse Magnetic mode solution of eigenproblem (2.28) is the TM_{010} mode and it has longitudinal electric field [61, chapter 8]

$$\underline{E}_z = E_0 \,\mathrm{J}_0\left(\frac{\chi_{01} r}{R}\right), \tag{2.33}$$

while all the other field components vanish. The field pattern is depicted in Figure 2.3. The angular frequency is

$$\omega_{010} = \frac{\chi_{01} c}{R}, \tag{2.34}$$

which is independent of the cavity length. The TM_{010} mode is the one preferably chosen for the acceleration of particles since it is the first mode (with the lowest frequency) with a non-zero electric field along the longitudinal direction on axis (higher order modes of type TM_{0np} could be analogously chosen). We will often call this mode the *accelerating mode*.

It is clear that to accelerate a beam through the cavity one has to cut holes at both ends and add beampipes for the particles to fly through. The dimensions of the beampipes are chosen in such a way that their cutoff frequency is well above that of the accelerating mode, which in turns guarantees that the field is mainly contained inside the cavity. However, these holes disrupt the simple geometry and it is no longer possible to obtain closed form solutions. Furthermore, since sharp corners can cause undesired effects on the quality of the field and the beam acceleration (see chapter 2.3 for the definition of the main quantities of interest), it is often preferable to build cavities with a more complicated shape, or even with more than one cell. Consequently, it is necessary to resort to numerical computations to evaluate the performance of these devices.

2.2 Standing-Wave RF Cavities

In the following, we will consider RF cavities operating with a standing-wave electromagnetic field. In this type of cavities, a RF power supply (e.g. a klistron [96]) is connected through an input coupler to the structure (see Fig. 5.1). The geometry of the cavity is such that the power supply frequency matches its accelerating resonant mode. To correctly excite the desired standing-wave accelerating field, the design is also optimised in such a way that other modes are significantly far from the accelerating one.

Let now $\left(\omega_n, \underline{\mathbf{E}}_n\right)$ be the resonant modes of the cavity, i.e. solutions of problem (2.28). The modes can be ordered according to their frequency $f_n = \omega_n / 2\pi$, creating a diverging sequence. The total electric field is given by the contribution of all the modes [81]

$$\mathbf{E}(\mathbf{r}, t) = \sum_n a_n e^{-\imath \omega_n t} \underline{\mathbf{E}}_n(\mathbf{r}), \tag{2.35}$$

where $a_n e^{-i\omega_n t}$ expresses the field variation in time and depends on the power losses on the walls due to Joule effects, on the power losses through the open surfaces, on the injected power through the coupler and on the excitation by the particle beam itself (*beam loading*). Among all these modes, one, denoted by $\underline{\mathbf{E}}_0$, having the strongest electric field on the axis in the longitudinal direction, is used to accelerate the beam (see Fig. 2.3). As stated before the mode commonly chosen for acceleration is the TM_{010} mode and, up to first order, only this mode is excited in the cavity.

Given the axis-symmetry of the general RF accelerating cavity, the classification of the eigenmodes usually refers to the pill-box case previously introduced. Exploiting the fact that a cylindrical cavity can be transformed into any other axis-symmetric cavity by a continuous deformation of its shape, the modes in the two configurations can be associated to each other. In the general case the matching is not an easy task, since, particularly for Higher Order Modes (HOMs), neither the longitudinal electric field nor the longitudinal magnetic field vanish. As a consequence, alternative classifications have been proposed to achieve an automatic mode recognition [14].

Multi-cell cavities add a further degree of complexity since they correspond to a system of coupled oscillators. The coupling between the modes of each cell creates groups of modes so that in an N-cell cavity each mode will split into N different modes. Each of this groups is called a passband [78, chapter 7]. If the connecting irises are small, the coupling between cells decreases and the frequency bandwidth will be smaller. Given a mode i in a certain passband, the field maxima will differ in each cell j proportionally to a sinusoidal function

$$|\underline{\mathbf{E}}| \propto \sin\left(i\pi \frac{2j-1}{2N}\right). \tag{2.36}$$

As a consequence, modes in an N-cell cavity can be further classified according to their *phase advance* as ${}^{i\pi}/_{N}$ modes: the one with the lowest frequency is the 0 - mode, the one with the highest is the π - mode.

The accelerating mode which is usually desired for acceleration in a multi-cell cavity is the TM_{010} π - mode and it corresponds to the last mode in the first monopole passband and is characterised by a strong longitudinal component of the electric field, which is of alternating sign in each cell. The synchronisation between the field oscillation and the particle beam should guarantee that the bunch only experiences the field in the correct direction. For non relativistic particles ($\beta \ll 1$), each cell needs to be longer than its predecessor in order to keep this synchronisation while the bunch is gaining speed.

2.3 Quantities of Interest in Accelerator Design

For a more complete explanation of the physics behind linear accelerators, in particular about beam dynamics, we refer the interested reader to [81, 96]. Here, we restrict ourselves to the definition of some important quantities that are commonly used to characterise accelerating cavities, following [78].

2.3.1 Accelerating Voltage

Let us consider an electron travelling at the speed of light in a resonating cavity. During the transit the particle will experience a time varying field. As stated previously, for the charge to receive the maximum energy transfer, the time necessary to traverse the cavity is

$$T = \frac{L}{c} = \frac{\pi}{\omega_0} \tag{2.37}$$

where L is the length of the cavity. Provided that the particle enters the cavity at the exact time the field is changing sign, it will always see the field pointing in the same direction. We can then define the accelerating voltage of the cavity as the line integral of the electric field seen by the charge along the cavity axis:

$$V_c = \left| \int_0^L E_z(r = 0, z) e^{\imath \omega_0 z/c} dz \right|. \tag{2.38}$$

It is often useful to introduce an average axial electric-field amplitude

$$E_{acc} = \frac{V_c}{L}. \tag{2.39}$$

The value of E_{acc} clearly depends on the choice of L. For a multicell cavity, the natural choice is the geometric cell length. By simple calculation one can see that for the pill-box cavity TM_{010} mode $E_{\mathrm{acc}} = 2E_0/\pi$.

2.3.2 Power Losses and Quality Factor

Real cavities, even when made of superconducting material, experience currents flowing in a thin surface layers of the walls. We call R_s the surface resistance which gives us the power dissipated in the walls due to Joule effect:

$$P_c = \frac{1}{2} R_s \int_S \left| \underline{\mathbf{H}} \right|^2 d\mathbf{s}, \tag{2.40}$$

where S is the wall surface and $\mathbf{H}$ the magnetic field at the walls.

By introducing the total stored energy of the accelerating field in the cavity volume Ω

$$U = \frac{\varepsilon_0}{2} \int_\Omega \left| \underline{\mathbf{E}} \right|^2 d\mathbf{r} = \frac{\mu_0}{2} \int_\Omega \left| \underline{\mathbf{H}} \right|^2 d\mathbf{r}. \tag{2.41}$$

it is possible to define the *quality factor* Q_0 which relates the stored energy and the power losses in the cavity walls:

$$Q_0 = \frac{\omega_0 U}{P_c}. \tag{2.42}$$

Combining (2.40) - (2.42) one obtains

$$Q_0 = \frac{\omega_0 \mu_0 \int_\Omega \left| \underline{\mathbf{H}} \right|^2 d\mathbf{r}}{R_s \int_S \left| \underline{\mathbf{H}} \right|^2 d\mathbf{s}} \tag{2.43}$$

which leads to the introduction of the so-called *geometry constant*

$$G = \frac{\omega_0 \mu_0 \int_\Omega \left|\underline{\mathbf{H}}\right|^2 d\mathbf{r}}{\int_S \left|\underline{\mathbf{H}}\right|^2 d\mathbf{s}}. \tag{2.44}$$

Since the constant G is solely dependent on the cavity shape, it is often used to compare cavities without having to take into account the materials or their size. The quality factor

$$Q_0 = \frac{G}{R_s}, \tag{2.45}$$

on the other hand, varies with the cavity size due to the frequency dependence of R_s [78].

2.3.3 Shunt Impedance

Another important quantity that characterises the losses in the cavity is the *shunt impedance* R_a which is defined as

$$R_a = \frac{V_c^2}{P_c} \tag{2.46}$$

It is worth mentioning that definition (2.46) is the most common in accelerator physics. However, other definitions are found in literature such as

$$R_a^c = \frac{V_c^2}{2P_c} \qquad \text{or} \qquad r_a = \frac{V_c^2}{P_c'}. \tag{2.47}$$

The one on the left is used in circuit theory, while the one on the right is sometimes used for LINACs. Here, P_c' is the power dissipated per unit length and is measured in ohms per meter. A large shunt impedance of the accelerating mode is desirable, since it means that the dissipated power is minimised.

Finally, it is possible to characterise the interaction of the beam with the accelerating mode through the *R over Q* factor:

$$\frac{R_a}{Q_0} = \frac{V_c^2}{\omega_0 U}, \tag{2.48}$$

which is independent of the surface resistance.

Figure 2.4: A superconducting TESLA cavity. (Copyright 2006 DESY)

2.3.4 Field Flatness and Cavity Tuning

In the case of multi-cell cavities, small variations between cells are sufficient to substantially alter the field profile. As a consequence of this, the cells need to be tuned in such a way that the accelerating field is the same in each cell. For a fixed amount of stored energy U_0 in the cavity, it is preferable to have equal fields in each cell for two main reasons: to maximise the accelerating voltage and to minimise the peak surface fields since they can cause electric field emission (see Fig. 2.5).

We denote with $E_{\mathrm{pk},j}$ the peak value of $E_z(r=0,z)$ in the j-th cell. The field flatness is measured by two quantities:

$$\eta_1 = \frac{1-\left(\max_j \left|E_{\mathrm{pk},j}\right| - \min_j \left|E_{\mathrm{pk},j}\right|\right)}{\mathbb{E}\left(\left|E_{\mathrm{pk},j}\right|\right)} \qquad \eta_2 = 1-\frac{\operatorname{std}\left(E_{\mathrm{pk},j}\right)}{\mathbb{E}\left(\left|E_{\mathrm{pk},j}\right|\right)}, \tag{2.49}$$

which are typically required to be ≥ 0.95 for a well tuned cavity.

In practice, the tuning is performed through mechanical deformation. The field flatness is measured by perturbing each cell in succession using a tiny metal tube segment (called *bead*) which travels along the cavity axis. Using a circuit model for the cells as capacitively coupled LC oscillators, a set of tuning parameters is computed which, in turn, give the required frequency shift for each cell [78, 91]. To lower (resp. increase) the frequency, each cell is shortened (elongated) along the z axis by a tuning machine which clamps the cavity at the irises and applies forces to obtain a permanent deformation [64].

2.4 TESLA Cavity

The main application presented in this thesis is the simulation of the so called TESLA cavity. The TESLA Technology Collaboration started in 1994 with the goal of developing a 500 GeV center-of-mass energy

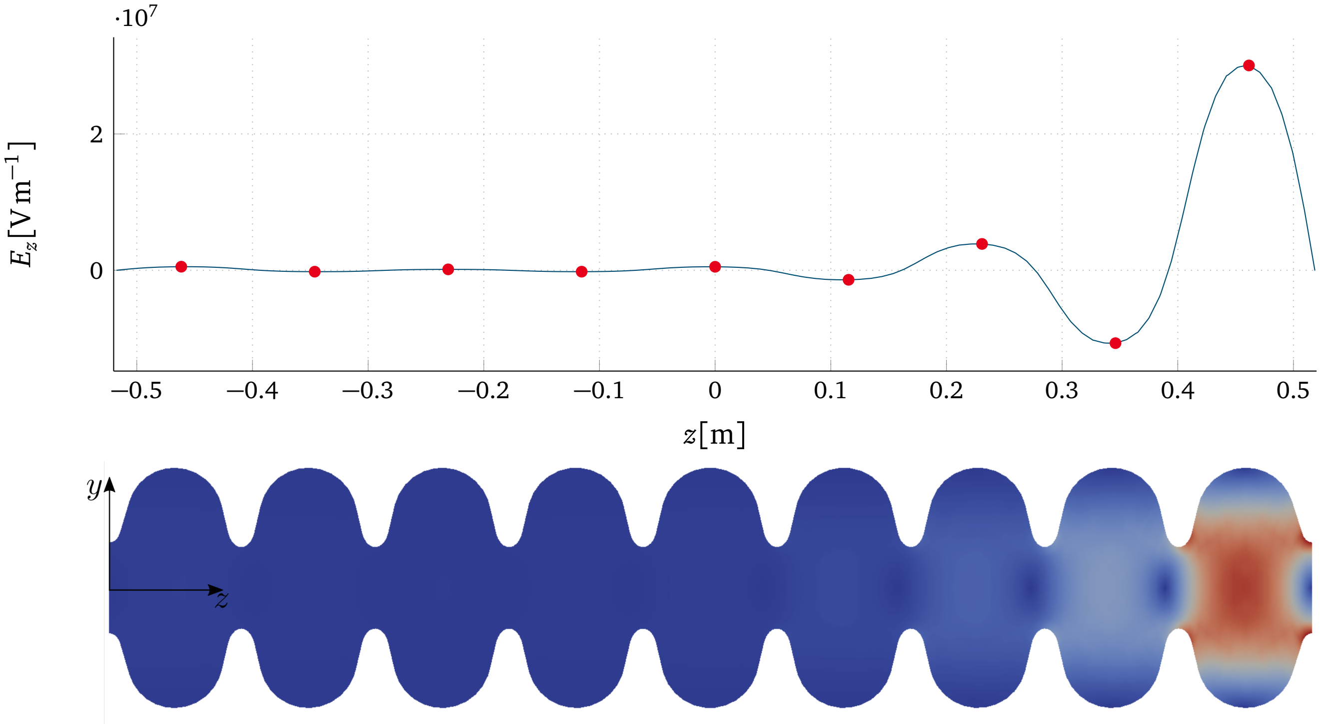

Figure 2.5: Electric field distribution in an untuned TESLA cavity constructed with the design parameter given in Table 2.1 (with PMC boundary conditions at the end irises). On the top, the field along the cavity axis $E_z(x=0,y=0,z)$; in red the values at the center of each cell. On the bottom, a yz cut of the cavity depicting the electric field magnitude.

Cavity Shape Parameter	Mid-Cup	End-Cup 1	End-Cup 2
Equator radius R_{eq}	103.3	103.3	103.3
Iris radius R_{iris}	35	39	39
Horizontal half axis at iris a_1	12	10	9
Vertical half axis at iris b_1	19	13.5	12.8
Horizontal half axis at equator a_2	42.0	40.3	42
Vertical half axis at equator b_2	42.0	40.3	42
Length L	57.7	56.0	57.0
Wall thickness w_{t}	2.5	2.5	2.5

Table 2.1: TESLA TTF design parameters for the different half-cells [2]. All dimensions are given in mm.

superconducting linear electron-positron collider with high accelerating gradient ($E_{acc} = 25\,\mathrm{MV\,m^{-1}}$) superconducting cavities. In particular we will focus on the TESLA Test Facility (TTF) design of the cavities [45] which were installed at Deutsches Elektronen-Synchrotron (DESY)'s Free-Electron Laser (FEL) FLASH in Hamburg. FLASH is able to produce extremely intense, ultrashort pulsed X-ray laser flashes.

The TTF cavity is a 9-cell standing wave structure of about 1 m in length whose lowest TM mode resonates at the comparatively low frequency of 1.3 GHz. This choice allows for the acceleration of long trains of particle bunches with very low emittance (i.e. a small spread of the particle bunch in the phase space), making a superconducting LINAC with TESLA cavities ideal for a free-electron laser in the vacuum ultraviolet and X-ray regimes. The particles enter the structure already at relativistic speed ($\beta \simeq 1$), so that the cells in the cavity are all equal in length.

In practice, the cavities are created, one half-cell at a time, by deep drawing of pure niobium sheets. Deep drawing is a forming process where a thin sheet of material is pressed into shape between two dies as shown in Fig. 2.6. The material in excess is trimmed using a milling machine and the half-cells are then joined at the equators through Electron Beam Welding (EBW) [60, 92].

The geometry of the TESLA cavity is given in terms of seven parameters that define the shape of each half-cell (see Fig. 2.7). The full cavity is then obtained by concatenation of all the half-cells and revolution of the outline around the cavity axis. If all the half-cells are taken into account, the model of the TESLA cavity comprises 126 parameters that define the shape of the cavity. Each of these quantities has an impact on the resonant frequency and the quality of the electric field that is excited during operation.

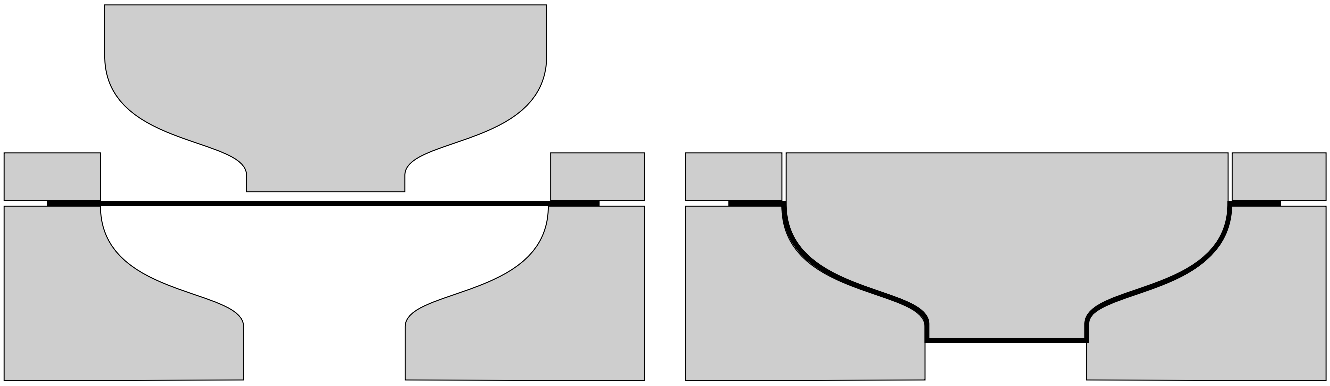

Figure 2.6: Deep drawing of a niobium sheet into a half-cell.

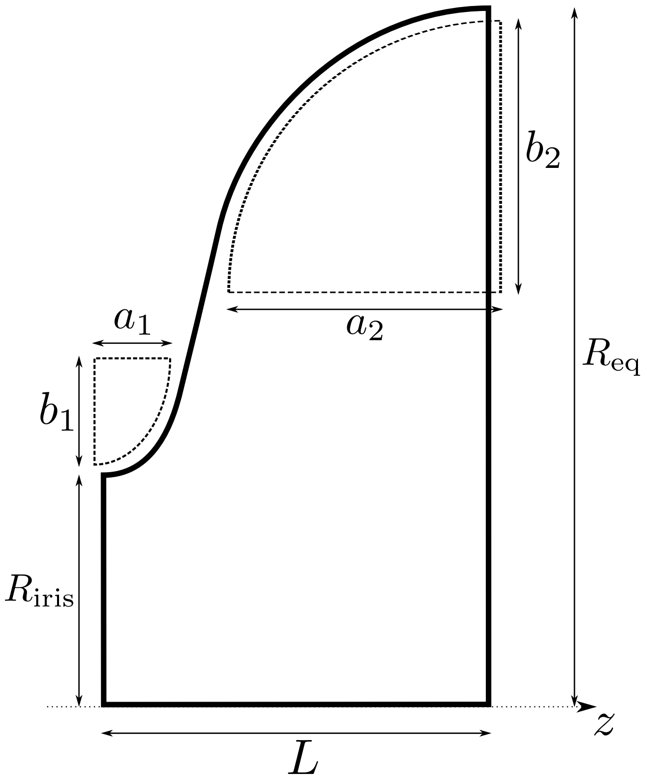

Figure 2.7: 2D cut of the TESLA Test Facility cavity half-cell profile with design parameters.

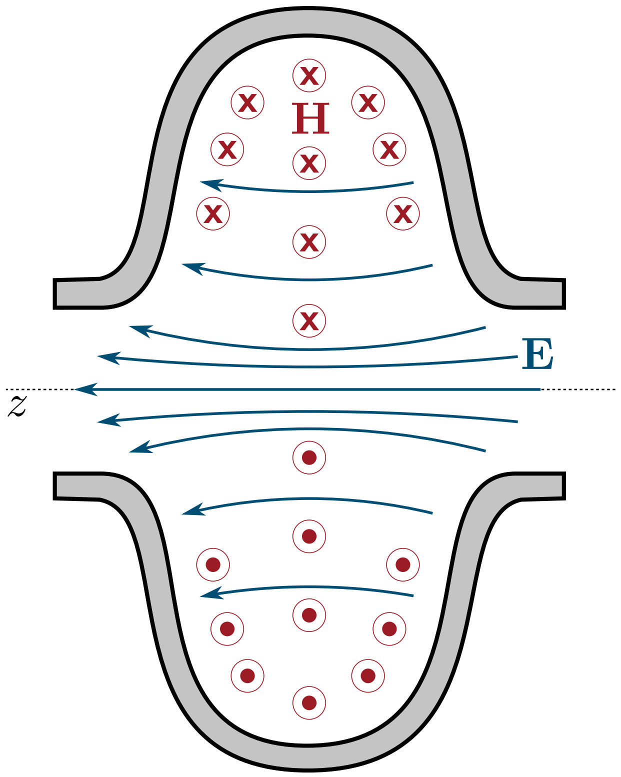

Figure 2.8: Schematic representation of the accelerating mode in a single cell standing-wave cavity. In blue the electric field lines, in red the magnetic ones.

2.5 Lorentz Detuning in RF Cavities

It is clear that real cavities will suffer from shape variations with respect to the design, for example due to manufacturing imperfections. In chapter 4 the impact of this uncertainty is considered using UQ methods. However, even in a cavity whose geometry complies perfectly with the design specifications, the inherent nature of the electromagnetic field behaviour can cause domain deformations. As a matter of fact, the high-energy electromagnetic field inside the cavity exerts a radiation pressure on the walls, which is responsible for mechanical deformations of the domain. Albeit small, such deformation may lead to a significant shift of the resonant frequency. These effects, known as *microphoning* and *Lorentz detuning* [36, 41, 51, 101], need to be considered and predicted with high precision in order to achieve a robust cavity design.

Consider, for the sake of simplicity, a single cell cavity as the one depicted in Fig. 2.9. Let Ω_{c} and Ω_{w} be the two disjoint open domains representing the cavity and its walls respectively and $\Gamma_{\mathrm{cw}} = \overline{\Omega}_{\mathrm{c}} \cap \overline{\Omega}_{\mathrm{w}}$ be the interface between the two. The evaluation of the Lorentz detuning effect requires the solution of two coupled problems: Maxwell's eigenvalue problem inside the undeformed and deformed cavity to obtain the accelerating electromagnetic field and an elastic problem in the cavity walls to compute the deformation. Since the deformations are known to be very small, we choose to employ a linear elastic model for the walls.

The coupling betweeen the two problems is given by the radiation pressure on the common interface Γ_{cw} which is obtained through a post-processing step from the electromagnetic field [88] and acts a a source boundary term for the linear elasticity problem. The calculation steps are then as follows:

Step 1. Solve Maxwell's eigenproblem (2.28) in Ω_{c} with PEC boundary conditions on $\partial\Omega_{\mathrm{c}}$. The eigenmode solution delivers a number of eigenfunction-eigenvalue couplets $\left(\omega_n^2, \underline{\mathbf{E}}_n\right)$, corresponding to

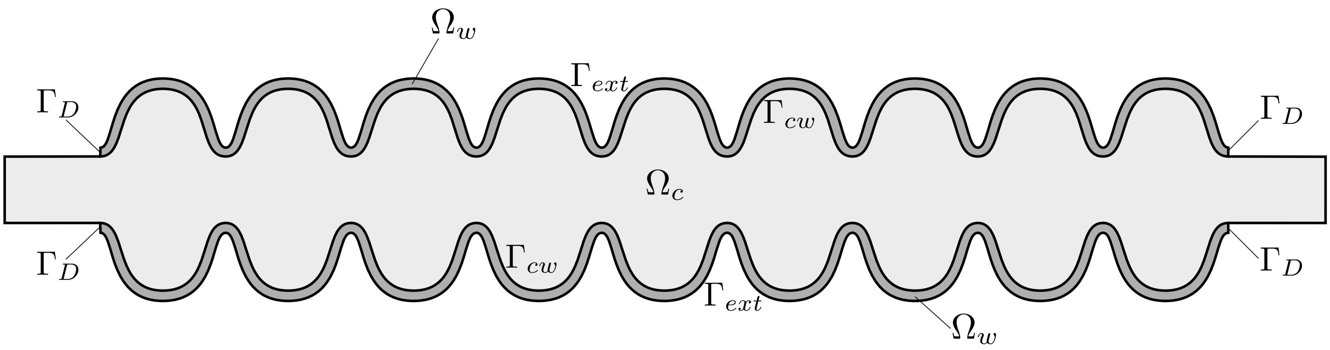

Figure 2.9: RF cavity domains for the Lorentz detuning simulation. In light grey the cavity chamber filled with vacuum Ω_c and in dark grey the cavity walls Ω_{w}. The walls are considered to be fixed at the irises where the connecting beampipes start.

the possible modes within the cavity. The accelerating mode of interest is the first transverse magnetic mode TM_{010} (see Fig. 2.8). Let $\underline{\mathbf{E}}_0$ be the computed electric field and ω_0^2 the corresponding eigenvalue, then $f_0 = \omega_0/2\pi$ is the resonant frequency for the accelerating eigenmode in the undeformed geometry.

Step 2. Compute the magnetic field $\underline{\mathbf{H}}_0$ for the first accelerating eigenmode as

$$\underline{\mathbf{H}}_0 = \frac{\imath}{\omega_0 \mu_0} \nabla \times \underline{\mathbf{E}}_0. \tag{2.50}$$

In first approximation the accelerating mode is the only mode excited in the cavity and it will exert a radiation pressure p on its walls. Due to the oscillating nature of the field, this pressure has a static component plus an oscillating component at frequency $2f_0$. In practice, however, the latter can be neglected [88] and the radiation pressure on Γ_{cw} is approximated by a time-constant value that may be expressed as

$$p_{\mathrm{rad}} = -\frac{1}{4}\varepsilon_0 \Big(\mathbf{E}_{\mathrm{pk}} \cdot \mathbf{n}_c\Big)\Big(\mathbf{E}^*_{\mathrm{pk}} \cdot \mathbf{n}_c\Big) + \frac{1}{4}\mu_0 \Big(\mathbf{H}_{\mathrm{pk}} \times \mathbf{n}_c\Big) \cdot \Big(\mathbf{H}^*_{\mathrm{pk}} \times \mathbf{n}_c\Big) \tag{2.51}$$

where $\mathbf{E}_{\mathrm{pk}}$ and $\mathbf{H}_{\mathrm{pk}}$ are the field peak values and $\cdot^*$ denotes the complex conjugate operator.

Step 3. Solve the following linear elasticity problem in the walls domain Ω_w

$$-\nabla \cdot \boldsymbol{\sigma} = 0 \qquad \text{in } \Omega_{\mathrm{w}} \tag{2.52a}$$

with the constitutive law

$$\boldsymbol{\sigma} = 2\eta \nabla^{(S)} \mathbf{u} + \kappa \mathbf{I} \nabla \cdot \mathbf{u} \tag{2.52b}$$

and boundary conditions

$$\begin{cases} \boldsymbol{\sigma}\mathbf{n}_w = p_{\mathrm{rad}}\mathbf{n}_w & \text{on } \Gamma_{\mathrm{cw}} \\ \boldsymbol{\sigma}\mathbf{n}_w = 0 & \text{on } \Gamma_{\mathrm{ext}} \\ \mathbf{u} = 0 & \text{on } \Gamma_D := \partial\Omega_w \setminus (\Gamma_{cw} \cup \Gamma_{\mathrm{ext}}) \end{cases} \tag{2.52c}$$

for the displacement $\mathbf{u}$. In (2.52) we denote by $\nabla^{(S)}$ the symmetric gradient

$$\nabla^{(S)} = \frac{1}{2}\Big(\nabla \mathbf{u} + \nabla \mathbf{u}^\top\Big), \tag{2.53}$$

while κ and η are the first and second Lamé parameters of the wall constituent material and $\mathbf{n}_{\mathrm{w}}$ is the outward unit normal to Ω_{w}. The Lamé parameters can derived starting from the Young's modulus E and Poissons' ratio ν of a given material as:

$$\kappa = \frac{\nu E}{(1+\nu)(1-2\nu)} \qquad \eta = \frac{E}{2(1+\nu)}. \tag{2.54}$$

On Γ_{cw} the radiation pressure p is applied, while the irises are considered to be fixed.

Step 4. Let the deformed walls domain $\Omega_{\mathrm{w}}^{'}$ be defined as

$$\Omega_{\mathrm{w}}^{'} \equiv \{\mathbf{r} + \mathbf{u}(\mathbf{r}), \mathbf{r} \in \Omega_{\mathrm{w}}\}, \tag{2.55}$$

and the deformed cavity boundary $\Gamma_{\mathrm{cw}}^{'}$ as

$$\Gamma_{\mathrm{cw}}^{'} \equiv \{\mathbf{r} + \mathbf{u}(\mathbf{r}), \mathbf{r} \in \Gamma_{\mathrm{cw}}\}. \tag{2.56}$$

Furthermore, let $\Omega_{\mathrm{c}}^{'}$ denote the domain enclosed by $\Gamma_{\mathrm{cw}}^{'}$ and the two irises.

Step 5. Solve once again Maxwell's eigenproblem (2.28) in $\Omega_{\mathrm{c}}^{'}$ with analogous boundary conditions. Let $(\underline{\mathbf{E}}_0^{'}, (\omega_0^{'})^2)$ denote the accelerating eigenmode. The shifted frequency is finally obtained as

$$f_0^{'} = \frac{\omega_0^{'}}{2\pi} \tag{2.57}$$

and the frequency shift due to Lorentz detuning as

$$\Delta f_0 = \left| f_0 - f_0^{'} \right|. \tag{2.58}$$

This procedure can be carried out iteratively if necessary.

2.6 Summary

After stating the fundamental laws of electromagnetism, the eigenvalue problem for the time-harmonic fields in a resonator has been derived. A closed form solution is available only when trivial shapes are considered, e.g. parallelepipeds or cylinders. In the second part of the chapter we have defined the most common quantities of interest used in RF cavity design and we have proposed a coupled model for simulation of the Lorentz detuning effect.

Our main interest is the simulation of devices whose performance is highly sensitive to the domain shape. As such we propose the application of Isogeometric methods for the numerical treatment. In the following chapter we focus on the discretisation of Maxwell's eigensystem (2.28) and of linear elasticity problem (2.52) using IGA, giving particular attention to the construction of suitable approximation spaces for the electromagnetic fields.

3 Isogeometric Analysis

We now enter the world of discrete,
the solution we apply is quite neat:
from computer designs
we can take the B-Splines,
and the diagram will be complete.

The first step in the numerical treatment of a PDE on a domain of interest Ω is, typically, the discretisation of the domain itself. One classical example is the meshing process of classical FEM which subdivides the geometry into triangles (quadrilaterals) in the 2D case or tetrahedra (hexahedra) in the 3D case. Whenever the geometry is non trivial, this immediately introduces an approximation. The use of curved boundary meshes and higher order elements [71] alleviates this problem, but does not solve it, since even common curves like conical sections (circles, ellipses, etc. . .) cannot be exactly represented by a polynomial map.

In many practical applications the domain Ω is generated through a CAD software, thus a set of basis functions and a parametrisation of it (or at least of its boundary representation) are already available. IGA was introduced in 2005 by Hughes et al. [58] with the idea of using the same classes of basis functions commonly used for geometry description in CAD software, for the representation of the solution of scalar (or vector) fields. Such basis functions are the so called B-Splines and NURBS basis functions [12, 83].

This distinctive feature allows for the exact representation of geometries defined via CAD, independently of the level of refinement of the computational grid. Moreover, the commonly employed piece-wise polynomial spaces are embedded into NURBS spaces, thus IGA can be seen as a generalisation of standard FEMs. It is worth mentioning the fact that IGA shares the same Galerkin approach as FEM: a weak formulation of the PDE is constructed and cast in a suitable space V, and a set of basis functions is selected in order to construct a sequence of proper subspaces $V_h \to V$ as $h \to 0$. IGA expands the set of basis functions from polynomials to the superset of rational polynomials. In many cases a pre-existent code can be easily modified to work in an IGA setting by changing the basis function construction routines only. Given the higher regularity of the basis functions employed, the method has been shown to present several advantages over FEM in addition to the better handling of CAD geometries, like a faster convergence with respect to the number of degrees of freedom [62] and the possibility to treat higher order differential operators [4].

As mentioned in the Introduction, these properties have made IGA appealing for a wide variety of applications (see chapter 1).

In the simulation of RF cavities it is especially interesting to be able to accurately represent the geometry throughout the analysis without the mesh approximation, since the use of NURBS guarantees exact representation of the elliptical arcs that defines the half-cells (see Fig. 2.7). Furthermore, IGA allows for the domain deformations to be handled in an accurate and straightforward way by changing only a relatively small number of control points.

As a first step in this chapter we state the variational formulation of the cavity eigenproblem. The weak formulation requires us to define Sobolev spaces of both scalar and vector valued functions and important relations that hold between them. The concepts of IGA are then introduced with focus on the application to RF cavity simulation. In particular we define B-Splines and Non-Uniform Rational B-Splines basis functions and show how they are used to parametrise geometries. In section 3.4 those functions and mapping are used to discretise Maxwell's equations and the linear elasticity problem (2.52). Finally a brief explanation on how to treat complicated domains using a multipatch approach is given.

3.1 Weak Formulation

To numerically solve Maxwell's eigenvalue problem (2.28) the Galerkin Ansatz is used. For this purpose the equations must be cast into weak formulation and suitable choices for the spaces must be made.

A preliminary step before the discretisation is the construction of its weak form and the definition of the proper spaces in which to cast it.

3.1.1 Vector Functions with Well Defined Curl or Divergence

For the definition of the Sobolev spaces we follow [71, chapter 3] and we denote by $L^p(\Omega)$ the classical Lebesgue spaces endowed with the norm $\|\cdot\|_{L^p(\Omega)}$, and by $\mathbf{L}^p(\Omega)$ their vector valued counterparts. The Hilbert spaces $H^k(\Omega)$ denote the functions in $L^p(\Omega)$ such that their k-th order derivatives also belong to $L^p(\Omega)$, and $\mathbf{H}^k(\Omega)$ are their vector valued counterparts. When a fixed value is prescribed on a section of the boundary $\Gamma \subseteq \partial\Omega$, we will use the common notation $H^k_{0,\Gamma}(\Omega)$ and $\mathbf{H}^k_{0,\Gamma}(\Omega)$, where the 0 subscript denotes homogeneous boundary conditions.

To correctly deal with Maxwell's equations we need to introduce the spaces of $L^2(\Omega)$ functions with divergence or curl in $L^2(\Omega)$. Under the hypothesis mentioned above, the space of functions with divergence in $L^2(\Omega)$ is denoted by $\mathbf{H}(\mathrm{div};\Omega)$ and defined by:

$$\mathbf{H}(\mathrm{div};\Omega) = \left\{\mathbf{v} \in \mathbf{L}^2(\Omega) : \nabla \cdot \mathbf{v} \in L^2(\Omega)\right\} \tag{3.1}$$

with the associated norm

$$\|\mathbf{v}\|_{\mathbf{H}(\mathrm{div};\Omega)} = \left(\|\mathbf{v}\|^2_{\mathbf{L}^2(\Omega)} + \|\nabla \cdot \mathbf{v}\|^2_{L^2(\Omega)}\right)^{1/2}. \tag{3.2}$$

To solve problems in which the normal component of a vector field is specified on $\partial\Omega$, it is also useful to consider the subspace of $\mathbf{H}(\mathrm{div};\Omega)$:

$$\mathbf{H}_0(\mathrm{div};\Omega) = \{\mathbf{v} \in \mathbf{H}(\mathrm{div};\Omega) : \mathbf{v} \cdot \mathbf{n}\,|_{\partial\Omega} = 0\}, \tag{3.3}$$

corresponding to the kernel of the trace operator

$$\gamma_{\mathbf{n}}(\mathbf{v}) = \mathbf{v}\,|_{\partial\Omega} \cdot \mathbf{n}. \tag{3.4}$$

We denote the space of three-dimensional vector functions with curl in $\mathbf{L}^2(\Omega)$ as

$$\mathbf{H}(\mathbf{curl};\Omega) = \left\{\mathbf{v} \in \mathbf{L}^2(\Omega) : \nabla \times \mathbf{v} \in \mathbf{L}^2(\Omega)\right\} \tag{3.5}$$

endowed with the norm

$$\|\mathbf{v}\|_{\mathbf{H}(\mathbf{curl};\Omega)} = \left(\|\mathbf{v}\|^2_{\mathbf{L}^2(\Omega)} + \|\nabla\times\mathbf{v}\|^2_{\mathbf{L}^2(\Omega)}\right)^{1/2}. \tag{3.6}$$

The space $\mathbf{H}(\mathbf{curl};\Omega)$ is of great importance in the study of Maxwell's equations since it corresponds to the space of finite-energy solutions [71].

Let us now assume, for the sake of simplicity, that our domain Ω is simply connected and that its boundary $\partial\Omega$ is split into two disjoint parts, $\partial\Omega = \Gamma_D \cup \Gamma_N$ with $\Gamma_D \neq 0$. We denote by $\mathbf{H}_{0,\Gamma_D}(\mathbf{curl};\Omega)$ the space of functions in $\mathbf{H}(\mathbf{curl};\Omega)$ with vanishing tangential trace on Γ_D:

$$\gamma_t(\mathbf{v}) = \mathbf{v}|_{\Gamma_D} \times \mathbf{n} = 0. \tag{3.7}$$

A more in depth discussion about the trace properties of functions in $\mathbf{H}(\mathbf{curl};\Omega)$ can be found in [71].

3.1.2 Weak Formulation of the Eigenvalue Problem

The standard variational formulation of (2.28) is [11]: *Find* $\omega \in \mathbb{R}$ *and* $\mathbf{E} \in \mathbf{H}_0(\mathbf{curl};\Omega)$ *with* $\mathbf{E} \neq 0$ *such that*

$$(\nabla\times\mathbf{E}, \nabla\times\mathbf{v}) = \omega^2\varepsilon_0\mu_0(\mathbf{E},\mathbf{v}) \qquad \forall\mathbf{v}\in\mathbf{H}_0(\mathbf{curl};\Omega) \tag{3.8a}$$

$$(\mathbf{E}, \nabla\phi) = 0 \qquad \forall\phi \in H^1_0(\Omega), \tag{3.8b}$$

where $(\cdot,\cdot)$ identifies the usual $\mathbf{L}^2$ scalar product in Ω, i.e.

$$(\mathbf{u},\mathbf{v}) = \int_\Omega \mathbf{u}\cdot\mathbf{v}\,d\mathbf{r}. \tag{3.9}$$

In practice, however, the following formulation is used [11, 98]: *Find* $\omega\in\mathbb{R}$ *and* $\mathbf{E}\in\mathbf{H}_0(\mathbf{curl};\Omega)$ *with* $\mathbf{E}\neq 0$ *such that*

$$(\nabla\times\mathbf{E}, \nabla\times\mathbf{v}) = \omega^2\varepsilon_0\mu_0(\mathbf{E},\mathbf{v}) \qquad \forall\mathbf{v}\in\mathbf{H}_0(\mathbf{curl};\Omega). \tag{3.10}$$

In general, there exists two groups of solution of (3.10): static fields (with $\omega = 0$ and $\nabla\times\mathbf{E} = 0$) and resonant fields (with $\omega \neq 0$). The first case corresponds to the infinite dimensional eigenspace given by the gradient of functions in $H^1_0(\Omega)$, while the other eigenvalues form a diverging sequence with eigenfunctions in $\mathbf{H}_0(\mathbf{curl};\Omega)\cap\mathbf{H}\left(\mathrm{div}^0;\Omega\right)$, where we have introduced the space

$$\mathbf{H}\left(\mathrm{div}^0;\Omega\right) := \left\{\mathbf{v}\in\mathbf{L}^2(\Omega) \text{ s.t. } \nabla\cdot\mathbf{v} = 0\right\} \tag{3.11}$$

of integrable functions with zero divergence [11, 71].

Given weak formulation (3.10), it is possible to construct a sequence of finite dimensional subsets $V_h \subset \mathbf{H}_0(\mathbf{curl};\Omega)$ in terms of a set of basis functions:

$$V_h = \mathrm{span}\{\mathbf{v}_i\}_{i=1}^{N_\mathrm{dof}}, \qquad \dim(V_h) = N_\mathrm{dof}. \tag{3.12}$$

These basis functions are used both for the testing and for expressing the solution field:

$$\mathbf{E} \approx \mathbf{E}_h \in V_h, \qquad \mathbf{E}_h = \sum_{j=1}^{N_\mathrm{dof}} e_j\mathbf{v}_j. \tag{3.13}$$

The discretised weak formulation becomes: *Find* $\omega_h\in\mathbb{R}$ *and* $\mathbf{E}_h\in V_h$ *with* $\mathbf{E}_h\neq 0$ *such that*

$$\sum_{j=1}^{N_\mathrm{dof}} e_j\left(\nabla\times\mathbf{v}_j, \nabla\times\mathbf{v}_i\right) = \omega_h^2\varepsilon_0\mu_0\sum_{j=1}^{N_\mathrm{dof}} e_j\left(\mathbf{v}_j,\mathbf{v}_i\right) \qquad \forall i = 1,\ldots,N_\mathrm{dof}. \tag{3.14}$$

By introducing the stiffness and the mass matrix $\mathbf{K}\in\mathbb{R}^{N_\mathrm{dof}\times N_\mathrm{dof}}$ and $\mathbf{M}\in\mathbb{R}^{N_\mathrm{dof}\times N_\mathrm{dof}}$ with elements

$$k_{ij} = \left(\nabla\times\mathbf{v}_j, \nabla\times\mathbf{v}_i\right), \qquad m_{ij} = \left(\mathbf{v}_j,\mathbf{v}_i\right), \tag{3.15}$$

we obtain to the generalised eigenvalue problem

$$\mathbf{K}\mathbf{e} = \lambda\mathbf{M}\mathbf{e}. \tag{3.16}$$

3.2 IGA Basis Functions

Curves consisting of just one polynomial or rational segment may often be inadequate to represent complex shapes (for example they might require a very high degree to satisfy the constraints). On the other hand, B-Spline and NURBS functions enjoy some major advantages that make them extremely convenient for surface modelling and are therefore the most commonly used technology for solid geometry modelling on which current CAD tools are based.

Among such advantages we care to mention in particular:

- They can exactly represent all conic sections, i.e. circles, ellipses, etc...
- They can be generated by many efficient and numerically stable algorithms
- They can handle arbitrary continuity in single points easily.

In this section we introduce the definition of such basis functions and highlight some properties that prove to be useful in the analysis.

3.2.1 B-Spline functions

A B-Spline object is obtained as the transformation through an appropriate mapping of a *reference domain* in the parameter space to a geometrical entity in the physical space. In one dimension, for example, this reference domain is typically given by the unit interval $[0,1]$. For the definition of the B-Spline basis, the interval is subdivided by a knot vector

$$\Xi = \left[\xi_1, \xi_2, \ldots, \xi_{n+p+1}\right] \quad \text{with } \xi_i \leq \xi_{i+1} \tag{3.17}$$

where $\xi_i \in [0,1]$ is the i-th knot and n is the number of basis functions. By convention there is a distinction between the polynomial *degree* p of the B-Spline basis and its *order* $p+1$. In the following, we will always refer to the degree to avoid creating ambiguity with the Finite Element case. Knot vectors can be *uniform*, if the knots are equally spaced, or non-uniform otherwise.

Given the knot vector, the i-th B-Spline basis function of degree p, denoted by $B_i^p(\xi)$, is defined by the recurrence formula (Cox-de Boor) [12]:

$$B_i^0(\xi) = \begin{cases} 1 & \text{if } \xi_i \leq \xi \leq \xi_{i+1} \\ 0 & \text{otherwise} \end{cases} \qquad B_i^p(\xi) = \frac{\xi - \xi_i}{\xi_{i+p} - \xi_i} B_i^{p-1}(\xi) + \frac{\xi_{i+p+1} - \xi}{\xi_{i+p+1} - \xi_{i+1}} B_{i+1}^{p-1}(\xi), \tag{3.18}$$

for $i = 1, \ldots, n$. Equation (3.18) can yield the quotient $0/0$ which is defined to be zero. An example of such basis functions can be seen in Fig. 3.1.

The main properties of B-Spline basis functions are:

- The basis $\left\{B_i^p\right\}_{i=1}^n$ constitutes a partition of unity.
- Each basis function is point-wise non-negative over the entire domain.
- $B_i^0(\xi)$ is a step function, equal to zero everywhere except on the half-open interval $\xi \in [\xi_i, \xi_{i+1})$. The half open interval $[\xi_i, \xi_{i+1})$ is called the i-th knot-span.
- For $p > 0$, $B_i^p(\xi)$ is a linear combination of two $(p-1)$-degree basis functions.
- Each p-th degree function has $p-1$ continuous derivatives across the element boundaries (i.e. across the knots) if they are not repeated.
- The support of the B-Spline of degree p is always $p+1$ knot spans.

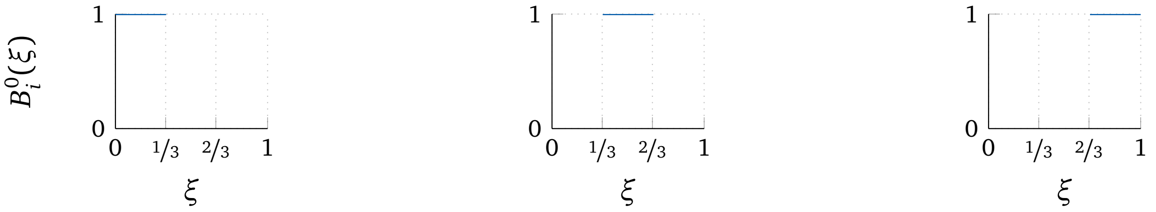

(a) B-Spline basis of degree 0. Knot vector $\Xi = [0, 1/3, 2/3, 1]$

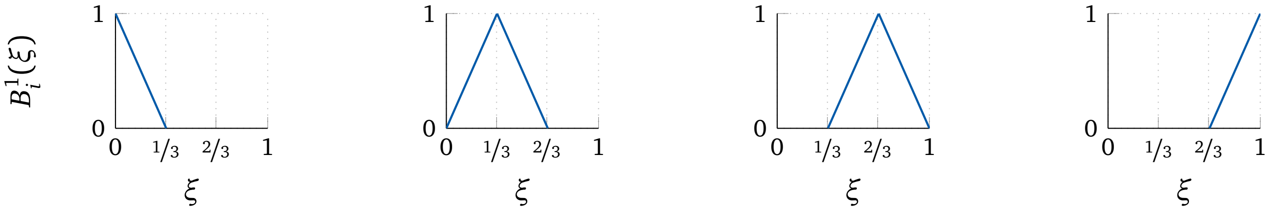

(b) B-Spline basis of degree 1. Knot vector $\Xi = [0, 0, 1/3, 2/3, 1, 1]$

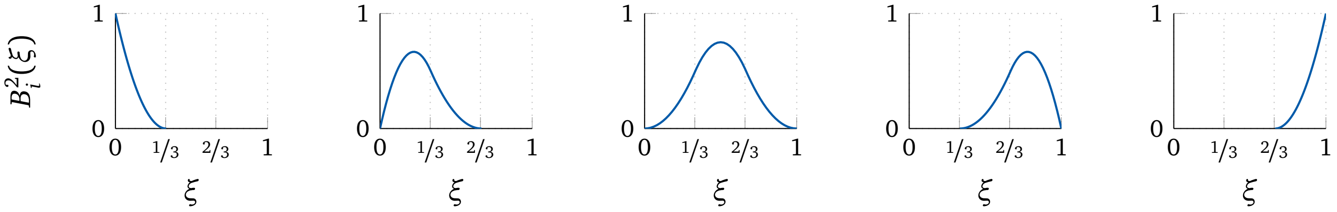

(c) B-Spline basis of degree 2. Knot vector $\Xi = [0, 0, 0, 1/3, 2/3, 1, 1, 1]$

Figure 3.1: B-Spline basis functions with varying degree on an open, uniform knot vector.

The concepts presented until now can be easily extended to multi-dimensional B-Spline functions using a tensor product approach. For instance in the 3D case, given the knot vectors Ξ_d, the degrees p_d and the number of basis functions n_d (with $d = 1, 2, 3$), the B-Spline trivariate basis functions are defined as

$$B_{\mathbf{i}}^{\mathbf{p}}(\xi) = B_{i_1}^{p_1}(\xi) B_{i_2}^{p_2}(\xi) B_{i_3}^{p_3}(\xi), \tag{3.19}$$

where $\mathbf{p} = (p_1, p_2, p_3)$ and $\mathbf{i} = (i_1, i_2, i_3)$ is a multi-index in the set

$$\mathscr{I} = \{(i_1, i_2, i_3) : 1 \leq i_d \leq n_d\}. \tag{3.20}$$

3.2.2 Non-Uniform Rational B-Splines

We can now exploit the concepts of the previous section to obtain Non-Uniform Rational B-Splines shape functions. Starting from the Cox-de Boor formula given in (3.18), we define the rational basis functions $N_i^p(\xi)$:

$$N_i^p(\xi) = \frac{w_i B_i^p(\xi)}{\sum_{j=a}^{n} w_j B_j^p(\xi)} \tag{3.21}$$

where we assume $w_i > 0 \; \forall i$.

It is important to notice that from this definitions, B-Splines are nothing else than a particular case of NURBS, where the weights given to the basis functions are all equal. An other useful way to understand them is as the projection on $\mathbb{R}^d$ of a B-Spline in $\mathbb{R}^{d+1}$ (see Fig. 3.3).

The higher dimensional basis functions are constructed once again through tensor product as in (3.19).

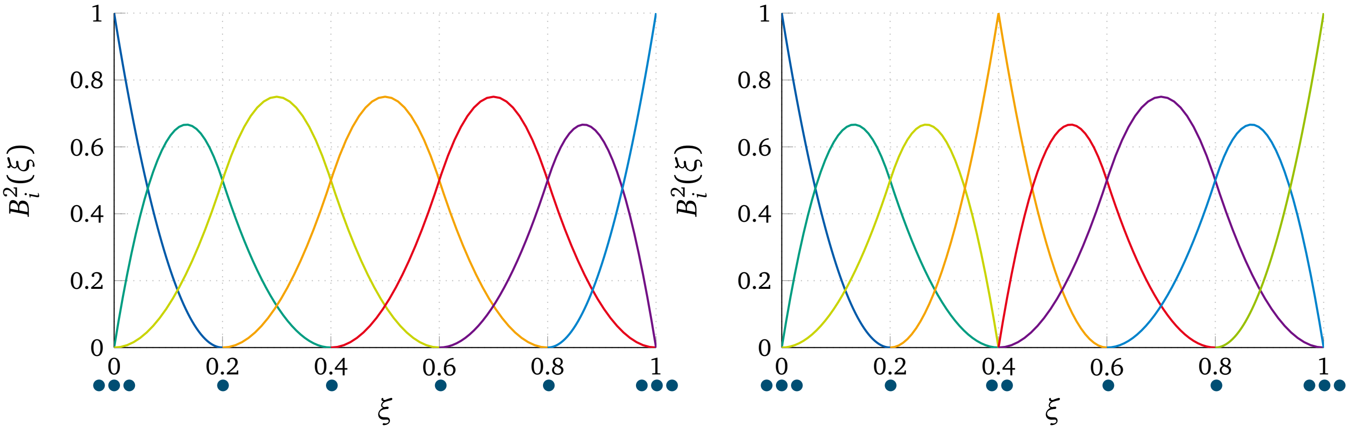

(a) B-Spline basis with C^1 continuity.

(b) B-Spline basis with C^0 continuity at knot 0.4.

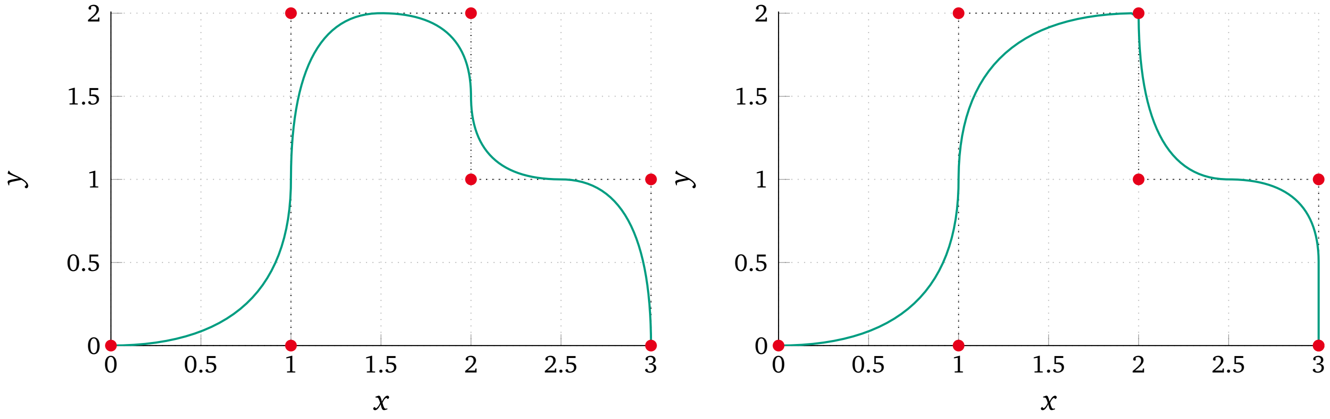

(c) B-Spline curve with C^1 continuity.

(d) B-Spline curve with C^0 continuity.

Figure 3.2: B-Spline basis functions for degree $p = 2$. The coloured dots indicate the knots positioning. Knot repetition influences the continuity of the curve.

3.3 Geometry Parametrisation and Modelling of Deformations

To build a B-Spline or NURBS curve, a set of *control points* needs to be defined. The linear combination of the basis functions with those points as coefficient, gives the mapping to the physical space. In particular, given n basis functions N_i^p and n control points $\mathbf{P}_i \in \mathbb{R}^d$, $i = 1, \ldots, n$, a curve is given by:

$$\mathbf{C}(\xi) = \sum_{i=1}^{n} \mathbf{P}_i N_i^p(\xi). \tag{3.22}$$

The control points define the so called control mesh (or control polygon) but this mesh does not, in general, conform to the actual geometry (see Fig. 3.2). On the contrary, the physical mesh is a decomposition of it: the element boundaries are the image of the knots through the mapping (3.22).

One of the most useful properties in CAD is the possibility to easily handle sharp corners and sudden changes in regularity of the curve. This is achieved by knot repetition: it is straightforward to see from (3.18) and (3.22) that a change in the multiplicity of a knot changes the continuity of the curve in correspondence of that knot. Given r_i, the multiplicity of the i-th knot, basis functions of degree p have $p - r_i$ continuous derivatives across the knot ξ_i. In the particular case of a knot repeated exactly $r_i = p + 1$ times, the basis is interpolatory at the knot ξ_i. We define as *open* a knot vector whose first and last knots are repeated $p + 1$ times (i.e. the curve is interpolatory at its ends). Below, we will always assume to be dealing with open knot vectors since they will be required in the construction of approximating spaces to enforce boundary conditions.

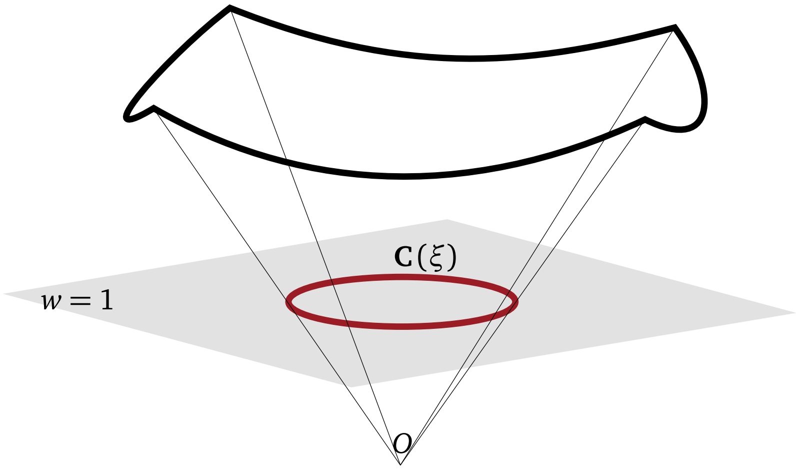

Figure 3.3: NURBS projection.

The properties of CAD curves follow directly the properties of the basis functions. For instance, continuity is controlled by the basis functions, while the control points act as weights, hence the control points can be modified without altering the curve continuity. Moreover, due to the compact support of the basis functions, moving a single control point can affect the geometry of no more than $p+1$ elements of the curve. This particular property is obviously one of the main reasons for the frequent usage of B-Spline and NURBS in CAD, since by moving a control point one can modify just a small portion of the curve.

The main advantage of NURBS over B-Spline curves is the possibility to exploit both the control points and the weights to control the local shape: as w_i increases, the curve is pulled closer to the control point $\mathbf{P}_i$, and vice versa. While non-rational splines (or Bézier curves) can approximate a circle, they are unable to represent it exactly. Rational splines, however, can represent any conic section exactly (although, in general, the parametrisation is not unique).

To construct manifolds and volumes, the parametrisation is once again a tensor product. A net of control points $\mathbf{P}_\mathbf{i}$ in the physical space is constructed, thus a volumetric mapping would become:

$$\mathbf{V}(\xi) = \sum_{\mathbf{i}\in\mathscr{I}} \mathbf{P}_\mathbf{i} N_\mathbf{i}^\mathbf{p}(\xi). \tag{3.23}$$

Maps of the types (3.22) and (3.23) also present advantages when dealing with deformations. Affine transformations, for example, are straightforward to apply since it is sufficient to apply the transformation directly to the control net. More complicated changes to the shape can be obtained by using an isoparametric deformation mapping defined as a NURBS entity in itself, and adding the corresponding control points. Given, for example, a NURBS curve as in Fig. 3.4a with a set of control points $\{\mathbf{P}^{(1)}\}$ and a deformation curve defined on the same set of basis functions, i.e. with the same number of degrees of freedom (Fig. 3.4b), with control points $\{\mathbf{P}_i^{(2)}\}$, the deformed curve is obtained as:

$$\mathbf{C}_{def}(\xi) = \sum_{i=1}^{n} \left(\mathbf{P}_i^{(1)} + \mathbf{P}_i^{(2)}\right) N_i^p(\xi). \tag{3.24}$$

3.4 Isogeometric Discretisation

Isogeometric Analysis, just like classical FEM, is typically based on a Galerkin approach: the equations are written in their variational formulations, e.g. (3.10), and the solution is sought in a finite dimensional space with well defined approximation properties. The main difference between the two methodologies is

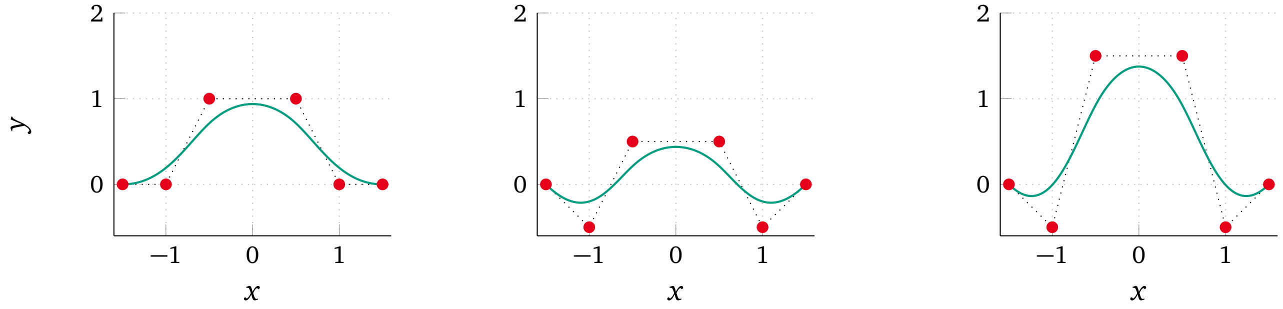

(a) A NURBS curve with control points $\{\mathbf{P}^{(1)}\}$

(b) A NURBS deformation curve with control points $\{\mathbf{P}^{(2)}\}$

(c) The deformed curve obtained with control points $\{\mathbf{P}^{(1)}+\mathbf{P}^{(2)}\}$

Figure 3.4: Deformation of NURBS objects can be obtained straightforwardly by combining the control points of the two mappings.

that in classical FEM the basis functions and the computational geometry are defined using piecewise polynomials, while in IGA the choice of the basis functions is inherited from the basis functions given by CAD. If the approximation space for the solution exactly matches the space for the geometry description, the approach is called *isoparametric*.

Let us now consider the domain $\Omega \subset \mathbb{R}^3$. We assume that this physical domain can be exactly represented through a parametrisation of the form

$$\mathbf{F} : \hat{\Omega} \to \Omega \tag{3.25}$$

where $\hat{\Omega}$ is the reference domain $[0,1]^3$, and $\mathbf{F}$ is of the type (3.23) and can be computed with the information given by CAD. We furthermore assume that $\mathbf{F}$ is piecewise smoothly invertible. It should be pointed out that commonly used CAD tools typically provide only a Boundary Representation (B-Rep), that is the objects are described in terms of their boundaries plus the notion of what is inside the domain of interest and what is not. For the IGA approach however, a full trivariate description of the computational domain is needed. In practice, the mapping $\mathbf{F}$ needs first to be constructed in a step that is the equivalent of the meshing in FEM. However, contrary to the wide variety of meshing tools, the construction of $\mathbf{F}$ is still a more or less manual process and only semi-automated procedures are available [73].

3.4.1 The de Rham Diagram

Following [25], given the mapping $\mathbf{F}$ and its Jacobian $D\mathbf{F}$, we define the pull-backs:

$$\begin{aligned}
\iota_0(v) &:= v \circ \mathbf{F} && v \in H^1\left(\hat{\Omega}\right) && \text{(3.26a)}\\
\iota_1(\mathbf{v}) &:= (D\mathbf{F})^\top (\mathbf{v} \circ \mathbf{F}) && \mathbf{v} \in \mathbf{H}\left(\mathbf{curl};\hat{\Omega}\right) && \text{(3.26b)}\\
\iota_2(\mathbf{v}) &:= \det(D\mathbf{F})\,(D\mathbf{F})^{-1} (\mathbf{v} \circ \mathbf{F}) && \mathbf{v} \in \mathbf{H}\left(\mathrm{div};\hat{\Omega}\right) && \text{(3.26c)}\\
\iota_3(v) &:= \det(D\mathbf{F})\,(v \circ \mathbf{F}) && v \in L^2\left(\hat{\Omega}\right). && \text{(3.26d)}
\end{aligned}$$

In particular, it can be proven that (3.26c) and (3.26d) preserve the curl and the divergence, respectively, from the reference domain to the physical one (see, for example, [71]). Due to this property, the following commuting de Rham diagram holds:

$$\begin{tikzcd}
\mathbb{R} \arrow[r] & H^1\left(\hat{\Omega}\right) \arrow[r, "\hat{\nabla}"] & \mathbf{H}\left(\mathbf{curl};\hat{\Omega}\right) \arrow[r, "\hat{\nabla}\times"] & \mathbf{H}\left(\mathrm{div};\hat{\Omega}\right) \arrow[r, "\hat{\nabla}\cdot"] & L^2\left(\hat{\Omega}\right) \arrow[r] & 0 \\
\mathbb{R} \arrow[r] & H^1(\Omega) \arrow[r, "\nabla"] \arrow[u, "\iota_0"] & \mathbf{H}(\mathbf{curl};\Omega) \arrow[r, "\nabla\times"] \arrow[u, "\iota_1"] & \mathbf{H}(\mathrm{div};\Omega) \arrow[r, "\nabla\cdot"] \arrow[u, "\iota_2"] & L^2(\Omega) \arrow[r] \arrow[u, "\iota_3"] & 0
\end{tikzcd} \tag{3.27}$$

and analogously for spaces with prescribed boundary conditions:

$$\begin{tikzcd}
0 \arrow[r] & H^1_0\left(\hat{\Omega}\right) \arrow[r, "\hat{\nabla}"] & \mathbf{H}_0\left(\mathbf{curl};\hat{\Omega}\right) \arrow[r, "\hat{\nabla}\times"] & \mathbf{H}_0\left(\mathrm{div};\hat{\Omega}\right) \arrow[r, "\hat{\nabla}\cdot"] & L^2\left(\hat{\Omega}\right) \arrow[r] & \mathbb{R} \\
0 \arrow[r] & H^1_0\left(\Omega\right) \arrow[r, "\nabla"] \arrow[u, "\iota_0"] & \mathbf{H}_0\left(\mathbf{curl};\Omega\right) \arrow[r, "\nabla\times"] \arrow[u, "\iota_1"] & \mathbf{H}_0\left(\mathrm{div};\Omega\right) \arrow[r, "\nabla\cdot"] \arrow[u, "\iota_2"] & L^2\left(\Omega\right) \arrow[r] \arrow[u, "\iota_3"] & \mathbb{R}.
\end{tikzcd} \tag{3.28}$$

For the correct approximation of vector fields in the case of Maxwell's equations, it is necessary to construct discrete spaces that comply to the same structure to avoid the so called *spurious modes*.

3.4.2 Conforming Discretisation of Maxwell's Eigenvalue Problem

In this section we recapitulate the notation that we will use from now on. The more interested reader can refer to [25]. In the one dimensional case, we will write

$$S^p_{\boldsymbol{\alpha}}\left(\hat{\Omega}\right) = \mathrm{span}\left\{B^p_0,\dots,B^p_{n-1}\right\}, \tag{3.29}$$

with $\boldsymbol{\alpha}_i = \left\{\alpha_0,\dots,\alpha_{n+p}\right\}$ and $\alpha_i = p - r_i$. Unless otherwise specified we will always assume to be dealing with B-Spline basis functions. An important property that is true for B-Splines is that, for $p \geq 1$ and $\alpha_i \geq 0$ $\forall i$, the derivatives of functions in $S^p_{\boldsymbol{\alpha}}$ are still B-Splines. In particular it is straightforward to see that

$$\left\{\frac{d}{dx}v \text{ s.t. } v \in S^p_{\boldsymbol{\alpha}}\right\} \equiv S^{p-1}_{\boldsymbol{\alpha}-1}. \tag{3.30}$$

It is then possible to proceed by tensor product to construct the multivariate B-Spline space:

$$S^{\mathbf{p}}_{\boldsymbol{\alpha}_1,\boldsymbol{\alpha}_2,\boldsymbol{\alpha}_3}\left(\hat{\Omega}\right) := S^{p_1}_{\boldsymbol{\alpha}_1} \times S^{p_2}_{\boldsymbol{\alpha}_2} \times S^{p_3}_{\boldsymbol{\alpha}_3}, \qquad B^{\mathbf{p}}_{ijk}(\xi_1,\xi_2,\xi_3) := B^{p_1}_i(\xi_1)B^{p_2}_j(\xi_2)B^{p_3}_k(\xi_3) \tag{3.31}$$

and define the sequence:

$$S^0\left(\hat{\Omega}\right) = S^{\mathbf{p}}_{\boldsymbol{\alpha}_1,\boldsymbol{\alpha}_2,\boldsymbol{\alpha}_3}\left(\hat{\Omega}\right) \tag{3.32}$$

$$S^1\left(\hat{\Omega}\right) = S^{p_1-1,p_2,p_3}_{\boldsymbol{\alpha}_1-1,\boldsymbol{\alpha}_2,\boldsymbol{\alpha}_3}\left(\hat{\Omega}\right) \times S^{p_1,p_2-1,p_3}_{\boldsymbol{\alpha}_1,\boldsymbol{\alpha}_2-1,\boldsymbol{\alpha}_3}\left(\hat{\Omega}\right) \times S^{p_1,p_2,p_3-1}_{\boldsymbol{\alpha}_1,\boldsymbol{\alpha}_2,\boldsymbol{\alpha}_3-1}\left(\hat{\Omega}\right) \tag{3.33}$$

$$S^2\left(\hat{\Omega}\right) = S^{p_1,p_2-1,p_3-1}_{\boldsymbol{\alpha}_1,\boldsymbol{\alpha}_2-1,\boldsymbol{\alpha}_3-1}\left(\hat{\Omega}\right) \times S^{p_1-1,p_2,p_3-1}_{\boldsymbol{\alpha}_1-1,\boldsymbol{\alpha}_2,\boldsymbol{\alpha}_3-1}\left(\hat{\Omega}\right) \times S^{p_1-1,p_2-1,p_3}_{\boldsymbol{\alpha}_1-1,\boldsymbol{\alpha}_2-1,\boldsymbol{\alpha}_3}\left(\hat{\Omega}\right) \tag{3.34}$$

$$S^3\left(\hat{\Omega}\right) = S^{\mathbf{p}-1}_{\boldsymbol{\alpha}_1-1,\boldsymbol{\alpha}_2-1,\boldsymbol{\alpha}_3-1}\left(\hat{\Omega}\right). \tag{3.35}$$

Given observation (3.30), it is possible to construct a discrete de Rham complex for the Isogeometric spaces:

$$\mathbb{R} \longrightarrow S^0\left(\hat{\Omega}\right) \xrightarrow{\hat{\nabla}} S^1\left(\hat{\Omega}\right) \xrightarrow{\hat{\nabla}\times} S^2\left(\hat{\Omega}\right) \xrightarrow{\hat{\nabla}\cdot} S^3\left(\hat{\Omega}\right) \longrightarrow 0. \tag{3.36}$$

To define the spaces in the physical domain, we use the pull-backs (3.26), that is the proper discretisation for $\mathbf{H}\left(\mathbf{curl};\Omega\right)$ is

$$S^1\left(\Omega\right) = \left\{\mathbf{v} = \hat{\mathbf{v}} \circ \iota_1^{-1}, \hat{\mathbf{v}} \in S^1\left(\hat{\Omega}\right)\right\} \tag{3.37}$$

and analogously for the other spaces. Similar considerations can be carried on for the case of Dirichlet boundary conditions.

The discretised eigenvalue problem (3.16) is obtained by choosing the discrete space in (3.12) as

$$V_h\left(\Omega\right) = S^1\left(\Omega\right). \tag{3.38}$$

Thanks to diagram (3.36), the eigenfunctions corresponding to $\omega_h = 0$ are given by gradients of functions in $S^0\left(\Omega\right)$, analogously to the continuous case. The spectral correctness and the convergence of the discrete approximation to the continuous solution is addressed in [25, 29].

3.5 Discretisation of the Linear Elasticity Problem

It is not the scope of this thesis to dwell too deeply on how to solve the mechanical problem. Suffice to say that the classical variational formulation framed in the usual Sobolev space $H^1(\Omega)$ is used: *Find the displacement* $\mathbf{u} \in H^1_{0,\Gamma_D}(\Omega)$ *such that*

$$-(\nabla \cdot \boldsymbol{\sigma}, \mathbf{v}) = 0 \qquad \forall \mathbf{v} \in \mathbf{H}^1_0(\Omega_w). \tag{3.39}$$

Some more details can be found in [31].

For the discretisation, IGA allows for a fully isoparametric approach, which in turn makes the computation of the deformed geometry easy to handle.

Let us assume that the computational domain is constructed as a single patch and that the parametrization $\mathbf{F}$ is a NURBS mapping as in (3.25). We define the discrete subspace of $H^1(\hat{\Omega})$ on the reference domain as the set of tensor product NURBS basis functions

$$W^{\mathbf{p}}_{\boldsymbol{\alpha}_1,\boldsymbol{\alpha}_2,\boldsymbol{\alpha}_3}(\hat{\Omega}) := W^{p_1}_{\boldsymbol{\alpha}_1} \times W^{p_2}_{\boldsymbol{\alpha}_2} \times W^{p_3}_{\boldsymbol{\alpha}_3}, \qquad N^{\mathbf{p}}_{ijk}(\xi_1,\xi_2,\xi_3) := N^{p_1}_i(\xi_1) N^{p_2}_j(\xi_2) N^{p_3}_k(\xi_3). \tag{3.40}$$

These are transformed to the physical domain using mapping ι_0:

$$W(\Omega) = \left\{\mathbf{v} = \hat{\mathbf{v}} \circ \iota_0^{-1}, \hat{\mathbf{v}} \in W(\hat{\Omega})\right\} \tag{3.41}$$

By restricting weak problem (3.39) to trial functions in $W(\Omega)$ and projecting the displacement $\mathbf{u}$:

$$\mathbf{u} \approx \mathbf{u}_h = \sum_j u_j \mathbf{w}_j \qquad \mathbf{w}_j \in W(\Omega), \tag{3.42}$$

we get to the linear system of equations

$$\mathbf{A}\mathbf{u} = \mathbf{f}, \tag{3.43}$$

where $\mathbf{A}$ is the stiffness matrix given by the stresses and $\mathbf{f}$ is the source term given by the electromagnetic pressure on the internal wall.

The isoparametric concept prescribes to choose as the basis functions for the space $W(\hat{\Omega})$ the same basis functions used to define the geometry and its map $\mathbf{F}$. This implies that the discrete solution $\mathbf{u}_h$ belongs to the same space of the geometry mapping. In particular, if the wall geometry is defined as

$$\Omega_{\mathrm{w}} = \mathbf{F}\left([0,1]^3\right) = \sum_{\mathbf{i} \in \mathscr{I}} \mathbf{P}_{\mathbf{i}} N^{\mathbf{p}}_{\mathbf{i}}(\xi), \tag{3.44}$$

over a set of N control points, then the solution $\mathbf{u}_h$ will have $3N$ degrees of freedom u_j which can be rearranged according to the three spatial components to create a set of N displacement control points $\mathbf{Q}_\mathbf{i}$. The deformed walls map can then be straightforwardly obtained as

$$\Omega'_{\mathrm{w}} = \mathbf{F}'\left([0,1]^3\right) = \sum_{\mathbf{i} \in \mathscr{I}} (\mathbf{P}_{\mathbf{i}} + \mathbf{Q}_{\mathbf{i}}) N^{\mathbf{p}}_{\mathbf{i}}(\xi). \tag{3.45}$$

3.6 Multipatch Formulation

When it is necessary to treat complicated geometries, a single mapping is often not sufficient for its construction or, albeit possible, it is at least inconvenient. Multipatch can describe the most complex geometries or can be applied to situations in which multiple material models are present.

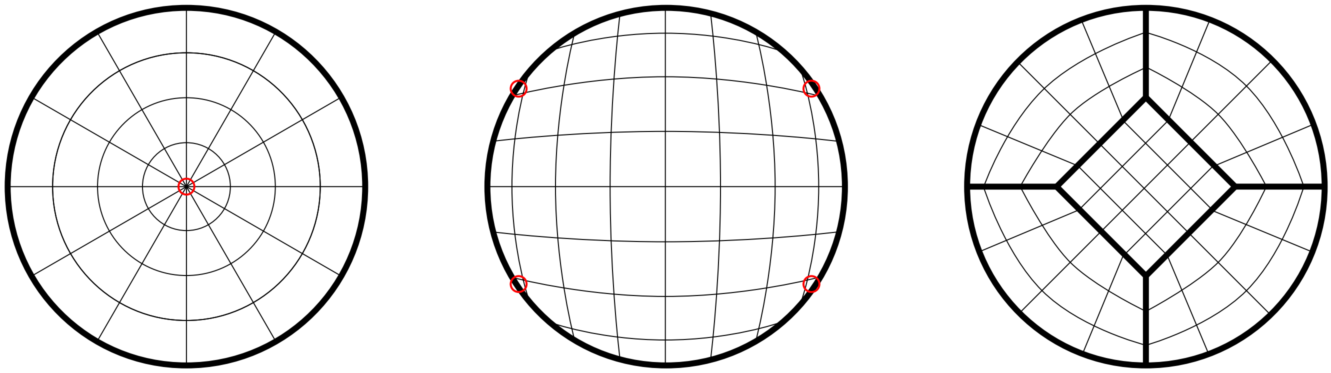

Figure 3.5: Different NURBS parametrisation of a circle. The first possibilty is to let one edge of the reference domain collapse in the centre (figure on the left); a second possibility is a mapping with singular Jacobian at the four corners (in the centre). The red circles highlight the location of the singularities. On the right the 5-patch map chosen with no critical points.

For example, in parametrising the geometries for both the pill-box cavity and for the TESLA cavity, that are the focus of the present work, we have chosen to use a multipatch approach in order to avoid singularities in the geometrical mapping. The parametrisation of the circle, and as a consequence of any cylindrical domain, as a single patch introduces either a collapsed edge or singularities in 4 points along the circumference (which becomes 4 lines when extruded to obtain cylindrical shapes) [7]. Figure 3.5 shows the two singular cases and the multipatch solution applied in this work.

In a multipatch approach the domain geometry is partitioned into N_{mp} subregions as

$$\overline{\Omega} \equiv \bigcup_{i=1}^{N_{\mathrm{mp}}} \overline{\Omega}_i \qquad\qquad \Omega_i \cap \Omega_j = \emptyset \qquad \forall i \neq j \tag{3.46}$$

where each of the patches consists of a smooth mapping with smooth inverse of the reference domain $\hat{\Omega}$

$$\Omega_W \equiv \mathbf{F}_i(\hat{\Omega}), \tag{3.47}$$

each of the mappings $\mathbf{F}_i$ being defined in terms of NURBS basis functions as in (3.22)-(3.23). We require that two neighbouring patches share one full face and we denote the interface by

$$\Gamma_{ij} \equiv \overline{\Omega}_i \cap \overline{\Omega}_j. \tag{3.48}$$

The resulting overall geometrical mapping is globally continuous but only piecewise smooth.

For the Maxwell eigenproblem the unknowns $\mathbf{E}_i$ are introduced and the problem to be solved in each patch becomes

$$\nabla \times \nabla \times \mathbf{E}_i = \omega_0^2 \mu_0 \varepsilon_0 \mathbf{E}_i \qquad \text{in } \Omega_i \tag{3.49}$$

with the interface conditions

$$\mathbf{E}_i \times \mathbf{n}_i = \mathbf{E}_j \times \mathbf{n}_i \qquad\qquad \text{on } \Gamma_{ij} \tag{3.50a}$$

$$\left(\mu_0^{-1} \nabla \times \mathbf{E}_i\right) \times \mathbf{n}_i = -\left(\mu_0^{-1} \nabla \times \mathbf{E}_j\right) \times \mathbf{n}_i \qquad\qquad \text{on } \Gamma_{ij}. \tag{3.50b}$$

with $\mathbf{n}_i$ the outward normal vector with respect to the i-th patch.

For the linear elasticity problem (2.52) a new set of unknowns $\mathbf{u}_i$ is introduced, such that $\mathbf{u}|_{\Omega_i} = \mathbf{u}_i$ solution of the problem

$$\nabla \cdot \left(2\eta \nabla^{(S)} \mathbf{u}_i + \lambda \mathbf{I} \nabla \cdot \mathbf{u}_i\right) = 0 \qquad \text{in } \Omega_{W,i} \tag{3.51}$$

and the overall problem is recovered by imposing continuity of the displacements and normal stresses at the patch interfaces

3.7 Summary

Starting from the continuous formulation of Maxwell's eigenvalue problem (2.28) and of the linear elasticity problem (2.52), we have derived their weak formulation by introducing proper Sobolev spaces with well defined gradient, divergence and curl in L^2. These spaces satisfy the de Rham complex given in (3.27). For the discretisation, instead of a finite element approach, IGA has been introduced. This required the definition of B-Spline and NURBS basis functions and of appropriate mappings from the reference domain to the physical domain. The discrete spaces obtained are embedded in the same structure as the continuous ones. Finally, it has been explained how to treat complex geometries by using multiple patches.

The strong relation between IGA and CAD design allows for the exact description of geometries which is highly beneficial when the shape has a strong impact on the accuracy of the solution. Furthermore, it renders the treatment of geometry deformation straightforward without any need of remeshing steps. In the next chapter we consider the case of uncertain geometry shapes and introduce UQ methods that are employed for the analysis of PDE with uncertain inputs.

4 Uncertainty Quantification for the Eigenvalue Problem

Let's assume we have a PDE,
with inputs allowed to run free.
A method is there
that you should be aware:
Monte Carlo is not only a Grand Prix!

In practical application, when designing a cavity, expert knowledge, physics considerations and feasibility constraints are exploited to reduce the number of variables and obtain a final design that complies with the required specifications, e.g. the fundamental frequency or the accelerating gradient. A full automatic optimisation procedures would be desirable, but, given the huge number of parameters (see Table 2.1), this is computationally too expensive. One possible solution is the application of UQ and sensitivity analysis to identify the parameters with the highest impact on the objective function [87]. The computation of eigenmodes sensitivities can also be used to ensure that the optimised cavity design is robust with respect to small perturbations. The computation of these sensitivities and of other stochastic moments for the eigenmodes of a cavity subject to geometry deformations falls into the field of UQ methods.

Cavity optimisation is, however, not only applicable to new cavity design. Due to the manufacturing process, the cavities that are put into operation are often sufficiently different from the design. For a TESLA cavity half-cell production, for example, tolerances on the shape are usually set at approximately $\pm 0.4\,\mathrm{mm}$ [60], while the welded cavity, whose total design length (excluding the beampipes at both ends) is $1010.7\,\mathrm{mm}$, can have variations of up to $\pm 2\,\mathrm{mm}$ [63]. The impact of these manufacturing imperfections is so relevant that in the design phase cavities are not optimised for frequency and for field flatness since a tuning process (see section 2.3.4) is nevertheless required.

The mathematical models that have been so far introduced follow a deterministic approach. This means that the input data, i.e. the cavity geometry, is considered to be given and that the model associates a solution to each specific input. Real life devices, however, present uncertainties that are typically categorised into two subsets: manufacturing imperfections regarding, for example, the final shape or the material properties are usually referred to as *aleatory uncertainties*, while we talk about *epistemic uncertainties* when we refer to the model itself not being necessarily a precise depiction of the underlying physics, either due to approximations or unknown quantities. As a consequence of this, both the model inputs and the model equations exhibit uncertainties and it has become more and more a necessity, in modern computational engineering, to evaluate the impact of these on the quantities of interest of a given problem.

In the following chapter, we introduce some methods designed for the modelling of random input data, with particular focus on the case of uncertain shape, and for the evaluation of stochastic moments of quantity of interests obtained from the solution of a system of PDEs given those uncertain inputs. In the last section we present a method of tracking the solution of the eigenvalue problem in the random parameter space to ensure accuracy of the results.

4.1 Random Input Parameters

Given the eigenmodes in a cavity Ω, $(\omega_n, \underline{\mathbf{E}}_n)$, we are interested in the quantification of the sensitivity of a specific quantity of interest $\mathcal{Q}(\omega, \underline{\mathbf{E}})$, e.g. the eigenfrequency of the accelerating mode f_0, with respect to changes of a parameter q defining the geometry. We can then define classical (local) sensitivities as

$$\mathbf{D}_q \mathcal{Q}(\omega, \mathbf{E}) = \frac{\partial \mathcal{Q}(\omega(q), \mathbf{E}(q))}{\partial q}. \tag{4.1}$$

In the case of a pillbox cavity, for example, the shape is given in terms of the radius R and the length L (see Fig. 2.3). The accelerating mode eigenfrequency is given by equation (2.34) and it only depends on the radius R. The sensitivity of the angular frequency can then be computed analytically:

$$\mathbf{D}_R \omega_{010} = -\frac{\chi_{01} c}{R^2}. \tag{4.2}$$

We are now interested in the situation where the input geometrical parameter is uncertain and can be described as a random variable with a certain probability distribution function. The aim is to propagate the uncertainty through the PDE and to compute statistics on the (now uncertain) outputs.

Let us then introduce a probability space $(\Theta, \mathscr{F}, \mathrm{P})$ with Θ the sample space of possible outcomes, $\mathscr{F}$ the σ-algebra associated to it and P a probability measure. Let $\theta \in \Theta$ be a random event and $\mathbf{Y}(\theta)$ a vector containing N independent random input parameters $Y_i(\theta)$, with a certain probability density function $\varrho(\mathbf{y})$. In our case, each possible realisation $\mathbf{y} = \mathbf{Y}(\theta)$ represents a shapes of the cavity, i.e. $\Omega = \Omega(\mathbf{y})$. We assume that Maxwell's eigenproblem (2.28) is well defined for all possible realisations $\mathbf{y}$. The solution of the eigenvalue problem is in itself a random variable depending on the random event θ

$$\omega_j = \omega_j(\mathbf{y}) \qquad \mathbf{E}_j = \mathbf{E}_j(\mathbf{y}). \tag{4.3}$$

The question is then how the input uncertainty affects the quantity of interest $\mathcal{Q}(\omega, \mathbf{E})$, e.g., a cavity's eigenfrequency. A typical measure is given by stochastic moments, e.g. the expected value and the variance

$$\mathbb{E}(\mathcal{Q}) = \int_{-\infty}^{\infty} \mathcal{Q}(\omega(\mathbf{y}), \mathbf{E}(\mathbf{y})) \varrho(\mathbf{y}) d\mathbf{y} \tag{4.4a}$$

$$\sigma^2(\mathcal{Q}) = \int_{-\infty}^{\infty} \left(\mathcal{Q}(\omega(\mathbf{y}), \mathbf{E}(\mathbf{y})) - \mathbb{E}(\mathcal{Q})\right)^2 \varrho(\mathbf{y}) d\mathbf{y} \tag{4.4b}$$

or the standard deviation $\mathrm{std}(\mathcal{Q}) := \sqrt{\sigma^2(\mathcal{Q})}$. However, those integrals can rarely be solved exactly and thus one relies on numerical methods.

In the particular case of interest for this thesis, the random input parameters $\mathbf{y}$ represent possible realisations of the shape of a resonating cavity. In the simplest case the y_i correspond to one or more of the design parameter that define the shape. For example, the TESLA cavity is defined in terms of 7 parameters per half-cell, for a total of 126 values (see 2.7). Any combination of these can be used as a random input for the model [87].

It is often the case, however, that the deformations that occur in real life devices are more complicated, often disrupting the symmetry of the domain or being correlated, making the analysis more cumbersome. One possible way to treat this case is the so called Karhunen–Loève expansion (sometimes also called, in the discrete case, Principal Component Analysis (PCA)).

4.2 Discrete Karhunen–Loève Expansion

Let us assume that we have measured M times the geometric variations and that each of these observations can be described by an N-dimensional vector $\mathbf{y}_m = \begin{bmatrix} y_{m,1} & y_{m,2} & \dots & y_{m,N} \end{bmatrix}^\top$ $(m = 1, \dots, M)$. And let us further assume that all components are normally distributed but possibly mutually correlated. The vector $\boldsymbol{\mu} = \{\mu_i\}$ denotes the expectation and is computed from the M measurement samples.

We aim to convert the observations into a (possibly smaller) set of uncorrelated variables. The first step is the collection of all the observations in the matrix $\mathbf{T} \in \mathbb{R}^{M \times N}$

$$\mathbf{T} = \begin{bmatrix} \mathbf{y}_1 & \mathbf{y}_2 & \dots & \mathbf{y}_M \end{bmatrix}^\top, \tag{4.5}$$

whose columns are the random variables and whose rows are the measured observations. The covariance matrix is the matrix $\boldsymbol{\Sigma} \in \mathbb{R}^{N \times N}$ whose elements c_{ij} are defined as

$$c_{ij} := \operatorname{cov}\left(\mathbf{y}_i, \mathbf{y}_j\right) = \mathbb{E}\left[(\mathbf{y}_i - \mu_i)(\mathbf{y}_j - \mu_j)\right] \qquad i, j = 1, \dots, N \tag{4.6}$$

The main idea [37] is to construct a decomposition of the covariance matrix such that

$$\boldsymbol{\Sigma} = \mathbf{Z}\mathbf{Z}^\top. \tag{4.7}$$

There are many possible choices for matrix $\mathbf{Z}$ (for example the Cholesky factorisation), but we focus on the eigendecomposition

$$\boldsymbol{\Sigma} = \mathbf{V}\mathbf{D}\mathbf{V}^\top, \tag{4.8}$$

where the columns of $\mathbf{V}$ are the orthonormal right eigenvectors of $\boldsymbol{\Sigma}$, and $\mathbf{D} = \operatorname{diag}(d_1, d_2, \dots, d_N)$ is a diagonal matrix whose elements are the corresponding eigenvalues. It is easy to prove that $\boldsymbol{\Sigma}$ is a symmetric positive definite matrix, thus the eigenvalues are all positive and real valued. Without loss of generality we can also assume that the columns of $\mathbf{D}$ and $\mathbf{V}$ are ordered in such a way that $d_1 \geq d_2 \geq \dots \geq d_N$.

Equation (4.8) corresponds to choosing

$$\mathbf{Z}_{\mathrm{KL}} := \mathbf{V}\mathbf{D}^{1/2} \tag{4.9}$$

and it is easy to see that the decomposition introduced can be exploited to express any random vector with mean $\boldsymbol{\mu}$ and variance $\boldsymbol{\sigma}^2$ as

$$\tilde{\mathbf{y}} = \boldsymbol{\mu} + \mathbf{Z}_{\mathrm{KL}} \boldsymbol{\epsilon}(\theta), \tag{4.10}$$

where $\boldsymbol{\epsilon}(\theta)$ is an N-dimensional vector whose components are independent and identically distributed (i.i.d.) samples $\sim \mathcal{N}(0, 1)$. Expression (4.10) is often referred to as discrete Karhunen–Loève expansion and $\tilde{\mathbf{y}}$ can be interpreted as a first order approximation of the randomness of the measured variables.

One useful property of eigendecomposition (4.8) is that the stronger the correlation between the variables, the faster the eigenvalues decay. It is then possible to introduce a further approximation by truncating the decomposition to a dimension $N_\mathrm{t} < N$

$$\mathbf{Z}_{\mathrm{tKL}} := \mathbf{V}_\mathrm{t}\mathbf{D}_\mathrm{t}^{1/2} \tag{4.11}$$

where $\mathbf{Z}_{\mathrm{tKL}}$ is now a rectangular matrix of dimensions $N \times N_\mathrm{t}$. The matrix $\mathbf{V}_\mathrm{t}$ consists of the first N_t eigenvectors only, while the matrix $\mathbf{D}_\mathrm{t}$ is the $N_\mathrm{t} \times N_\mathrm{t}$ north-west block of $\mathbf{D}$.

Now we can introduce the truncated discrete Karhunen–Loève expansion

$$\tilde{\mathbf{y}}_\mathrm{t} = \boldsymbol{\mu} + \mathbf{Z}_{\mathrm{tKL}}\boldsymbol{\epsilon}_\mathrm{t}(\theta) \approx \mathbf{y}, \tag{4.12}$$

where the vector $\boldsymbol{\epsilon}_\mathrm{t}(\theta)$ is now of reduced dimension N_t. The random variable $\tilde{\mathbf{y}}_\mathrm{t}$ will still have the mean value $\boldsymbol{\mu}$ but covariance matrix

$$\boldsymbol{\Sigma}_\mathrm{t} := \mathbf{V}_\mathrm{t}\mathbf{D}_t\mathbf{V}_\mathrm{t}^\top \approx \boldsymbol{\Sigma}. \tag{4.13}$$

The faster the eigenvalues of $\boldsymbol{\Sigma}$ decay, the smaller N_t can be selected with respect to N for the same accuracy. In practice, N_t is often chosen so that the considered eigenvalues represent at least 95 % of the total, i.e. N_t is such that

$$\sum_{i=1}^{N_\mathrm{t}} d_i \geq \frac{95}{100}\sum_{i=1}^{N} d_i. \tag{4.14}$$

In many cases, instead of extracting the reduced system from the complete eigendecomposition, the matrices $\mathbf{V}_\mathrm{t}$ and $\mathbf{D}_\mathrm{t}$ are obtained through a truncated Singular Value Decomposition (SVD).

The process introduced can be used to significantly reduce the number of random inputs for the UQ analysis which, as it will be shown in the following sections, can have a huge impact on the performance.

4.3 Numerical Integration of Stochastic Moments

One way to evaluate the statistical moments 4.4 is numerical integration. Here we present two approaches that are commonly used.

4.3.1 Monte Carlo Sampling

A first approach to numerically estimate integrals (4.4), is the well-known Monte Carlo (MC) sampling method [67]. In this case problem (2.28) is solved M times, for M random realizations $\mathbf{y}_m$ (see Fig. 4.1a). The results obtained for the angular velocity ω_n and the electric field $\underline{\mathbf{E}}_n$ are then used to estimate expectation values of the desired quantity of interest by sample averages:

$$\mathbb{E}(\mathcal{Q}) \approx \frac{1}{M}\sum_{i=1}^{M} \mathcal{Q}\big(\omega(\mathbf{y}_i), \underline{\mathbf{E}}(\mathbf{y}_i)\big). \tag{4.15}$$

Among the advantages of MC methods there is the fixed convergence rate to the exact values that scales as $M^{1/2}$ regardless of the number of random parameters. However, the convergence is rather slow even when the solution has very smooth variation with respect to the parameter changes. More sophisticated methods like quasi Monte Carlo [42] or multilevel Monte Carlo [54] are available to mitigate this issue.

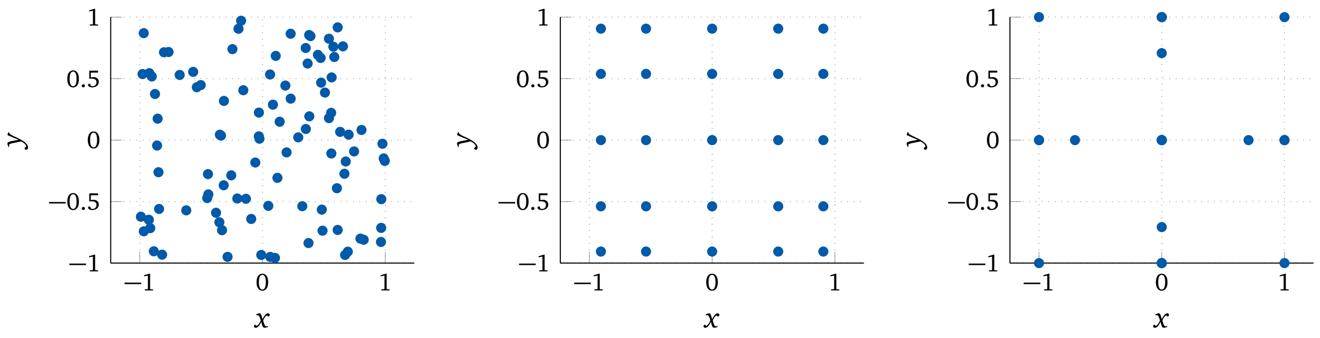

(a) Monte Carlo points. **(b)** Gaussian tensor product points. **(c)** Sparse Clenshaw-Curtis grid of level 2.

Figure 4.1: Some examples of different choices of collocation points in a two dimensional random parameter space: Monte Carlo points (a), Gaussian tensor product points (b), level 2 Clenshaw-Curtis points (c).

4.3.2 Stochastic Collocation

The main idea of stochastic collocation methods, in an analogous way of that which is performed for classical numerical quadrature, is to choose points $\mathbf{y}_m$ in the parameter space in a more clever way than just randomly like in Monte Carlo, e.g. Gaussian points. By exploiting the solution regularity one can increase the speed of convergence by approximating the mapping from parameter to solution space by polynomials of degree p. Depending on the context, this method may also be referred to as generalised Polynomial Chaos (gPC) [100].

Depending on the distribution of the input variables (uniformly, normally, etc...), the approximation is constructed by creating a basis of orthonormal polynomials $\{\psi_i(\mathbf{y})\}_0^p$ and a grid of points $\mathbf{y}_i$ in the parameter space called *collocation points* [100], i.e.

$$\mathcal{Q}(\omega(\mathbf{y}),\mathbf{E}(\mathbf{y})) \approx \sum_{i=0}^{p} \mathcal{Q}\big(\omega(\mathbf{y}_i),\mathbf{E}(\mathbf{y}_i)\big)\,\psi_i(\mathbf{y}). \tag{4.16}$$

The integrals in (4.4) can then be computed as

$$\mathbb{E}(\mathcal{Q}) \approx \sum_i \mathcal{Q}\big(\omega(\mathbf{y}_i),\mathbf{E}(\mathbf{y}_i)\big)\,w_i \tag{4.17a}$$

$$\mathrm{var}(\mathcal{Q}) \approx \sum_i \Big(\mathcal{Q}\big(\omega(\mathbf{y}_i),\mathbf{E}(\mathbf{y}_i)\big) - \mathbb{E}(\mathcal{Q})\Big)^2 w_i, \tag{4.17b}$$

where to each collocation point $\mathbf{y}_i$ we have associated a quadrature weight w_i. If the exact solution has a sufficiently smooth dependency with respect to its parameters this method converges exponentially [100].

The construction of these collocation points typically follows a tensor product approach, i.e. they are chosen independently for each variable and then multiplied in the multivariate case (see Fig. 4.1b). The direct consequence of this is the exponential growth of the quadrature points with the number of random variable N (the so called *curse of dimensionality*). One possible way to reduce this effect is the use of sparse grids [28] which construct the collocation points in a more clever way. Many different rules for constructing such grids have been proposed in literature based on the Clenshaw-Curtis rule (see Fig. 4.1c). We refer the interested reader to [5, 28, 75, 76].

Each collocation point requires the solution of the deterministic eigenvalue problem (2.28) and the number of points grows rapidly with N. As explained in section 4.2, the use of truncated Karhunen–Loève expansion can reduce the numerical cost by reducing the number of random dimensions.

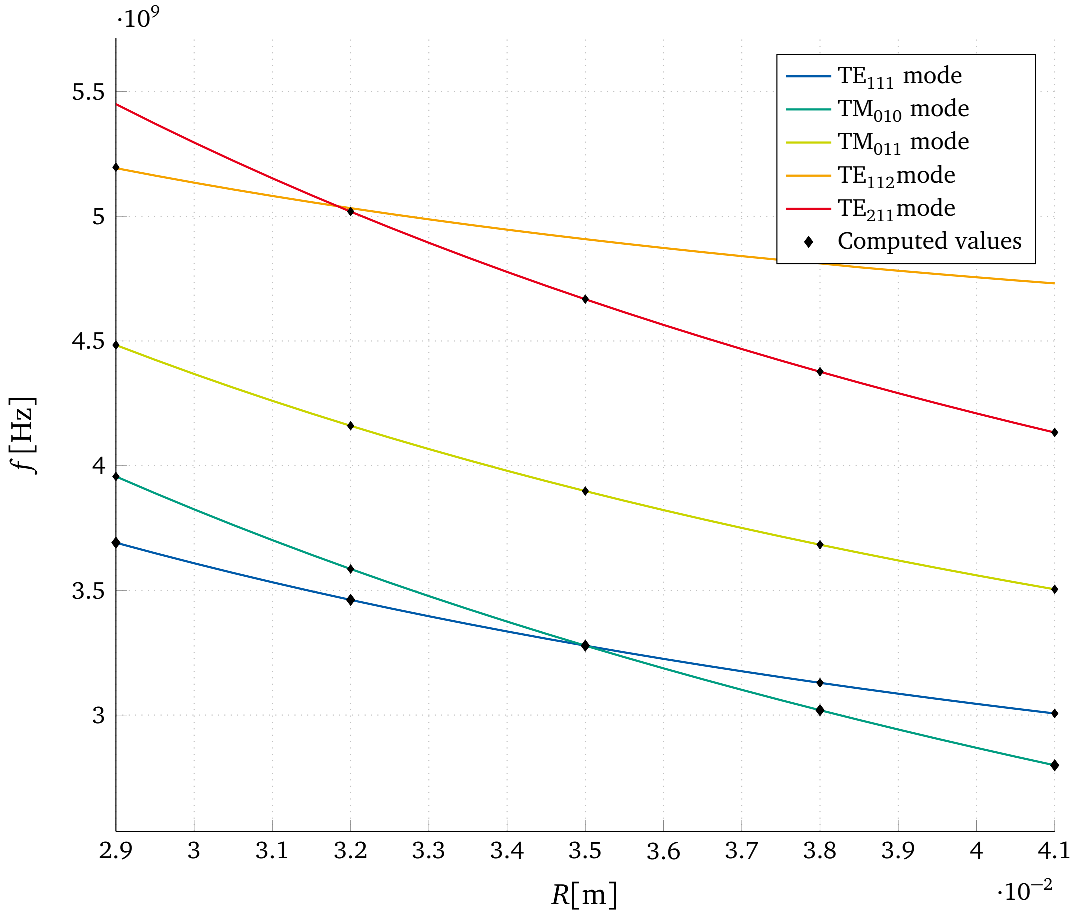

Figure 4.2: First five eigenfrequencies in a pill-box cavity of length $L = 71\,\text{mm}$ and radius $R \in [29, 41]\text{mm}$. Continuous lines show the analytical solutions, while markers are the computed solutions at discrete points. The natural ordering of the computed eigenvalues is unable to identify eigenmode crossings.

4.4 Eigenvalue Tracking

When dealing with uncertain inputs, the derivation of the discrete generalised eigenvalue problem (3.16) is still valid, but the parameter dependency of the geometry $\Omega(\mathbf{y})$ propagates via the mapping (3.25) to the stiffness and mass matrices **K** and **M** and to the eigenmode solution (see Eq. 3.16):

$$\mathbf{K}(\mathbf{y})\mathbf{v}(\mathbf{y}) = \lambda(\mathbf{y})\mathbf{M}(\mathbf{y})\mathbf{v}(\mathbf{y}). \tag{4.18}$$

It should be noted that since $\mathbf{K}(\mathbf{y})$ and $\mathbf{M}(\mathbf{y})$ are still matrices built through the IGA approximation introduced in chapter 3, they are symmetric positive definite matrices with real valued eigenvalues $\lambda(\mathbf{y})$.

Traditional eigenvalue solvers do not deal with parameter dependent matrices, therefore it is only possible to solve the eigenvalue problem at discrete sample points in the parameter space. A consistent ordering of the eigenvalues in the parameter space is not guaranteed. Let us consider, once again, the case of the pill-box cavity with radius R varying in a range $[R_{min}, R_{max}]$ and fixed length L. Solving the eigenvalue problem for discrete values of the radius does not give information on possible eigenvalue crossings and may suggest a completely wrong dependency of the eigenmodes on the parameter R. This case is depicted in Figure 4.2. The correct ordering of eigenmodes may be important for cavity design, for post-processing applications, or to obtain correct statistical measures.

Following [52], we assume that the dependency of the eigenvalues on the parameters is smooth, which is a reasonable assumption for the case of simply connected geometries not subjected to topological changes, and the eigenvalues of the system can be traced. Given two different configurations $\mathbf{y}_0$ and $\mathbf{y}_1$, corresponding to two different cavity shapes $\Omega_0 = \Omega(\mathbf{y}_0)$ and $\Omega_1 = \Omega(\mathbf{y}_1)$, it is possible to construct an algebraic homotopy from e.g. $\mathbf{y}_0$ to $\mathbf{y}_1$:

$$\mathbf{y}(s) = (1-s)\mathbf{y}_0 + s\mathbf{y}_1, \tag{4.19}$$

where $s \in [0,1]$. This mapping allows for the reduction of the dependency of the uncertain quantities from N parameters to the scalar quantity s, which makes the following one-dimensional analysis feasible. Homotopies different than (4.19) could be analogously defined, e.g. such that the eigenvalue problems for $0 < s < 1$ does not correspond to real geometries.

In the UQ setting introduced above, a set of discrete points $\mathbf{y}_k$ is given in the parameter space. These points could be randomly distributed, uniformly distributed or could follow a more clever scheme (see section 4.3.2). Given a reference configuration $\mathbf{y}_0$ (e.g. corresponding to an unperturbed geometry), we construct for each point $\mathbf{y}_k$ an homotopy like the one in (4.19), from $\mathbf{y}_0$ to $\mathbf{y}_k$. The stiffness and mass matrices are then dependent only on the parameter s:

$$\mathbf{K}_{k,s} := (1-s)\mathbf{K}(\mathbf{y}_0) + s\mathbf{K}(\mathbf{y}_k) \tag{4.20a}$$

$$\mathbf{M}_{k,s} := (1-s)\mathbf{M}(\mathbf{y}_0) + s\mathbf{M}(\mathbf{y}_k). \tag{4.20b}$$

It is worth mentioning that this step is allowed only if

$$\dim(\mathbf{K}(\mathbf{y}_k)) = \dim(\mathbf{M}(\mathbf{y}_k)) = const. \tag{4.21}$$

With a classical FEM mesh, this condition may not be ensured if for each k the mesh is recomputed from scratch: the transformation of the mesh to accommodate the deformed geometry should preserve the number of elements and this process may not be straightforward if the shape changes are non trivial. In the IGA approach, however, condition (4.21) is automatically verified since the mesh partitioning is directly inherited from the domain mapping.

The algebraically motivated homotopy (4.20) allows for the straightforward definition of the derivatives, i.e.

$$\mathbf{K}'_{k,s} = \frac{\partial}{\partial s}\mathbf{K}_{k,s} = \mathbf{K}(\mathbf{y}_k) - \mathbf{K}(\mathbf{y}_0) \tag{4.22a}$$

$$\mathbf{M}'_{k,s} = \frac{\partial}{\partial s}\mathbf{M}_{k,s} = \mathbf{M}(\mathbf{y}_k) - \mathbf{M}(\mathbf{y}_0) \tag{4.22b}$$

For each point k and eigenpair j, the eigenvalue problem (4.18) can be rewritten as a linear system of equations with a normalization constraint using a vector $\mathbf{c}$ such that $\mathbf{c}^\top \mathbf{e}_s \neq 0$

$$\begin{bmatrix} \mathbf{K}_s\mathbf{e}_s - \lambda_s\mathbf{M}_s\mathbf{e}_s \\ \mathbf{c}^\top\mathbf{e}_s - 1 \end{bmatrix} = \begin{bmatrix} 0 \\ 0 \end{bmatrix}, \tag{4.23}$$

where $\lambda_s := \lambda_j(\mathbf{y}_k(s))$ and $\mathbf{e}_s := \mathbf{e}_j(\mathbf{y}_k(s))$. The subscripts j and k addressing eigenpair number and collocation point are suppressed for readability, i.e. we consider the point in the parameter space and the eigenpair to be fixed. The second equation in (4.23) is a normalisation constraint for the eigenvector [68].

Let us now consider a Taylor expansion with respect to s at point s_0

$$\begin{bmatrix} \tilde{\mathbf{e}}_s \\ \tilde{\lambda}_s \end{bmatrix} = \begin{bmatrix} \mathbf{e}_0 \\ \lambda_0 \end{bmatrix} + (s - s_0)\begin{bmatrix} \mathbf{e}'_0 \\ \lambda'_0 \end{bmatrix} + \dots \tag{4.24}$$

which gives, after truncation, a first-order approximation for the eigenpair $\begin{bmatrix}\tilde{\mathbf{e}}_s & \tilde{\lambda}_s\end{bmatrix}^\top \approx \begin{bmatrix}\mathbf{e}_s & \lambda_s\end{bmatrix}^\top$ at $\mathbf{y}_k(s)$. The derivatives $\begin{bmatrix}\mathbf{e}'_0 & \lambda'_0\end{bmatrix}^\top$ of the eigenvalues and eigenvectors are obtained from Equation (4.23) which can be differentiated with respect to the parameter s. The resulting linear system

$$\begin{bmatrix}\mathbf{K}_0 - \lambda_0 \mathbf{M}_0 & -\mathbf{M}_0 \mathbf{e}_0 \\ \mathbf{c}^\top & 0\end{bmatrix}\begin{bmatrix}\mathbf{e}'_0 \\ \lambda'_0\end{bmatrix} = \begin{bmatrix}-\mathbf{K}'_0 \mathbf{e}_0 + \lambda \mathbf{M}'_0 \mathbf{e}_0 \\ 0\end{bmatrix} \tag{4.25}$$

is solved with respect to the eigenvalue and eigenvector derivatives.

The predicted eigenpair $\begin{bmatrix}\tilde{\mathbf{e}}_s & \tilde{\lambda}_s\end{bmatrix}^\top$ can then be used as an initial guess

$$\begin{bmatrix}\mathbf{e}_s^{(0)} & \lambda_s^{(0)}\end{bmatrix}^\top := \begin{bmatrix}\tilde{\mathbf{e}}_s & \tilde{\lambda}_s\end{bmatrix}^\top \tag{4.26}$$

for a Newton-Raphson method in order to obtain a better approximation of the exact eigenpair $\begin{bmatrix}\mathbf{e}_s & \lambda_s\end{bmatrix}^\top$. Higher order predictions can be used, depending on the truncation choice in (4.24).

At the i-th iteration the Newton-Raphson scheme requires the solution of the linear system of equations

$$\begin{bmatrix}\mathbf{K}_s - \lambda_s^{(i-1)} \mathbf{M}_s & -\mathbf{M}_s \mathbf{e}_s^{(i-1)} \\ \mathbf{c}^\top & 0\end{bmatrix}\begin{bmatrix}\Delta \mathbf{e}_s^{(i)} \\ \Delta \lambda_s^{(i)}\end{bmatrix} = -\begin{bmatrix}\mathbf{K}_s \mathbf{e}_s^{(i-1)} - \lambda_s^{(i-1)} \mathbf{M}_s \mathbf{e}_s^{(i-1)} \\ \mathbf{c}^\top \mathbf{e}_s^{(i-1)} - 1\end{bmatrix} \tag{4.27}$$

with the increments $\Delta \mathbf{e}_s^{(i)}$ and $\Delta \lambda_s^{(i)}$. The prediction is then iteratively improved by assigning

$$\begin{bmatrix}\mathbf{e}_s^{(i)} \\ \lambda_s^{(i)}\end{bmatrix} := \begin{bmatrix}\mathbf{e}_s^{(i-1)} \\ \lambda_s^{(i-1)}\end{bmatrix} + \begin{bmatrix}\Delta \mathbf{e}_s^{(i)} \\ \Delta \lambda_s^{(i)}\end{bmatrix}. \tag{4.28}$$

As a termination criterion for the Newton-Raphson method, the norm of the residual of the eigenvalue problem (4.23) can be considered as well as the norm of $\Delta \lambda_s^{(i)}$. The required number of Newton iterations can be used for a stepsize control in order to increase the efficiency and robustness of the algorithm. In Fig. 4.3 the algorithm proposed is depicted in a flowchart.

It is relevant to note that the tracing method proposed no longer requires the solution of an eigenvalue problem at each point $\mathbf{y}$ in the parameter space, but only in the reference configuration $\mathbf{y}_0$. However the cost of applying Newton algorithm for each eigenvalue and for each step in the tracing needs to be taken into account. Finally, it is worth mentioning that the choice of the reference configuration $\mathbf{y}_0$ may play an important role in the accuracy of the method: in many cases it is better to choose a point $\mathbf{y}_0$ far from the unperturbed shape since, given the symmetry of the domain, many of the eigenmodes may be degenerate and difficult to distinguish between each other.

4.5 Summary

Given a PDE model with random input parameters, it has been shown how to compute stochastic moments of quantity of interests obtained from the solution using numerical quadrature. The methods proposed are non-invasive and only require solving the problem for different realisations of the input parameters. In the case of RF cavities it is however paramount to be able to correctly identify the different modes obtained for each of these realisations. An algorithm for the tracking of the eigenmodes has been proposed.

In the following chapter we discuss some methods that exploit the typical cavity modularity to speed up the matrix calculations and to allow for different discretisation strategies to be employed in different parts of the device.

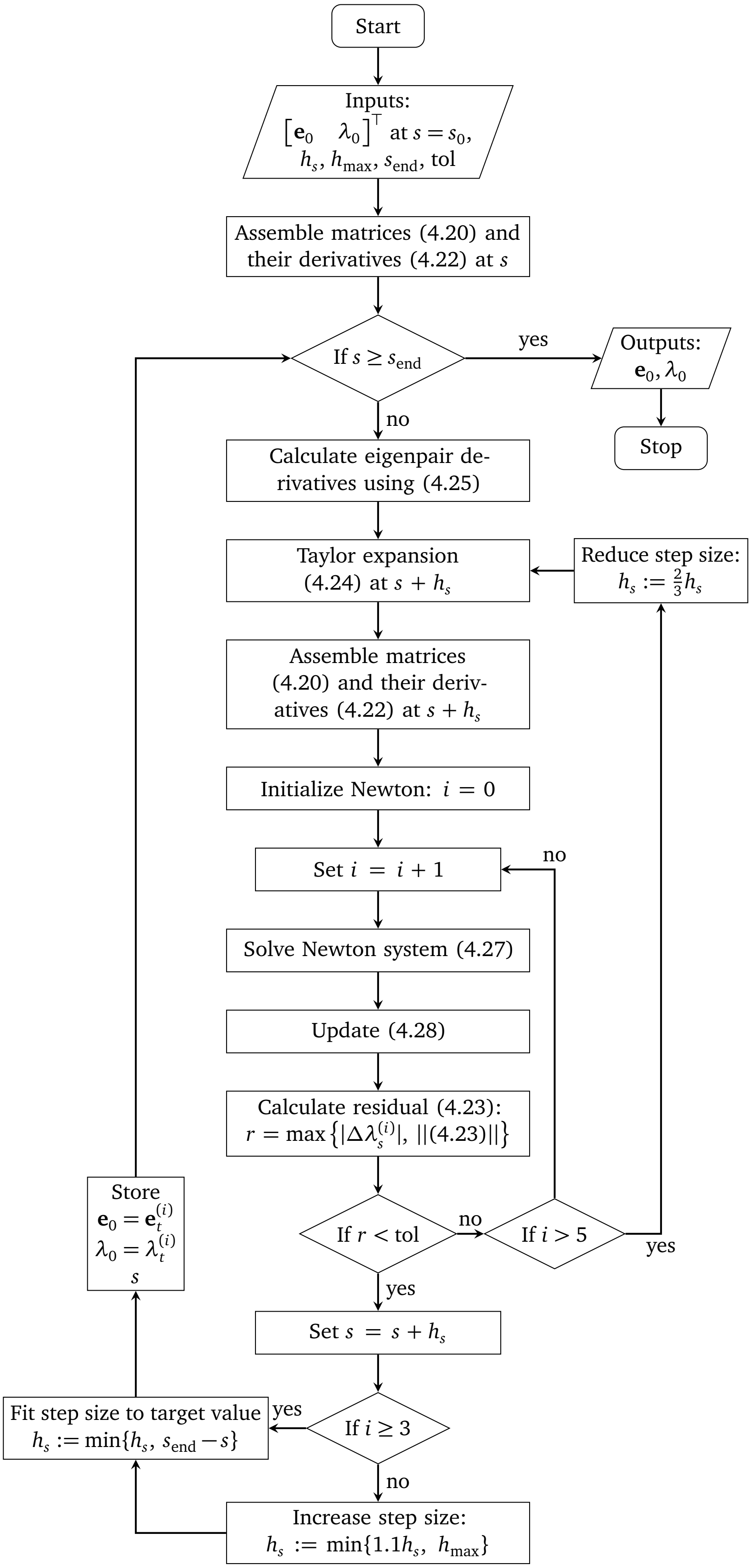

Figure 4.3: Flowchart for the proposed eigenvalue tracking method [52].

5 Substructuring Methods for RF Cavities

> *If we now want to split the domain,*
> *we should start with a bisecting plane.*
> *Some Lagrange multipliers*
> *our system requires,*
> *and a saddle-point matrix we obtain.*
>
> der

In the numerical modelling of linear accelerator structures, the simulation domain is often restricted to single RF cavities because the direct numerical treatment of the whole chain is computationally too expensive. The resource requirements in terms of both CPU time and memory occupation become even more challenging when a large number of simulations needs to be performed, as is the case for uncertainty quantification or shape optimization. Although the use of IGA in cavity simulation has been proven to be beneficial both in terms of accuracy and of overall reduction of the computational cost [33], the simulation of large and complex structures remains an overwhelming task.

A second important issue is the inclusion in the simulation of Higher Order Mode Couplers (HOMCs). Given the small features of the HOM antennas (see Fig. 5.1) and the tensor product nature of a straightforward IGA discretisation, the refinement in the beampipe area would propagate in the whole geometry, polluting the computational domain and unnecessarily increasing the dimension of the discrete problem. Other approaches have been proposed in the IGA community to allow for local refinement strategies such as hierarchical splines [95], T-splines [90], LR-splines [43] or PHT-splines [38], but, to our knowledge, as of now no stable algorithm is available for three dimensional Maxwell simulation.

In this work we propose the application of domain decomposition techniques for RF cavity simulation. In particular, we are interested in methods that allow for the coupling of different discretisations such as IGA and FEM. The goal is to be able to choose an Isogeometric scheme in the main part of the cavity, where exact geometry description plays a paramount role in the definition of the eigenfrequencies and wall deformations occur, and a FEM one in the end beampipes, where meshing is most problematic and tetrahedra allow for the inclusion of the fine details of the HOMCs.

In this chapter, we present two instances of domain decomposition methods. In particular we aim to obtain a substructuring procedure that can exploit the typical modularity of the accelerator structure to speed up matrix assembly and reduce memory consumption. Given the necessity for different grids and/or finite dimensional spaces in different sub-domains, the approximate solution might not be continuous

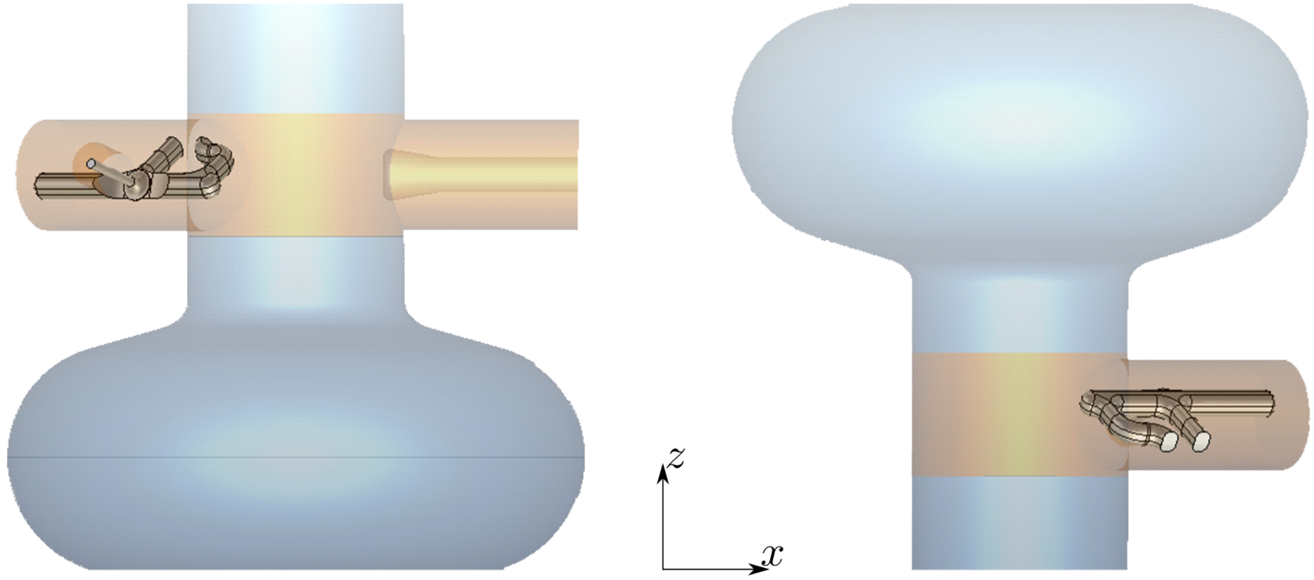

Figure 5.1: Higher Order Mode Couplers of the TESLA cavity. On the left the downstream coupler, on the right the upstream one.

across sub-domain interfaces. The coupling at the connecting circular sections needs to take into account the non-conformity of the two discretisations (see Fig. 5.2).

In the following we will consider, for the sake of exposition, a partitioning of Ω into $N_{\text{dom}} = 2$ non-overlapping sub-domains Ω_1, Ω_2 with a common interface $\Gamma = \overline{\Omega}_1 \cap \overline{\Omega}_2$ like in Figure 5.3. We will denote by Σ_1 and Σ_2 the remaining parts of the boundary, i.e. $\Sigma_s = \partial\Omega \cap \partial\Omega_s$, $s = 1, 2$.

We will also refer to Maxwell's eigenvalue problem (2.28) and its weak formulation (3.10). A Galerkin approximation like the one introduced in (3.14) cannot be used because the finite dimensional space consists of discontinuous functions across the connecting interface Γ, hence it is not a subset of $\mathbf{H}(\mathbf{curl}; \Omega)$ any more. The approach is to give a weak formulation of (2.28) compatible with the independent definition of the finite dimensional spaces on Ω_1 and Ω_2, with the addition of a weak coupling condition for the tangential fields across Γ.

In the first section of the chapter we introduce the Three-Field Method [16, 85] and in the subsequent sections we consider three substructuring approaches that can be viewed as specialisations of it. First we examine the multipatch approach introduced in section 3.6 which can be interpreted, on itself, as a domain decomposition method where all the interface degrees of freedom are strongly coupled. For modular geometries the patches can be chosen in such a way that only a reduced number of them needs to be discretised, thus speeding up matrix assembly. Each patch can be coupled with the neighbouring ones by matching the interface degrees of freedom. In the subsequent section, a Mortar method is introduced. This method allows for the coupling of different grids and exploits the inherent properties of the Isogeometric basis to naturally define the approximation space for the Lagrange multipliers. In section 5.4, we present an approach inspired by the State Space Concatenation (SSC) method recently introduced by Flisgen et al. [48, 49] which exploit the modularity of the structure and an analytical modal basis on the connecting interfaces. All of these methods are cast in the general framework of the Three-Field Method [16, 85].

5.1 The Three-Field Method

Following [85] we consider the general framework of the three-field method introduce by Brezzi and Marini [16]. Classical domain decomposition methods typically impose strongly the continuity of the solution and weakly that of the fluxes (or viceversa) leading to the so called Dirichlet-Neumann schemes.

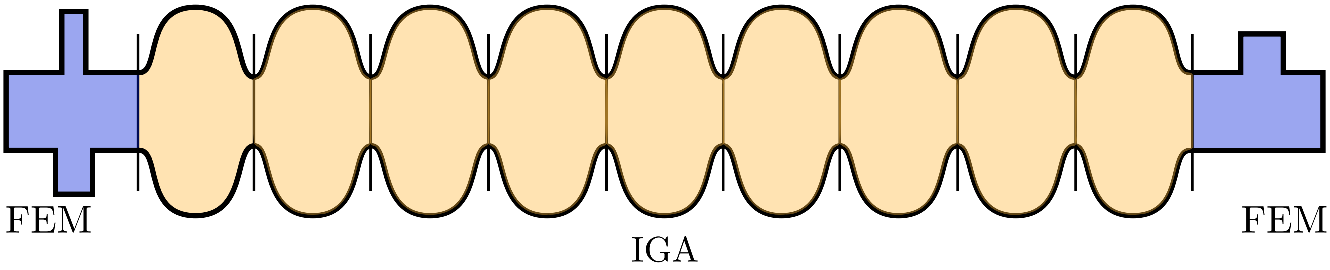

Figure 5.2: IGA-FEM approach for full cavity simulation. Each cell is discretised independently with IGA (orange colour), the two end couplers with FEM (in blue). All the pieces are coupled together through Mortar and/or State Space Concatenation methods.

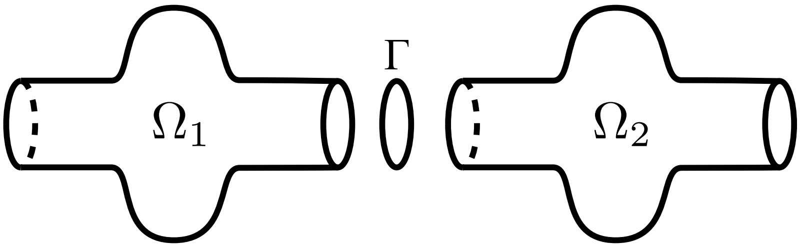

Figure 5.3: Domain decomposition into two non-overlapping sub-domains.

The three-field method relaxes both continuity conditions by introducing two sets of Lagrange multipliers instead of one. This choice allows for fully independent approximations on the two subdomains.

Given the space $V^s := \mathbf{H}(\mathbf{curl};\Omega)_{|\Omega_s}$ and the bilinear forms

$$a_s(\mathbf{u}^s,\mathbf{v}^s) = (\nabla\times\mathbf{u}^s,\nabla\times\mathbf{v}^s) - \omega^2\varepsilon_0\mu_0(\mathbf{u}^s,\mathbf{v}^s) \qquad \forall\mathbf{u}^s,\mathbf{v}^s\in V^s, \tag{5.1}$$

we introduce the following formulation: *for* $s=1,2$, *find* $\mathbf{E}^s\in V^s$, $\boldsymbol{\sigma}^s\in\Lambda'$ *and* $\boldsymbol{\lambda}\in\Lambda$ *such that*

$$\begin{aligned}
a_1(\mathbf{E}^1,\mathbf{v}^1)-\langle\boldsymbol{\sigma}^1,\mathbf{v}^1_{|\Gamma}\rangle_\Gamma &= 0 && \forall\mathbf{v}^1\in V^1 && \text{(5.2a)}\\
\langle\boldsymbol{\rho}^1,\boldsymbol{\lambda}-\mathbf{E}^1_{|\Gamma}\rangle_\Gamma &= 0 && \forall\boldsymbol{\rho}^1\in\Lambda' && \text{(5.2b)}\\
\langle\boldsymbol{\sigma}^1+\boldsymbol{\sigma}^2,\boldsymbol{\mu}\rangle_\Gamma &= 0 && \forall\boldsymbol{\mu}\in\Lambda && \text{(5.2c)}\\
\langle\boldsymbol{\rho}^2,\boldsymbol{\lambda}-\mathbf{E}^2_{|\Gamma}\rangle_\Gamma &= 0 && \forall\boldsymbol{\rho}^2\in\Lambda' && \text{(5.2d)}\\
a_2(\mathbf{E}^1,\mathbf{v}^2)-\langle\boldsymbol{\sigma}^2,\mathbf{v}^2_{|\Gamma}\rangle_\Gamma &= 0 && \forall\mathbf{v}^2\in V^2, && \text{(5.2e)}
\end{aligned}$$

where $\langle\cdot,\cdot\rangle$ denotes the duality coupling between Λ and Λ'. The Lagrange multipliers $\boldsymbol{\rho}^s$ impose the continuity of Dirichlet data on Γ, while $\boldsymbol{\sigma}^s$ correspond to Neumann data and their matching is weighted by the Lagrange multiplier $\boldsymbol{\mu}$.

The finite dimensional approximation of (5.2) requires the choice of suitable subspaces V_h^s of V^s, Ξ_h^s of Λ' and Λ_h of Λ. The discrete formulation reads: *for* $s=1,2$, *find* $\mathbf{E}_h^s\in V_h^s$, $\boldsymbol{\sigma}^s\in\Xi_h^s$ *and* $\boldsymbol{\lambda}_h\in\Lambda_h$ *such that*

$$\begin{aligned}
a_1(\mathbf{E}^1_h,\mathbf{v}^1_h)-\langle\boldsymbol{\sigma}^1_h,\mathbf{v}^1_{h|\Gamma}\rangle_\Gamma &= 0 && \forall\mathbf{v}^1_h\in V^1_h && \text{(5.3a)}\\
\langle\boldsymbol{\rho}^1_h,\boldsymbol{\lambda}_h-\mathbf{E}^1_{h|\Gamma}\rangle_\Gamma &= 0 && \forall\boldsymbol{\rho}^1_h\in\Xi^1_h && \text{(5.3b)}\\
\langle\boldsymbol{\sigma}^1_h+\boldsymbol{\sigma}^2_h,\boldsymbol{\mu}_h\rangle_\Gamma &= 0 && \forall\boldsymbol{\mu}_h\in\Lambda_h && \text{(5.3c)}\\
\langle\boldsymbol{\rho}^2_h,\boldsymbol{\lambda}_h-\mathbf{E}^2_{h|\Gamma}\rangle_\Gamma &= 0 && \forall\boldsymbol{\rho}^2_h\in\Xi^2_h && \text{(5.3d)}\\
a_2(\mathbf{E}^1_h,\mathbf{v}^2_h)-\langle\boldsymbol{\sigma}^2_h,\mathbf{v}^2_{h|\Gamma}\rangle_\Gamma &= 0 && \forall\mathbf{v}^2_h\in V^2_h. && \text{(5.3e)}
\end{aligned}$$

All the spaces in (5.3) cannot be chosen independently of each other as compatibility conditions are necessary to ensure well posedness and stability of the problem (see [85, chapter 2.5.2]).

In the following sections we present three instances of domain decomposition methods that can be derived from the three-field method.

5.2 Multipatch

Let us consider the multipatch approach presented in section 3.6. As mentioned before, in IGA, multipatch is usually applied to treat complicated geometry that can not be represented by a single smooth mapping of the unit cube. The idea is to discretise all the patches conformingly, i.e. in such a way that the knot vectors and control points match at the common interfaces and to suitably identify the degrees of freedom using conditions (3.50).

We define the local stiffness and mass matrices

$$\mathbf{K}_s = \{k_{ij}^s\} = \left(\nabla \times \mathbf{v}_j, \nabla \times \mathbf{v}_i\right)_{\Omega_s} \qquad \mathbf{M}^s = \{m_{ij}^s\} = \varepsilon_0\mu_0\left(\mathbf{v}_j, \mathbf{v}_i\right)_{\Omega_s} \qquad s = 1,2, \quad i,j = 1,\dots,N_s, \tag{5.4}$$

with N_s the number of degrees of freedom in subdomain s.

The coupled system for the full domain can be written as

$$\begin{bmatrix} \mathbf{K}_1 & 0 & \mathbf{B}_1 \\ 0 & \mathbf{K}_2 & -\mathbf{B}_2 \\ \mathbf{B}_1^\top & -\mathbf{B}_2^\top & 0 \end{bmatrix} \begin{bmatrix} \mathbf{e}_1 \\ \mathbf{e}_2 \\ \mathbf{l} \end{bmatrix} = \omega^2 \begin{bmatrix} \mathbf{M}_1 & 0 & 0 \\ 0 & \mathbf{M}_2 & 0 \\ 0 & 0 & 0 \end{bmatrix}, \tag{5.5}$$

where the vectors $\mathbf{e}_s$ collect the degrees of freedom for the electric field in the s-th domain, $\mathbf{l}$ are Lagrange multipliers, and $\mathbf{B}_s$ are coupling matrices. Since the degrees of freedom on the interface Γ are exactly matched, the matrices $\mathbf{B}_s$ are simply diagonal matrices that couple the degrees of freedom corresponding to the tangential components of the electric field from both sides. Thus, some unknown can be eliminated from the system by static condensation. In practice, this is enforced by numbering the basis functions in such a way that matching functions have the same index and by mapping the local indices on each patch to a global index of the multipatch domain (see [94, section 5] for more details).

The multipatch approach can be interpreted as an extreme case of the three-field method in which the coupling is performed strongly and conditions (5.3c), (5.3d) and (5.3e) vanish completely. The drawback of the multipatch method is that the discretisation of each patch can not be performed independently and a compatible discretisation has to be chosen in each subdomain. Furthermore, if we consider the issue of the non-locality of the refinement due to the tensor product nature of IGA, the matching grids on the common interface implies that any refinement performed on one patch also pollutes the neighbouring ones.

In the remainder of the chapter we consider methods that exploit weak coupling to guarantee more freedom in the discretisation choices on each subdomain.

5.3 Mortar Method

For the introduction to the Mortar method we will follow [85]. Given an IGA discretisation of the type introduced in section 3.4 in each of the two parts, i.e. the sudomain Ω_s is the mapping of the unit cube in the physical space through a NURBS mapping $\mathbf{F}_s : \hat{\Omega} \mapsto \Omega_s$ and a curl-conforming finite dimensional space for the approximation is given:

$$V_h^s \equiv \left\{\mathbf{v}_h^s \in \mathbf{H}\left(\mathbf{curl}; \Omega_s\right) \mid \mathbf{v}_h^s = \hat{\mathbf{v}} \circ (\iota_1^s)^{-1}, \hat{\mathbf{v}} \in S^1\left(\hat{\Omega}\right)\right\}, \tag{5.6}$$

where ι_1^s identifies the curl preserving pull-back function (3.26c) given the parametrisation $\mathbf{F}_s$ and S^1 is the space defined in (3.34).

$$V_h^s := V_{h|\Omega_s} \tag{5.7}$$

correspond to the restriction of V_h in (3.38) to Ω_s.

The main idea of the Mortar method is to introduce a discrete space V_δ that approximates $\mathbf{H}_0(\mathbf{curl};\Omega)$ without being contained into $C^0(\overline{\Omega})$. More precisely:

$$V_\delta := \left\{\mathbf{v}_\delta \in \mathbf{L}^2(\Omega) \,|\, \mathbf{v}_\delta^s = v_{\delta|\Omega_s} \in V_h^s, \, \mathbf{v}_\delta^s \times \mathbf{n}_{|\Sigma_s} = 0\right\}. \tag{5.8}$$

To provide an accurate solution of the original problem (2.28), the solution is sought in a well suited subspace V_δ^c of V_δ that also ensures the matching of the tangential components of the electric field across the interface Γ. Given that forcing the continuity in a strong sense is, in general, too strict when dealing with non matching grids, the Mortar methods imposes weak continuity using Lagrange multipliers. In particular, introducing V_δ^1 and V_δ^2, the restrictions of V_δ to Ω_1 and Ω_2 respectively and the functions $\mathbf{E}_\delta^1 \in V_\delta^1$ and $\mathbf{E}_\delta^2 \in V_\delta^2$, the restriction of $\mathbf{E}_\delta \in V_\delta$ to Ω_1 and Ω_2, the following integral coupling condition should be satisfied:

$$\left(\left(\mathbf{E}_\delta^1 \times \mathbf{n}_1 - \mathbf{E}_\delta^2 \times \mathbf{n}_2\right)_\Gamma, \boldsymbol{\mu}_\delta^s\right) = 0 \qquad \forall \boldsymbol{\mu}_\delta^s \in \Lambda_\delta^s, \tag{5.9}$$

with $\mathbf{n}_i$ the outward unit vector to subdomain i. Here, Λ_δ^s denotes the space of Lagrange multipliers and correspond to the restriction to Γ of the functions of V_δ^s. Depending on s, each domain can be *master* or *slave*: by taking $s = 2$ in (5.9), Ω_1 plays as master, that is (5.9) corresponds to generating the value of $\mathbf{E}_{\delta|\Gamma}^2$ from $\mathbf{E}_{\delta|\Gamma}^1$. The opposite choice is obviously possible.

The discrete problem to be solved becomes: *Find* $\omega_\delta \in \mathbb{R}$ *and* $\mathbf{E}_\delta \in V_\delta^c$ *such that*

$$\sum_{s=1}^{2}\left((\nabla \times \mathbf{E}_\delta, \nabla \times \mathbf{v}_\delta) - \omega_\delta^2 \varepsilon_0 \mu_0 (\mathbf{E}_\delta, \mathbf{v}_\delta)\right) = 0 \qquad \forall \mathbf{v}_\delta \in V_\delta^c, \tag{5.10}$$

where V_δ^c is defined as

$$V_\delta^c := \left\{\mathbf{v}_\delta \in V_\delta \,|\, \left(\left(\mathbf{v}_\delta^1 \times \mathbf{n}_1 - \mathbf{v}_\delta^2 \times \mathbf{n}_2\right)_\Gamma, \boldsymbol{\mu}_\delta^s\right) = 0, \, \forall \boldsymbol{\mu}_\delta^s \in \Lambda_\delta^s\right\}. \tag{5.11}$$

For the case where $N_{\mathrm{dom}} > 2$, the procedure is analogous.

Some more details on Mortaring techniques and about the analysis of the approximation properties of the Mortar FEM spaces can be found, for example, in [8, 13, 22]. In the following, we will focus on the differences that arises when dealing with IGA and, in particular, B-Spline spaces.

5.3.1 Isogeometric Mortar Method

Let us set, without loss of generality, Ω_1 to be the master side and the Lagrange multipliers space to be Λ_δ^2. We will drop the index 2 and just write Λ_δ and $\boldsymbol{\mu}_\delta$. Λ_δ needs to properly discretise the trace space of $V_h^2 \subset \mathbf{H}(\mathbf{curl};\Omega_s)$. In particular, being the trace space of $\mathbf{H}(\mathbf{curl};\Omega_s)$ on Γ, it can be proven that Λ_δ is a divergence conforming space, subset of $H^{-1/2}(\mathrm{div}_\Gamma;\Gamma)$. For a review of the properties of trace spaces of $\mathbf{H}(\mathbf{curl};\Omega)$ we refer the interested reader to [18, 21].

In a classical FEM framework the proper discretisation of the trace space is not straightforward. It typically requires the use of Raviart-Thomas type elements and a baricentric refinement of the boundary mesh to define the dual space [17]. However, as presented in chapter 3, in an IGA setting the definition of such spaces usually reverts to properly change the degree of the discretisation for each component of the vector field and applying the proper pull-back function (see (3.26)).

Let us then consider space V_h^s defined in (5.6). Let us also suppose that $\Gamma = \mathbf{F}_s(\hat{\Gamma})$ and that, without loss of generality, $\hat{\Gamma}$ is the unit square on the reference space corresponding to $\xi_3 = 0$. Then we define the space

$$S^2(\hat{\Gamma}) := S_{\boldsymbol{\alpha}_1-1,\boldsymbol{\alpha}_2-2}^{p_1-1,p_2-2}\left(\hat{\Gamma}\right) \times S_{\boldsymbol{\alpha}_1-2,\boldsymbol{\alpha}_2-1}^{p_1-2,p_2-1}\left(\hat{\Gamma}\right). \tag{5.12}$$

The Lagrange multiplier space on Γ can be obtained as

$$\Lambda_\delta = \left\{ \mathbf{v} = \hat{\mathbf{v}} \circ \iota_2^{-1} \,|\, \hat{\mathbf{v}} \in S^2(\hat{\Gamma}) \right\}, \tag{5.13}$$

with ι_2 the divergence preserving transformation in (3.26d). It should be clear that, given the three dimensional vector space $S^1(\Omega)$, it is fairly simple to extract the proper components and to construct Λ_δ, which makes the implementation of a Mortar scheme in the IGA setting appealing. When dealing with an IGA-FEM coupling, it is then desirable to choose s in such a way that Λ_δ is the trace space of the IGA space and not the FEM one.

5.3.2 Saddle-Point Formulation and inf-sup Condition

We introduce the bilinear forms:

$$a(\mathbf{u}, \mathbf{v}) = \sum_{s=1}^{2} \left((\nabla \times \mathbf{u}^s, \nabla \times \mathbf{v}^s) - \omega^2 \varepsilon_0 \mu_0 (\mathbf{u}^s, \mathbf{v}^s) \right) \qquad \forall \mathbf{u}, \mathbf{v} \in V_\delta \tag{5.14}$$

$$b(\mathbf{u}, \boldsymbol{\mu}) = \left((\mathbf{u}^1 \times \mathbf{n}_1 - \mathbf{u}^2 \times \mathbf{n}_2)_\Gamma, \boldsymbol{\mu} \right) \qquad \forall \mathbf{u}^s \in V_\delta,\ \boldsymbol{\mu} \in \Lambda_\delta, \tag{5.15}$$

to write problem (5.10)-(5.11) as: *Find* $\omega_\delta \in \mathbb{R}$ *and* $(\mathbf{E}_\delta, \lambda_\delta) \in V_\delta \times \Lambda_\delta$ *such that*

$$a(\mathbf{E}_\delta, \mathbf{v}_\delta) + b(\mathbf{E}_\delta, \boldsymbol{\lambda}_\delta) = 0 \qquad \forall \mathbf{v}_\delta \in V_\delta \tag{5.16a}$$

$$b\left(\mathbf{E}_\delta, \boldsymbol{\mu}_\delta\right) = 0 \qquad \forall \boldsymbol{\mu}_\delta \in \Lambda_\delta. \tag{5.16b}$$

Given a basis $\left\{\mathbf{v}_j\right\}_{j=1}^{N_s}$ for V_h^s and a basis $\{\boldsymbol{\lambda}_k\}_{k=1}^{N_\Lambda}$ for the Lagrange multiplier space, we can write the local stiffness and mass matrices as in (5.4), while the coupling matrices become

$$\mathbf{B}_s = \{b_{ik}^s\} = b(\boldsymbol{\lambda}_k, \mathbf{v}_i) \qquad s = 1, 2, \quad i = 1, \ldots, N^s, \quad k = 1, \ldots, N_\Lambda. \tag{5.17}$$

Problem (5.16) can be written in algebraic form in an analogous way to the multipatch case to get a generalised eigenvalue problem of the type (5.5). In this instance, however, the coupling matrices $\mathbf{B}_s$ are not diagonal and do not allow for the static condensation procedure performed before. The final system is then of the form

$$\begin{bmatrix} \mathbf{K} & \mathbf{B} \\ \mathbf{B}^\top & 0 \end{bmatrix} \begin{bmatrix} \mathbf{e} \\ \mathbf{l} \end{bmatrix} = \omega^2 \begin{bmatrix} \mathbf{M} \\ 0 \end{bmatrix}, \tag{5.18}$$

with the block diagonal matrices

$$\mathbf{K} = \begin{bmatrix} \mathbf{K}_1 & 0 \\ 0 & \mathbf{K}_2 \end{bmatrix} \qquad \mathbf{M} = \begin{bmatrix} \mathbf{M}_1 & 0 \\ 0 & \mathbf{M}_2 \end{bmatrix}$$

and the coupling matrix $\mathbf{B} = \begin{bmatrix} \mathbf{B}_1 & -\mathbf{B}_2 \end{bmatrix}^\top$. The discrete solution is reconstructed as

$$\mathbf{E} = \sum_{s=1}^{2} \sum_{j=1}^{N^s} e_j^s \mathbf{v}_j. \tag{5.19}$$

System (5.18) is a so called *saddle-point* problem. It is well known from the theory of mixed formulations that saddle-point problems give rise to questions about well posedness and stability [9, 15]. In particular, the convergence properties of such problems are governed by the verification of the Ladyzhenskaya-Brezzi-Babuška inf-sup stability condition [15]:

$$\inf_{\mu\in\Lambda_\delta}\sup_{\mathbf{u}\in V_\delta}\frac{b(\mathbf{u},\boldsymbol{\mu})}{\|u\|_{V_\delta}\,\|\mu\|_{\Lambda_\delta}}\geq\beta_{\text{inf}}>0. \tag{5.20}$$

A practical interpretation of criterion (5.20) is that the space of Lagrange multipliers should not be too rich with respect to V_δ. When that is not the case, the left hand side matrix in (5.18) becomes singular and spurious solutions appear.

The analysis of such condition is, in general, a difficult one. A full article on the inf-sup stability of the proposed discretisation scheme is under preparation [26]. In particular it is possible to prove that the method becomes unstable when the discretisation degree for the Lagrange multiplier space is $p_\Gamma = p_{\text{IGA}} - k$, with p_{IGA} the degree of the IGA space and k even.

In the present work, we apply numerical verification of the inf-sup condition using the method proposed in [30]. In particular, the β_{inf} constant in (5.20) can be estimated by solving the generalised eigenvalue problem

$$\mathbf{B}^\top\mathbf{K}^{-1}\mathbf{B}\mathbf{x}=\lambda^2\mathbf{M}_\Gamma\mathbf{x} \qquad \text{with } \mathbf{M}_\Gamma=\{m_{\Gamma,ml}\}=\int_\Gamma\boldsymbol{\lambda}_l\boldsymbol{\lambda}_m ds. \tag{5.21}$$

Given the eigenvalues λ_k, solution of problem (5.21), the inf-sup constant is given by

$$\beta_{\text{inf}}=\min_k\lambda_k. \tag{5.22}$$

Although solving (5.21) is clearly not efficient, since it involves the computation of $\mathbf{K}^{-1}$, we use this test to verify the well posedness of the formulation introduced.

As a final remark, we highlight once again the relation of the Mortar method with the three-field framework introduced above: in a Mortar approach, one chooses, e.g., Λ_h in (5.3d) to be $\Lambda_h=\text{tr}(V_h^1)$. This simplifies (5.3) since $\Xi_h^1=\emptyset$, thus (5.3c) disappears, and $\Xi_h^2=\text{tr}(V_h^2)$.

The Mortar method has the advantage, with respect to the multipatch case, to allow for different discretisation schemes on different subdomains, at the expense of having to explicitly compute the coupling matrix $\mathbf{B}$ and of solving a saddle-point problem. Furthermore, the computation of matrices $\mathbf{B}_s$ typically requires the construction of the intersecting mesh on the common interface Γ. This is straightforward when two IGA discretisations are used on both sides, but can become quite cumbersome, in particular if the coupling is between a hexahedral mesh, like in IGA, and a tetrahedral mesh, like in classical FEM.

5.4 State-Space Concatenation

This section discusses the SSC method recently introduced by Flisgen et al. [48] and its properties with respect to standard Domain Decomposition Methods (DDMs).

In the SSC method, the typical linear accelerator structure is exploited for the decomposition. The geometry is decomposed into smaller sub-domains in correspondence of waveguide like section, e.g. between each cavity, so that physical knowledge about the waveguide dispersion relation may be taken advantage of.

The undampened modes in the waveguide are excited in each part using a superposition of waveguide modes on the interface Γ. These modes are given by the eigenfunctions of a two-dimensional Laplace operator. The model for the complete system is then recovered by treating each sub-domain as a dynamical system with given Input/Output characteristics and by coupling the I/O *ports* of neighbouring cells. Outside excitations can be treated in the same way by imposing waveguide ports on the corresponding boundaries.

In addition to this coupling strategy, the SSC method also implements Reduced Order Models (ROMs) to scale down the size of the problem for each piece of the structure. Similar methods have been proposed in literature for different kinds of application such as mechanics [46] or fluid dynamics [59] where, instead of the waveguide modes, the general concept of port reduction is used. For the purposes of this thesis, we are interested in the SSC method as a substructuring method where the typical structure of LINAC cavities is exploited for the selection and computation of the Lagrange multipliers on the coupling interfaces.

5.4.1 Input/Output System

Let us consider, Maxwell's eigenvalue problem (2.28) in a cavity of domain Ω. On each sub-domain, we denote by $\mathbf{E}^s$ the restriction of the solution $\mathbf{E}$ on Ω_s, i.e. $\mathbf{E}^s = \mathbf{E}|_{\Omega_s}$, and we write the following problem:

$$\begin{aligned} \nabla \times \nabla \times \mathbf{E}^s &= \omega^2 \varepsilon_0 \mu_0 \mathbf{E}^s && \text{in } \Omega_s \\ \mathbf{E}^s \times \mathbf{n} &= 0 && \text{on } \Sigma_s \\ (\nabla \times \mathbf{E}^s) \times \mathbf{n} &= \mathbf{\Phi} && \text{on } \Gamma \end{aligned} \tag{5.23}$$

where $\mathbf{\Phi}$ is expressed as a superposition of waveguide modes φ_k on Γ, like the ones introduced in section 2.1.2:

$$\mathbf{\Phi} = \sum_k \alpha_k \varphi_k. \tag{5.24}$$

The modes φ_k are determined by the cross section of the cut plane Γ and correspond to the eigenfunctions of the transverse Laplace operator. In [48], the series (5.24) is truncated by selecting the first $N_\Gamma < \infty$ modes. The choice of N_Γ is motivated by the physics of the problem. In particular, all the waveguide modes which can propagate in the frequency range of interest should be part of the modal basis. Furthermore, it is suggested that a certain amount of evanescent modes should be added: the shorter the waveguide-like structure across Γ is, the more modes are needed for an accurate solution.

Given the space V_h^s in (5.6), we introduce the space

$$V_{h,0}^s = \left\{ \mathbf{v} \in V_h^s \,|\, \nabla \times \mathbf{v}_{|\Sigma_s} = 0 \right\} \qquad s = 1, 2. \tag{5.25}$$

On each sub-domain, we can write the weak formulation of (5.23) as: *Find* $\mathbf{E}^s \in V_{h,0}^s$ *such that*

$$(\nabla \times \mathbf{E}^s, \nabla \times \mathbf{v}) - (\mathbf{\Phi}, (\mathbf{n} \times \mathbf{v}) \times \mathbf{n})_\Gamma = \omega^2 \varepsilon_0 \mu_0 (\mathbf{E}^s, \mathbf{v}) \qquad \forall \mathbf{v} \in V_{h,0}^s. \tag{5.26}$$

Similarly to the Mortar method, this problem needs a further condition to ensure the continuity of the global solution $\mathbf{E}$ across Γ. The continuity is once again enforced in a weak sense, but the Lagrange multipliers are chosen to be the waveguide modes φ_k themselves:

$$\left((\mathbf{n} \times \mathbf{E}^1) \times \mathbf{n}, \varphi_k \right)_\Gamma = \left((\mathbf{n} \times \mathbf{E}^2) \times \mathbf{n}, \varphi_k \right)_\Gamma \qquad \forall k = 1 \ldots N_\Gamma. \tag{5.27}$$

This continuity condition allows for jumps in the normal component of the field which, in turn, might cause non-physical charges to appear on the interface Γ. Spurious modes of this type can be eliminated from the spectrum in a post processing step by imposing the divergence free condition (2.4b) as proposed, e.g, in [98].

It is easy to see that the discretisation of problem (5.26)-(5.27) gives rise once again to a saddle-point system analogous to (5.18), where the coupling matrices will be given by

$$\mathbf{B} = \begin{bmatrix} \mathbf{B}_1 \\ -\mathbf{B}_2 \end{bmatrix} \quad \text{with } \mathbf{B}_s = \{b_{ik}^s\} = \left(\varphi_k, \left(\mathbf{n} \times \mathbf{v}_i^s \right) \times \mathbf{n} \right)_\Gamma \quad s = 1, 2,\ i = 1, \ldots, N^s,\ k = 1, \ldots, N_\Gamma \tag{5.28}$$

It is worth noticing, that, with respect to the Mortar method, the SSC has the advantage that the computation of the coupling matrices is completely independent on each side since the Lagrange multipliers φ_k live on a separate space. When dealing with the coupling of non-conforming meshes across Γ, the Mortar method requires the construction of a common mesh given by the intersection of the meshes on the two sides. In the SSC case, however, matrices $\mathbf{B}_1$ and $\mathbf{B}_2$ can be straightforwardly computed on completely different meshes. Furthermore, for accelerator cavities with common shapes, the intersection surface Γ is usually sufficiently simple that the analytical eigenmodes can be used.

The refinement of the subdomains and the choice of the number of coupling modes N_Γ is governed by the inf-sup stability condition. It is our interest to link the dimension of the set spanned by the modal basis $\{\varphi_k\}$ to the stability of the coupled system. In absence of a rigorous proof, inf-sup test (5.21) can be used to verify whether the coupled system is stable. The results of such a test is presented in chapter 8.

In a similar way to the previous methods presented, the SSC method can be interpreted as a three-field method too. Here the space Λ_h is assigned as the space spanned by the waveguide modes, and Ξ_h^1, Ξ_h^2 are bot set to be equal to Λ_h. It is interesting to notice that in this case there is no master/slave relation but the formulation is perfectly symmetric.

5.5 Summary

The possibility to exploit cavity modularity for the matrices construction and the necessity of applying different discretisation approaches on different parts of the device has lead to the introduction of two substructuring methods based on domain decomposition techniques. Both methods can be cast in the common framework of the three-field method and lead to the solution of a saddle-point problem which requires the verification of an inf-sup condition to ensure stability. A numerical test to verify this property can be applied.

In the second part of the thesis, the methods introduced are applied to the simulation of particle accelerator cavities.

Part II

Applications

6 Cavity Simulation and Lorentz Detuning

Now I'll talk about Lorentz detuning,
you know all the theory, I'm assuming.
But before I proceed,
there is something I need:
the field flatness demands some improving.

The numerical discretisation scheme introduced in chapter 3 is implemented using GeoPDEs [94], an Octave/Matlab package for the solution of PDEs with IGA. Together with the nurbs package [77], this code allows for the definition of NURBS geometries and the construction of the IGA spaces and the corresponding matrices.

Two standard solvers for generalised eigenvalue problems are tested: the Implicitly Restarted Lanczos Method (IRLM) implemented in the ARPACK library [65] and the Jacobi-Davidson method JDQZ developed by Gerard Sleijpen and Henk van der Vorst [50]. The two methods perform similarly in terms of memory consumption and, while the IRLM implementation is more efficient, the Jacobi-Davidson solver shows better accuracy even with very ill conditioned matrices. Unless otherwise specified, the results shown in the following of the thesis are obtained with the JDQZ algorithm. Since the eigenfunctions of Maxwell's eigenvalue problem (2.28) are defined up to a constant, all the computed fields will be rescaled in such a way that the total stored energy in the cavity is equal to 1 J which is a common choice in cavity simulation [35].

In this chapter we first present the pill-box cavity case as a verification example: the convergence of the eigenvalues to the exact solution is shown and the efficiency of the eigenvalue solver when applied to matrices arising from an IGA discretisation and a FEM one is compared. Furthermore, we present the results for the Lorentz detuning simulation both for the pill-box cavity, where a closed form solution is available, and for the single-cell TESLA cavity. Some further comparison with the state of the art FEM solver Computer Simulation Technology (CST$^{®}$) is also shown. In section 6.3 we present the numerical tuning process for the 9-cell TESLA cavity and the frequency shift caused by the Lorentz detuning effect computed in this configuration. In the last section, as a final example, the optimisation of a β-graded cavity for the Superconducting-DArmstadt-LINear-ACcelerator (S-DALINAC) is presented.

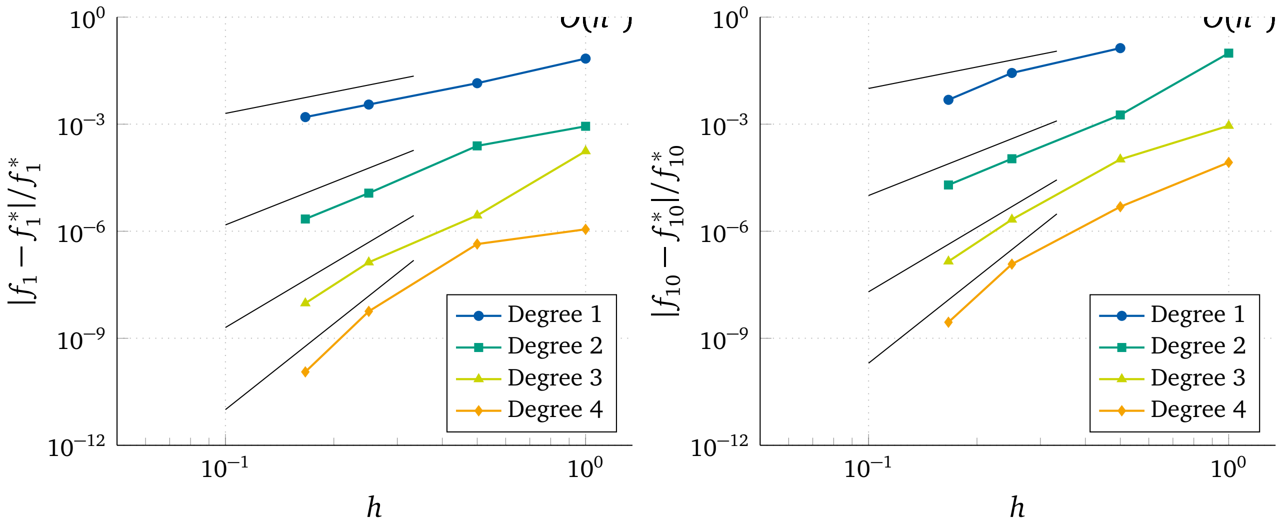

(a) First computed eigenfrequency (TM_{010}).

(b) Tenth computed eigenfrequency (TM_{110}).

Figure 6.1: Convergence of the eigenfrequencies in the pill-box cavity to the exact value for different discretisation orders and increasing mesh resolution. In black the expected rates of convergence.

6.1 Eigenvalue Problem in a Pill-Box Cavity

As a verification example, the discretisation scheme introduced in chapter 3 is applied to the case of a pill-box cavity of radius $R = 35$mm and length $L = 100$mm. The closed form solution for the fundamental mode is given in (2.33) - (2.34). Figure 6.1a depicts the relative error between the first computed eigenfrequency f_1 and the exact solution f_1^*. The expected order of convergence for the eigenvalues is $O(h^{2p})$ where p is the degree of the basis functions and h is the mesh size [11]. The asymptotic convergence rates for increasing order of IGA discretisation, which can be appreciated in the logarithmic scale, correspond to what predicted by the theory. In Fig. 6.1b the analogous graph for the tenth computed eigenvalue is presented: the order of convergence is preserved although, not surprisingly, the relative error is approximately one order of magnitude bigger since the eigenvalue is higher in the spectrum.

In addition to the convergence rates for increasing order of IGA discretisation, we are interested in investigating the efficiency of the solver. The wider support of IGA basis functions with respect to the classical FEM ones, leads to stiffness and mass matrices with bigger bandwidth and, typically, with worse conditioning. However, as mentioned in chapter 3, the number of IGA degrees of freedom required to achieve a given accuracy is smaller which, in turn, leads to a trade off in efficiency.

Given the same cylindrical geometry, a set of IGA matrices are computed, using GeoPDEs, for IGA basis functions of degree 2 and 3 and for increasing mesh refinement. Analogous FEM matrices are built using the proprietary electromagnetic field simulation software CST® [35] and, in particular, CST MICROWAVE STUDIO (CST MWS®) which is well renowned for cavity simulation. We test the standard Lanczos-Arnoldi solver for the generalized eigenvalue problem both with the IGA matrices and with the FEM ones. In Table 6.1 we report the number of degrees of freedom required by the IGA and FEM methods to achieve a given level of accuracy, alongside with the time needed to solve the corresponding eigenvalue problem. Given the wider support, the IGA matrices are denser than their FEM counterparts. For example, given an Isogeometric matrix of dimension 50 000 and degree 2 approximately, the ratio of non zero elements over total number of elements is 2.4×10^{-2}, while for an analogous FEM matrix the ratio is 8.8×10^{-4}. However the accuracy-per-degree-of-freedom is higher when using Isogeometric Analysis and this leads to speed-ups up to 9 times (2nd order, error 1×10^{-8}) as shown in Table 6.1.

	2^{nd} order				3^{rd} order			
	IGA		FEM		IGA		FEM	
Rel. Error	N_{dof}	$t\,[\text{s}]$	N_{dof}	$t\,[\text{s}]$	N_{dof}	$t\,[\text{s}]$	N_{dof}	$t\,[\text{s}]$
1×10^{-5}	1540	0.2	5346	1.7	-	-	-	-
1×10^{-6}	9828	6.8	46 266	21.1	-	-	-	-
1×10^{-7}	18 304	14.8	158 050	187.6	-	-	-	-
1×10^{-8}	47 520	95.1	381 036	843.4	4480	2.5	15 618	5.8
1×10^{-10}	-	-	-	-	30 628	91.7	135 246	141.5
1×10^{-11}	-	-	-	-	97 888	542.8	461 937	1176.3

Table 6.1: Number of DoFs required to compute the first accelerating mode in the pill-box cavity within a prescribed accuracy ($R = 35\text{mm}$ and $L = 100\text{mm}$, $f_0 = 3.2783579381\text{GHz}$). The IGA implementation is carried out in GeoPDEs [94] while for the FEM simuation CST STUDIO SUITE [35] is used (empty cells are due to unavailable FEM matrices). The times listed refer to the solution of the eigenvalue problem with ARPACK.

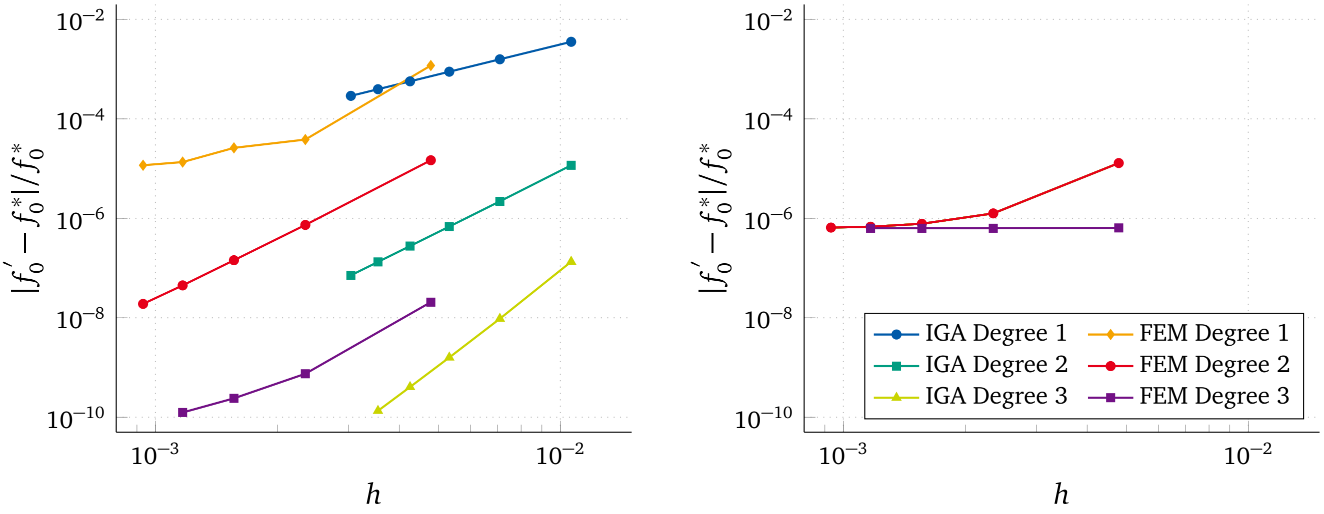

(a) Comparison of IGA proposed method and CST® implementation with sensitivity analysis.

(b) Convergence of CST® results for the resonant frequency with the algorithm proposed in section 2.5.

Figure 6.2: Convergence of the eigenfrequency for the deformed pill-box cavity (design parameters: $R = 35$ mm, $L = 100$ mm, exact frequency $f_0^* = 3.278292919\text{GHz}$). The IGA simulation is performed following the steps described in section 2.5. The FEM results are obtained using the commercial software CST®.

6.1.1 Lorentz Detuning

A second verification example is the simulation of the Lorentz detuning effect on the pill-box cavity. The steps illustrated in section 2.5 are applied to the first transverse magnetic TM_{010} mode in the cavity (the accelerating mode) and the corresponding detuning is computed. By excluding the bases of the cylinder in the mechanical simulation, the resulting deformation is only radial and the frequency shift can be computed analytically using once again formula (2.34) with the new value of the radius. The shifted frequency is compared with the exact solution given by the theory while increasing the mesh resolution for a given polynomial order (see Fig. 6.2a). Of particular relevance is the fact that neither the electromagnetic-mechanical coupling nor the geometry deformation through the control points movement appears to have any detrimental effects on the optimal convergence rates for the eigenvalue problem.

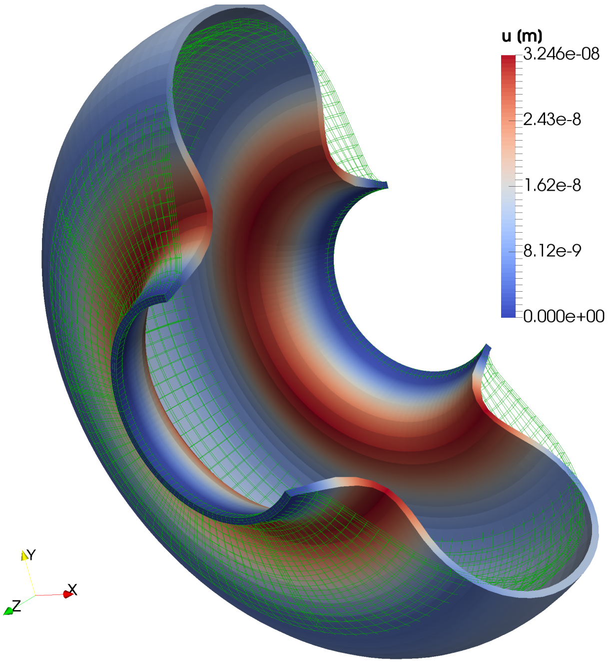

Figure 6.3: Wall deformation in the 1-cell TESLA cavity due to the Lorentz forces (in green the starting geometry outline). The displacement has been enhanced of a factor 500 000.

Ref. Lev.	N_{el}	N_{dof}	f_0 [GHz]	Shift [Hz]	Variation [Hz]
1	30	872	1.314 575 516	137.64	-
2	240	2760	1.301 894 514	188.25	50.61
3	810	6336	1.301 124 581	193.14	4.89
4	1920	12 140	1.301 005 564	189.87	3.27
5	3750	20 712	1.300 975 853	187.01	2.86
6	6480	32 592	1.300 965 893	184.96	2.05
7	10 290	48 320	1.300 961 916	183.56	1.40
8	15 360	68 436	1.300 960 116	182.59	0.96

Table 6.2: Detuning values for the 1-cell TESLA cavity. The number of elements N_{el} and the number of degrees of freedom N_{dof} refer to the values for Maxwell's eigenproblem.

As a comparison, we perform the same kind of computation using CST®. The FEM eigenvalue solver computes the eigenmode and the Lorentz forces which are exported to CST MPHYSICS STUDIO (CST MPS®) to compute the wall deformation. The information on the displacement is then imported in CST MWS®, where the detuned frequency $f_0^{'}$ is calculated through a sensitivity analysis approach. The results are depicted in Fig. 6.2a along with the IGA ones. The approach used in CST® leads to a linearisation of the problem but the method performs well since the deformations are very small. It is also worth noticing, once again, that, given a fixed number of degrees of freedom, the IGA discretisation presents a higher accuracy with respect to FEM, particularly for higher order.

In addition to the simulation using sensitivity analysis, the proposed algorithm for IGA is implemented and tested in CST®. The results show that the level of accuracy reachable in this case for the resonating frequency is limited to 10^{-6} (see Figure 6.2b).

6.2 1-cell TESLA Cavity

A more realistic example is the 1-cell TESLA cavity [2] (see Fig. 2.8). The accelerating eigenmode of the TESLA cavity is once again the TM_{010} mode at 1.3GHz. The frequencies for undeformed and deformed geometry are computed on six meshes with an increasing number of subdivisions (Table 6.2). In the last column of Table 6.2 we report the difference between the values of the frequency shift computed at two subsequent levels of refinement, which shows the convergence of the method and that approximately 70 000 DOFs, are sufficient to achieve an accuracy of about 1 Hz. In this last case, the total computational time (geometry creation, matrix construction, two eigenvalue solutions and the linear elasticity problem in between) is approximately 10 min. In Fig. 6.3, the undeformed and deformed geometry are compared. The computed displacement is in the nm range, which is in good accordance to results reported in literature [2].

6.3 9-cell TESLA Cavity

The 9-cell TESLA cavity is constructed with the nurbs toolbox in Octave/Matlab [77] using the TTF design parameters of Table 2.1. In operation, the beampipes that connect each cavity are 141.6 mm in length, with couplers connected to it to avoid the trapping of HOMs in the cavity (see Fig. 5.1). As mentioned in the previous part of the thesis, the simulation of the cavity with the couplers is unaffordable with a classical IGA approach due to the impossibility of local refinement strategies. As a first step simple cylindrical beampipes with no couplers are added at the cavity irises, with a longer longitudinal length of 365 mm (see Fig. 6.4). This is a common choice in cavity simulation that aims at rendering negligible the effects of the boundary conditions at the end caps of the beampipes on the eigenmodes [97].

In Table 6.3 the first 60 eigenmodes are listed. The results are obtained using second degree B-Spline basis functions and approximately 200 000 degrees of freedom. The first nine modes correspond to the first passband of TM_{010} modes and are well separated from the higher ones. The last mode in the passband is the π-mode and is the one used for acceleration (highlighted in grey in the table). HOMs are more difficult to categorise since the different monopole, dipole and quadrupole modes start overlapping. A detailed analysis of the different types of modes is not the scope of this work; the interested reader can find more information in, e.g., [97].

As expected the direct computation of the eigenfrequency and of the electric field distribution in the TESLA cavity, using the TTF design parameters, shows that the cavity needs a tuning process. The frequency is approximately a MHz off the nominal value and the field is concentrated into the centre of the cavity and drops to smaller values in the outer cells as can be appreciated in Figure 6.5. By using the definitions (2.49) it is possible to quantify the so called field flatness as

$$\eta_1 = 76.81\,\% \quad \text{and} \quad \eta_2 = 92.39\,\%.$$

To achieve the correct distribution of the electromagnetic fields a tuning procedure of the computational domain is required (see section 2.3.4). Since mimicking the mechanical procedure that real cavities are subjected to would be infeasible, the shape is tuned through a numerical optimisation of specific geometry parameters.

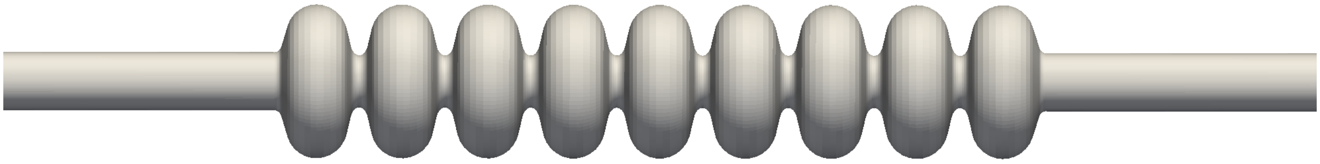

Figure 6.4: Computational domain for the 9-cell TESLA cavity including beampipes at the two ends.

6.3.1 Field Flatness Optimisation

The goal of the optimisation is to achieve an even distribution of the electric field peaks along the cells of the cavity, i.e. η_1 and η_2 defined in (2.49) should be greater than 95 %. Furthermore, the frequency of the accelerating mode should be tuned as close as possible to 1.3 GHz.

To numerically achieve these goals, the geometry parameters that are typically chosen for the optimisation are the length of the two end-cups half-cells l_1 and l_2 and the equatorial radius of the cells R_{eq}. The first two parameters strongly influence the field flatness, while the equatorial radius is mainly responsible for fixing the frequency of the cavity. The three parameters are used for a non-linear constrained optimisation procedure using the Sequential Quadratic Programming (SQP) method [74] in Matlab. The bounds for the parameters are set to ±1.5 mm. The objective function for the optimisation is

$$J_{\mathrm{tune}} = e^{|\eta_1 - 1|} + \gamma e^{|f - f^*|/f^*}, \tag{6.1}$$

where $f^* = 1.3\,\mathrm{GHz}$ and the scalar value γ can be chosen to favour the field or the frequency tuning. In the results shown $\gamma = 10$. The derivative of the objective function are evaluated with centred finite differences.

Figure 6.6 shows the field after the optimisation step. The tuned parameters are

$$l_1 = -0.27879\,\mathrm{mm} \qquad l_2 = -0.15585\,\mathrm{mm} \qquad R_{\mathrm{eq}} = 0.06685\,\mathrm{mm} \tag{6.2}$$

and manage to tune the frequency of the accelerating mode to $f_{\mathrm{tuned}} = 1.300001363$ and the field flatness to

$$\eta_1 = 97.76\,\% \quad \text{and} \quad \eta_2 = 99.15\,\%.$$

In Figure 6.7 the longitudinal electric field E_z of the nine modes in the TM_{010} passband are depicted on a xz cut for the tuned TESLA cavity. Figure 6.7i shows the π-mode: by synchronising the particle beam flying along the axis with the oscillation of the field, the charged particles are always entering a new cell when the longitudinal component of electric field has flipped, always experiencing a force in the correct direction.

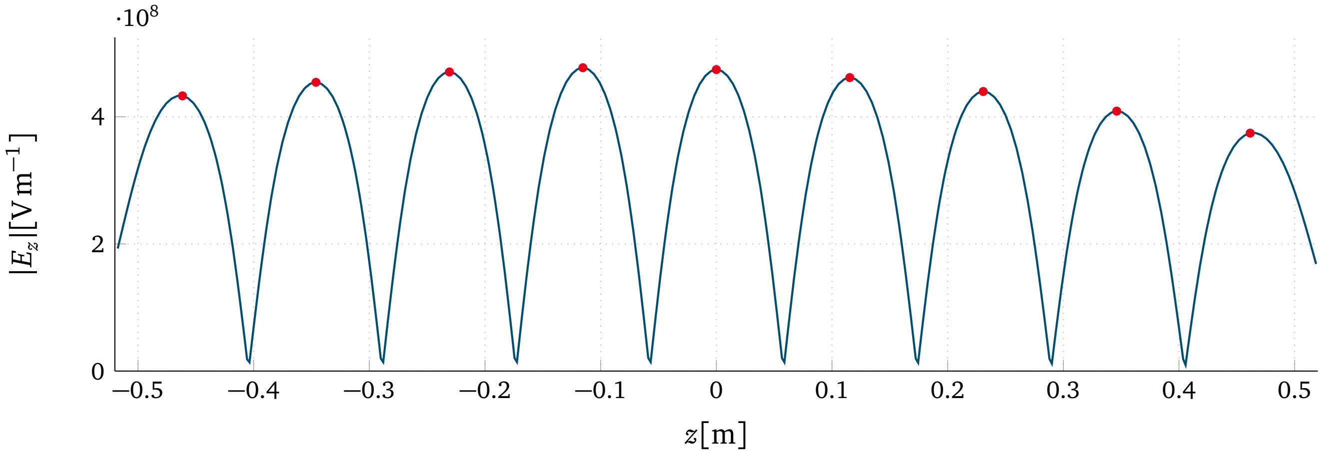

Figure 6.5: Absolute value of the longitudinal electric field $|E_z|$ in the untuned TESLA cavity. The computed value for the field flatness are $\eta_1 = 76.81$ and $\eta_2 = 92.39$.

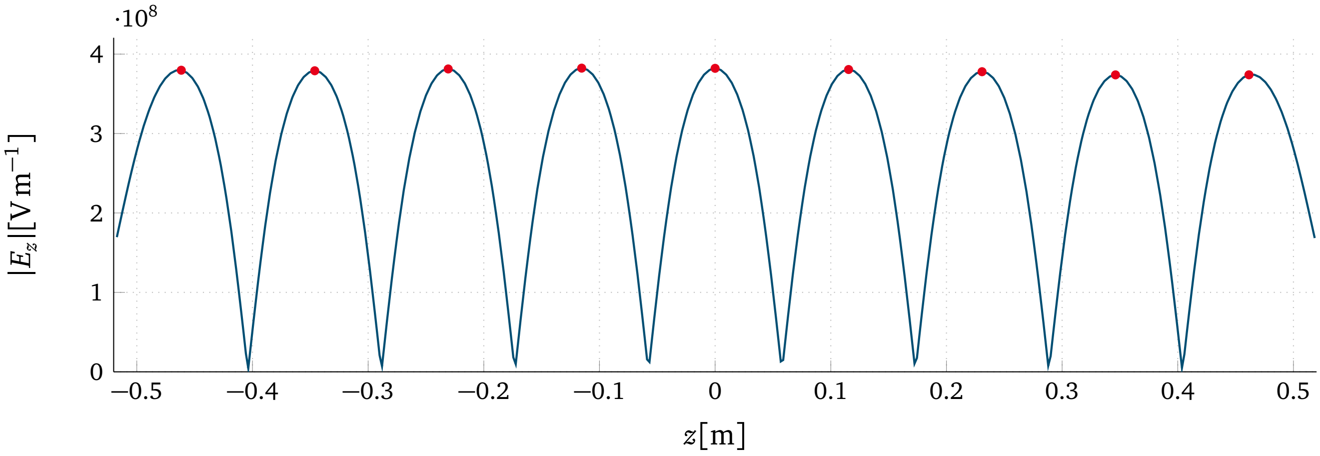

Figure 6.6: Absolute value of the longitudinal electric field $|E_z|$ in the tuned TESLA cavity. The computed value for the field flatness are $\eta_1 = 97.76$ and $\eta_2 = 99.15$.

6.3.2 Lorentz Detuning

Using the tuned geometry parameters (6.2), we evaluate the impact of the Lorentz detuning on the 9-cell TESLA cavity. For this simulation we consider the beampipes to be fixed, i.e. homogeneous Dirichlet boundary conditions are imposed at surfaces Γ_D in Figure 2.9.

The material parameters used to model the behaviour of Niobium in the linear elasticity problem are Young's modulus E and Poissons' ratio ν given by [1]:

$$E = 104.9\,\mathrm{GPa} \qquad \nu = 0.397, \tag{6.3}$$

from which the first and second Lamé parameters can be derived according to (2.54).

The computed value for the deformations are in good agreement with the literature [2] and the computed frequency shift is approximately 1 kHz.

6.4 Optimisation of the Low β Cavity for the S-DALINAC

As a final example we test the tuning procedure on the design of the new injection cavity for the S-DALINAC in Darmstadt [93]. This cavity is currently under development and is supposed to be placed at the beginning of the accelerator structure in order to increase the energy of the particles from the non-relativistic range, to relativistic velocities. As a consequence, conversely to the TESLA cavity presented above, this low β cavity needs to be adapted for particles flying in the range $\beta = 0.2 \sim 0.6$. One of the possible design options foresees a 5-cell superconducting structure whose cells need to be adjusted in length in order to accommodate for the increasing speed of the beam. In particular, the injection energy for the electrons is 100 keV and with an amplitude of 5 $\mathrm{MV\,m^{-1}}$ the cavity should bring the electrons close to the speed of light (95 %). The starting design is depicted in Fig. 6.8 and the geometry parameters are given in Table 6.4.

This design was created by considering the 20-cell non-superconducting structure already in operation as a starting point. A 5-cell cavity is created and scaled to take into account the temperature change from room temperature to the temperature of liquid helium. The cavity is stretched in the longitudinal direction to accommodate for the relativistic change in velocity and then the scaling is distributed geometrically on each cell by a constant factor (see Table 6.5) [72].

This design is not optimised since it is still far off the nominal operational frequency of 3 GHz and energy is not evenly distributed in the cells (see Table 6.6 and Figure 6.9). The equatorial radii R_{eq} of each cell need to be tuned in order to get the correct frequency and field distribution.

For this optimisation the cavity is considered to be magnetically closed at the irises with no beampipes included. As afirst step we do not consider the presence of the input coupler and its three dimensional effects, and the model for the structure is simplified to a 2D section, cut in half along the axis with a symmetric boundary condition and axisymmetric basis functions in order to take into account the rotation. The objective function for the optimisation is the one given in (6.1), but the non-gradient based method Bounded Optimisation BY Quadratic Approximation (BOBYQA) [84] is tested. This method does not require additional function evaluations for the computation of the gradients.

The computed optimal values for the equatorial radii of each cell are given in Table 6.7. The frequency is brought in the kHz range of the nominal frequency and the both η parameters are well above 95 %. A full 3D simulation was performed with the optimised geometry and the longitudinal electric field behaviour can be appreciated in Fig. 6.11.

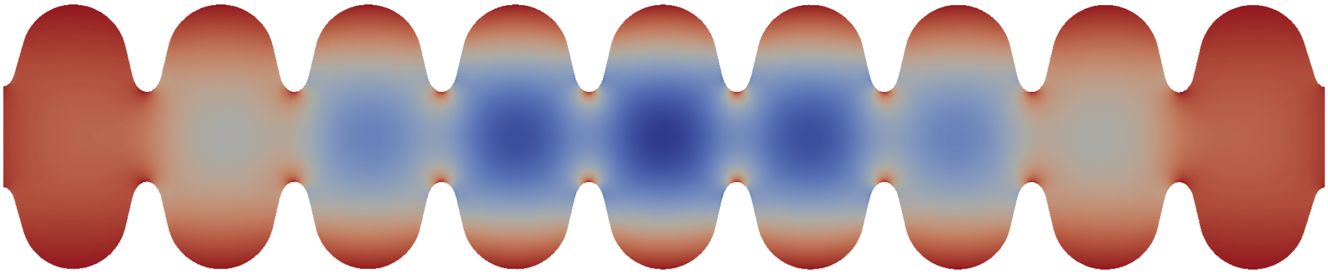

(a) 0-mode

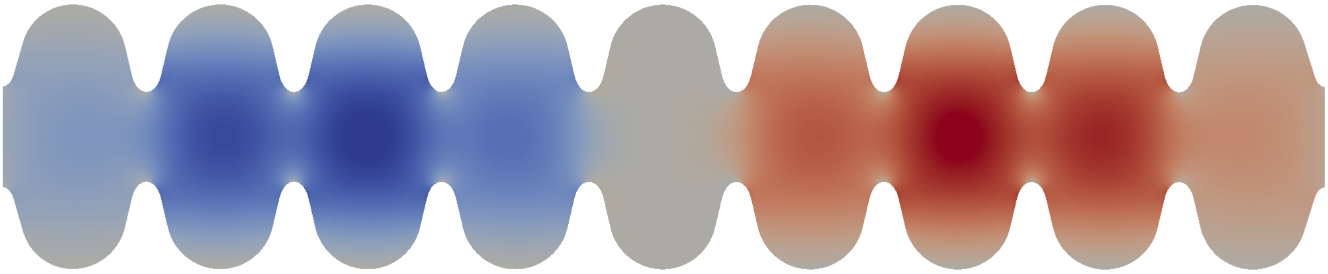

(b) $\pi/2$-mode

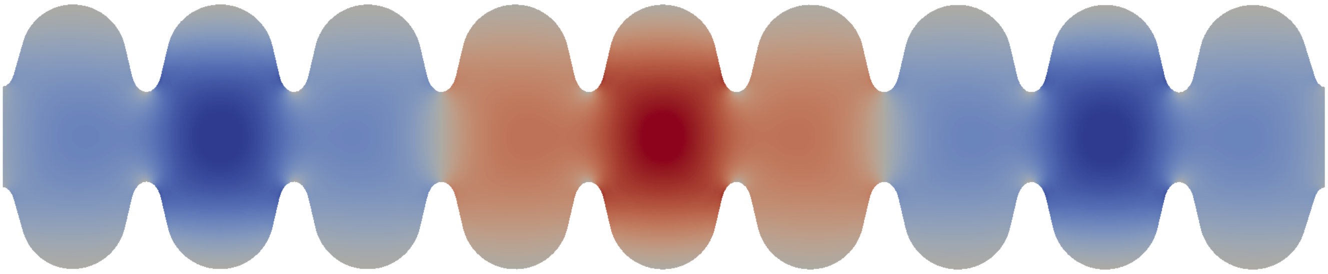

(c) $\pi/3$-mode

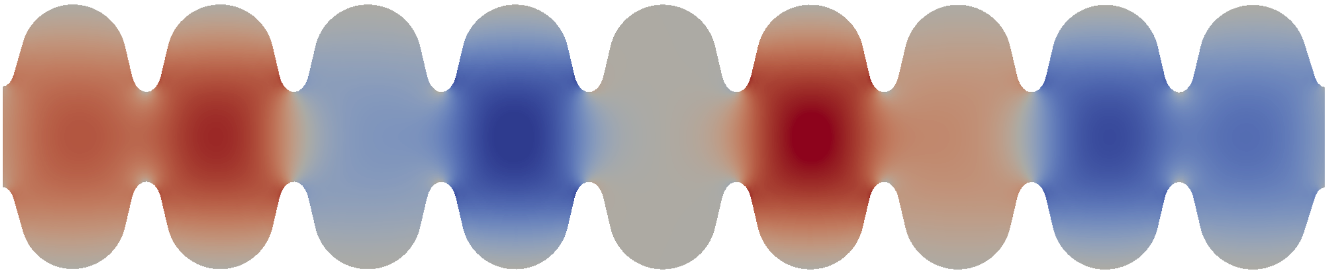

(d) $\pi/4$-mode

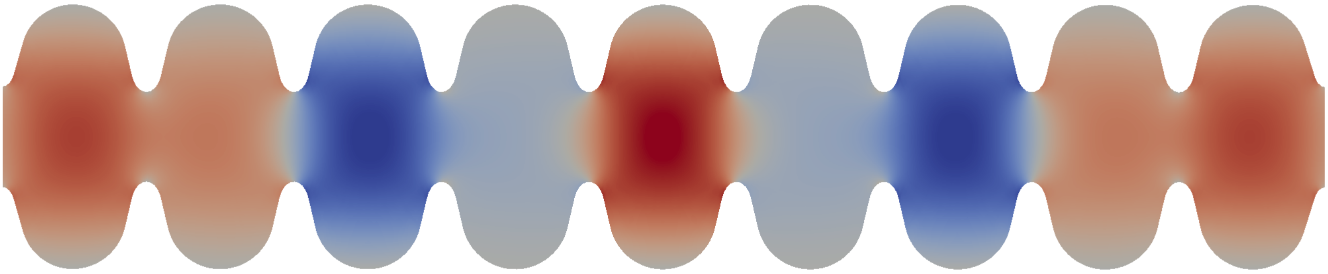

(e) $\pi/5$-mode

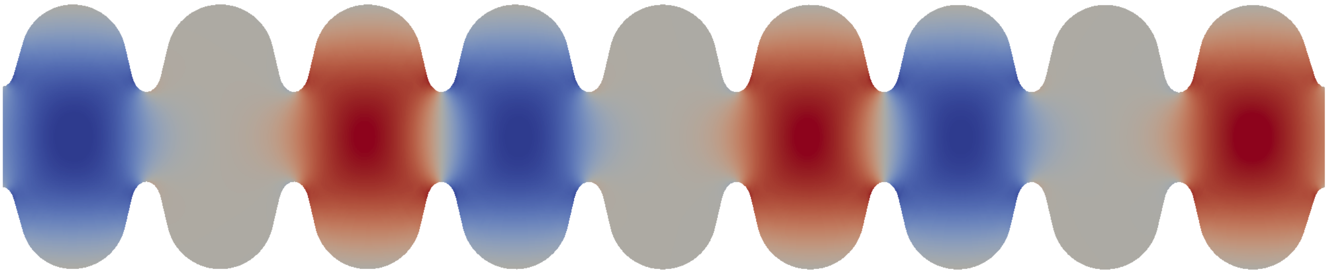

(f) $\pi/6$-mode

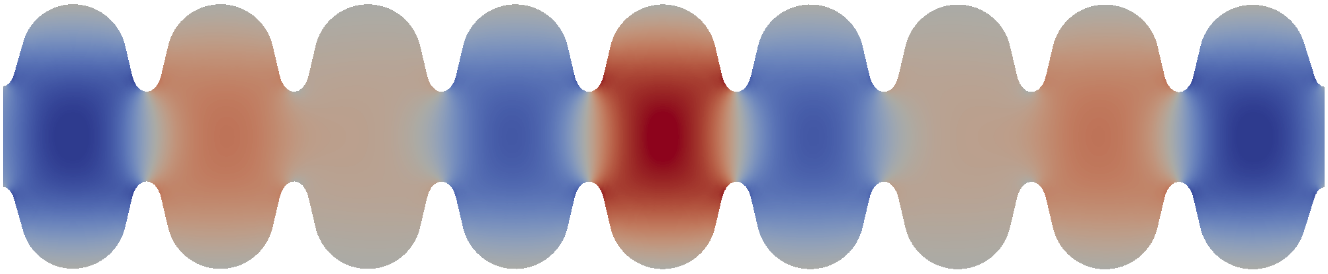

(g) $\pi/7$-mode

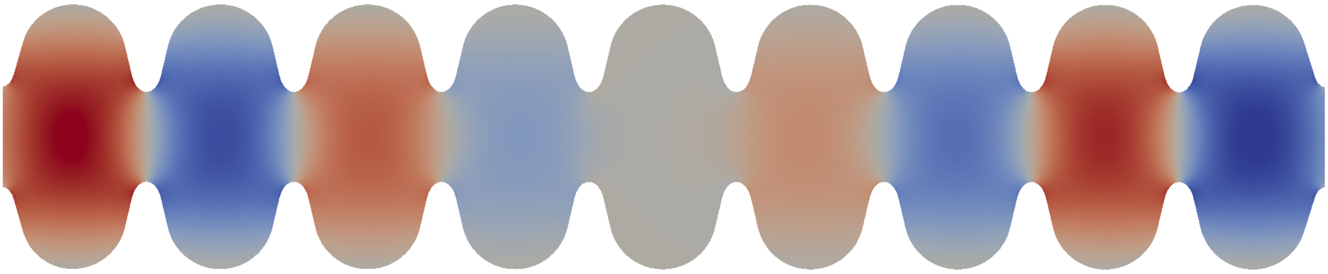

(h) $\pi/8$-mode

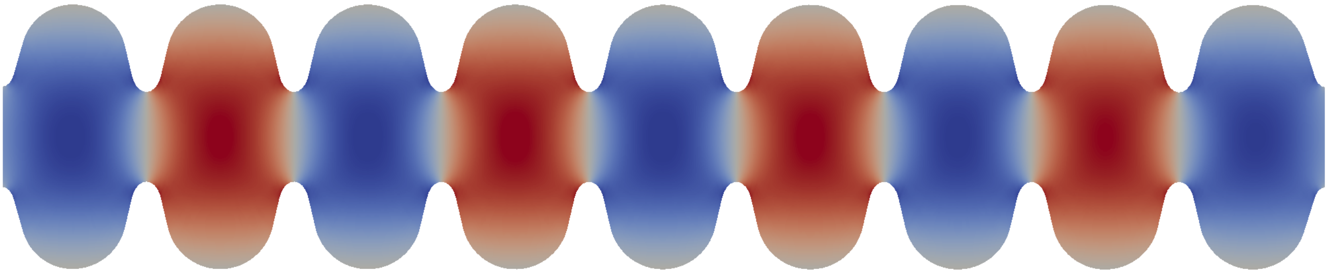

(i) π-mode

Figure 6.7: Longitudinal electric field E_z for the nine modes in the first monopole TM_{010} passband. The results shown are for the tuned TESLA cavity. Mode (i) is the π-mode used for acceleration

Mode	f_{untuned}[GHz]	f_{tuned}[GHz]
1	1.277 374 057	1.276 473 909
2	1.279 420 927	1.278 537 788
3	1.282 571 389	1.281 714 662
4	1.286 460 462	1.285 636 678
5	1.290 629 663	1.289 841 421
6	1.294 577 562	1.293 822 539
7	1.297 820 697	1.297 090 050
8	1.299 964 366	1.299 234 030
9	1.300 848 789	1.300 001 363
10	1.621 334 197	1.621 248 775
11	1.621 334 197	1.621 248 775
12	1.628 968 188	1.629 013 509
13	1.628 968 188	1.629 013 509
14	1.641 812 820	1.641 994 102
15	1.641 812 820	1.641 994 102
16	1.659 631 763	1.659 901 874
17	1.659 631 763	1.659 901 874
18	1.681 784 579	1.682 067 062
19	1.681 784 579	1.682 067 062
20	1.707 262 142	1.707 472 791
21	1.707 262 142	1.707 472 791
22	1.734 736 680	1.734 804 168
23	1.734 736 680	1.734 804 168
24	1.762 629 762	1.762 509 430
25	1.762 629 762	1.762 509 430
26	1.790 107 099	1.789 953 271
27	1.790 107 099	1.789 953 271
28	1.800 638 894	1.800 029 606
29	1.800 638 894	1.800 029 606
30	1.838 171 516	1.837 699 541
31	1.838 171 516	1.837 699 541
32	1.853 816 628	1.853 179 583
33	1.853 816 628	1.853 179 583
34	1.866 180 898	1.865 422 024
35	1.866 180 898	1.865 422 024
36	1.875 227 147	1.874 364 215
37	1.875 227 147	1.874 364 215
38	1.881 501 964	1.880 543 800
39	1.881 501 964	1.880 543 800
40	1.885 610 844	1.884 560 346
41	1.885 610 844	1.884 560 346
42	1.888 082 876	1.886 939 256
43	1.888 082 876	1.886 939 256
44	1.889 348 489	1.888 122 005
45	1.889 348 489	1.888 122 006
46	2.280 721 752	2.280 780 485
47	2.280 721 752	2.280 780 485
48	2.281 209 140	2.281 307 100
49	2.281 209 140	2.281 307 101
50	2.291 023 414	2.291 885 381
51	2.291 149 793	2.292 012 230
52	2.299 863 276	2.299 310 770
53	2.299 984 050	2.299 431 684
54	2.301 940 982	2.301 487 727
55	2.302 062 868	2.301 609 624
56	2.305 045 954	2.304 725 264
57	2.305 169 477	2.304 848 616
58	2.308 776 997	2.308 603 887
59	2.308 902 469	2.308 729 106
60	2.312 690 933	2.312 646 007

Table 6.3: First 60 computed eigenfrequencies in the TESLA cavity for the untuned and tuned configuration. The 9th mode (highlighted in grey) is the TM_{010} π-mode used for acceleration.

It should be pointed out that this tuning is only the first step in the optimisation of the cavity for operation. Future work need to take into account a particle tracking model in order to verify the acceleration of the electrons and attempt to maximise the energy transferred to the beam.

Cavity Shape Parameter	Cell 1	Cell 2	Cell 3	Cell 4	Cell 5
Equator radius R_{eq}	43.445 42	43.445 42	43.445 42	43.445 42	43.445 42
Iris radius R_{iris}	16.5627	16.5627	16.5627	16.5627	16.5627
Horizontal half axis at iris a_1	3.2	3.7184	4.32	5.0208	5.8336
Vertical half axis at iris b_1	3.0592	3.0592	3.0592	3.0592	3.0592
Horizontal half axis at equator a_2	21.98	25.540 76	29.673	34.486 62	40.069 54
Vertical half axis at equator b_2	23.823 52	23.823 52	23.823 52	23.823 52	23.823 52
Length L	25.18	29.259 16	33.993	39.507 42	45.903 14

Table 6.4: Low β cavity design parameters for the different cells. All dimensions are given in mm.

Cell 1	Cell 2	Cell 3	Cell 4	Cell 5
1	1.162	1.350	1.569	1.823

Table 6.5: Horizontal scaling factors for the Low β cavity cells.

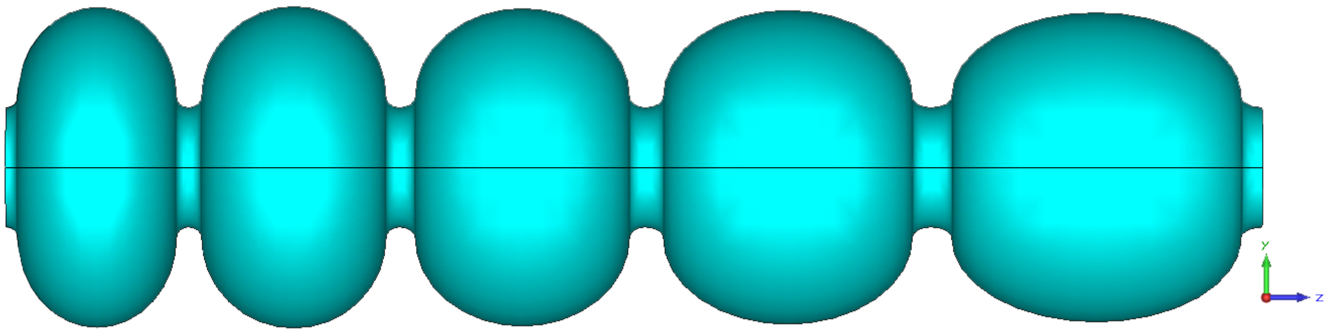

Figure 6.8: Starting design of the low β cavity for the S-DALINAC. The cavity cells get longer in order to take into account the increasing speed of the particle bunch.

Mode	$f_{\text{untuned}}[\text{GHz}]$	$f_{\text{tuned}}[\text{GHz}]$
1	2.954 736 350	2.945 940 528
2	2.983 777 664	2.970 277 189
3	3.005 371 500	2.985 099 410
4	3.024 775 316	2.995 784 608
5	3.061 691 596	3.000 004 153
6	4.001 483 150	4.031 600 710
7	4.259 900 969	4.257 481 710
8	4.552 547 216	4.526 159 368
9	4.902 997 523	4.855 909 938

Table 6.6: First 9 computed eigenfrequencies in the low β cavity for the untuned and tuned configuration. The fifth mode (highlighted in grey) is the TM_{010} π-mode used for acceleration.

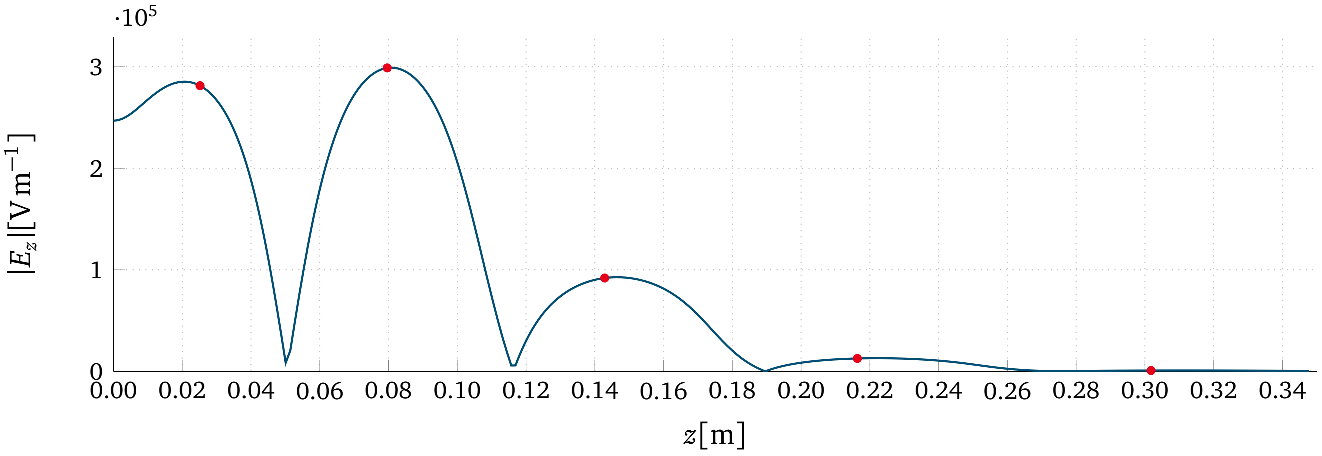

Figure 6.9: Absolute value of the longitudinal electric field $|E_z|$ in the untuned low β cavity. The computed frequency for the TM_{010} π-mode is $f_{\text{untuned}} = 3.061\,691\,596\,\text{GHz}$. The computed value for the field flatness are $\eta_1 = -117.36$ and $\eta_2 = -5.09$.

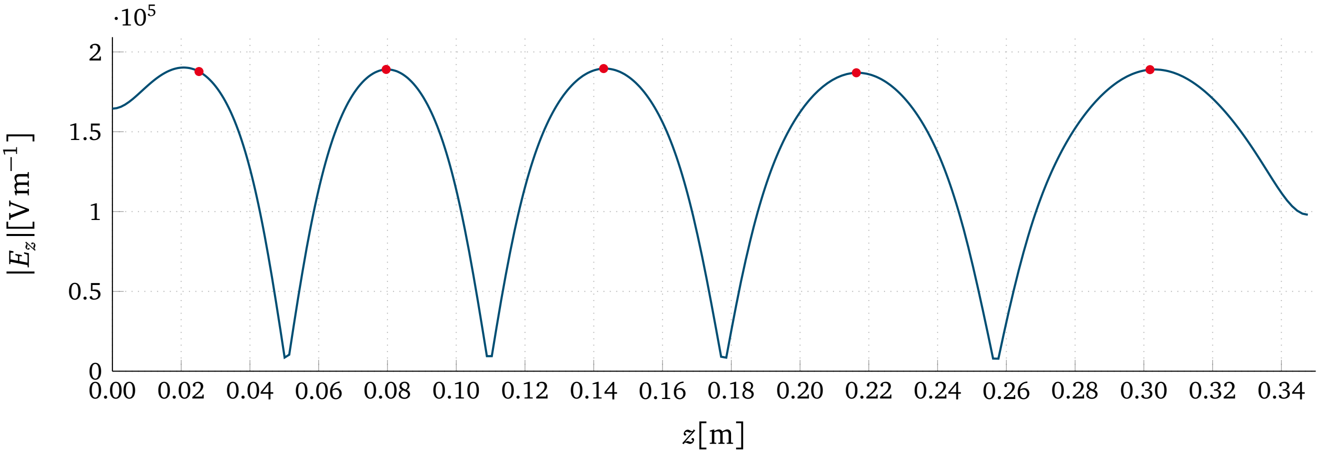

Figure 6.10: Absolute value of the longitudinal electric field $|E_z|$ in the tuned low β cavity. The computed frequency for the TM_{010} π-mode is $f_{\text{tuned}} = 3.000\,004\,153\,\mathrm{GHz}$. The computed value for the field flatness are $\eta_1 = 98.60$ and $\eta_2 = 99.43$.

Cell 1	Cell 2	Cell 3	Cell 4	Cell 5
44.361 42	44.545 42	44.016 42	43.496 42	42.850 42

Table 6.7: Optimum value of R_{eq} for the β cavity cells.

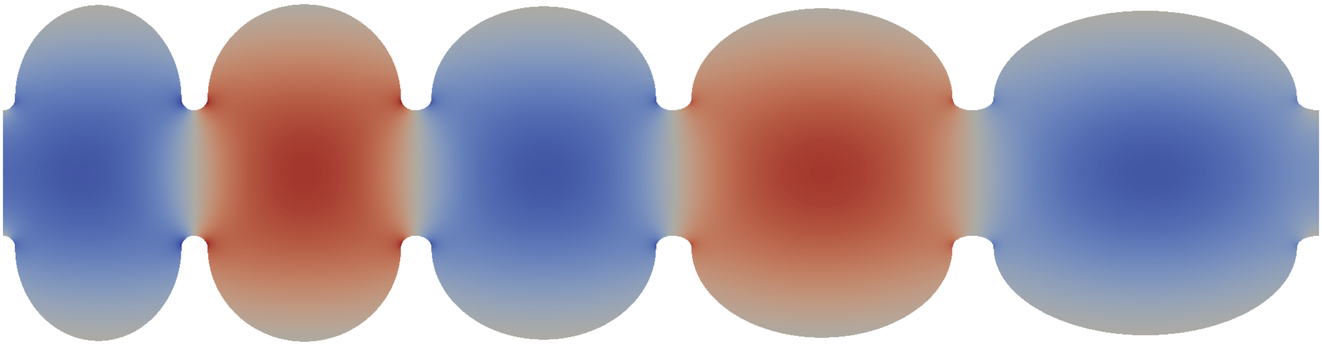

Figure 6.11: Longitudinal electric field in the tuned low β cavity for the S-DALINAC.

7 Uncertainty Quantification

Two eigenvalues enter in a bar
(if you think it's a joke you're quite far!)
'cos when the cavity is changed,
they get mixed and rearranged,
and the result might become too bizarre.

This chapter deals with the evaluation of the sensitivity of the eigenfrequencies of RF cavities with respect to geometrical uncertainties. In the first section we consider, as an example, a pill-box cavity with uncertain radius where a closed form solution is available. We then evaluate the case of a single cell TESLA cavity subject first to uncertain design parameters and, secondly, to elliptical deformations. In the second section, starting from real measurements, we present the case of the 9-cell TESLA cavity with uncertain cell eccentricity. The numerical quadrature for the evaluation of the statistical moments makes use of the eigenvalue tracking algorithm introduced in section 4.4.

7.1 Pill-Box Cavity

As a first example with closed form solution, we consider once again the pill-box case. Let the cylinder height $L = 0.1\,\mathrm{m}$ and the radius R be uncertain. We assume the design value for the radius to be $R = 0.05\,\mathrm{m}$, and that it follows a uniform distribution $R \sim \mathscr{U}(0.04\,\mathrm{m}, 0.06\,\mathrm{m})$. We are interested in the expected value of the eigenfrequencies and their sensitivity to the radius change. The solution of Maxwell's eigenvalue problem in the cavity is obtained using second degree IGA basis functions and 21 692 degrees of freedom. The pill-box cavity as well as the electric and magnetic field distribution of the fundamental TM mode are shown in Fig. 2.3.

In order to be able to correctly classify the eigenmodes for the UQ, we apply the proposed eigenvalue tracking technique introduced in section 4.4 to follow the eigenfrequencies over the parameter range $R = 0.04\,\mathrm{m} - 0.06\,\mathrm{m}$. The exact values are well known (see (2.33) - (2.34)) and a transition of the fundamental mode from TE to TM is expected at approximately $R \approx 0.0492\,\mathrm{m}$.

To illustrate the necessity of the eigenvalue tracking, the frequencies obtained by solving (2.28) at discrete sample points R_i are shown in Fig. 7.1. As it can be appreciated, the eigenvalues cannot be associated to specific modes. It is worth mentioning that, in this simple example, the eigenmodes can be distinguished as a post processing step by analysing the eigenvectors. Since the deformed cavity maintains

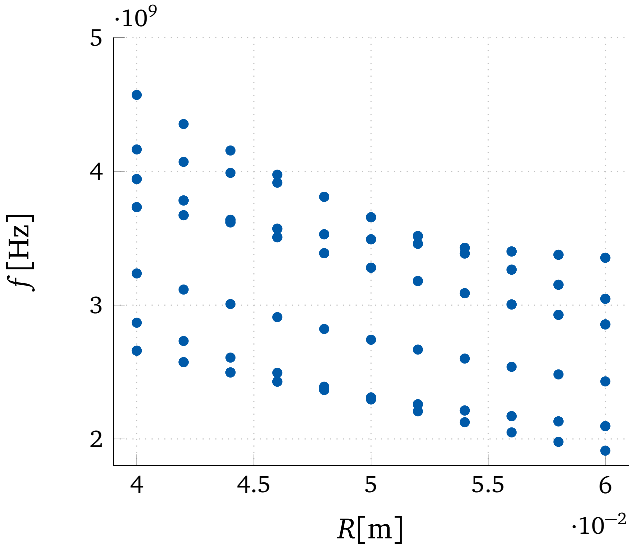

Figure 7.1: Eigenvalues in the pill-box cavity for different values of the radius R.

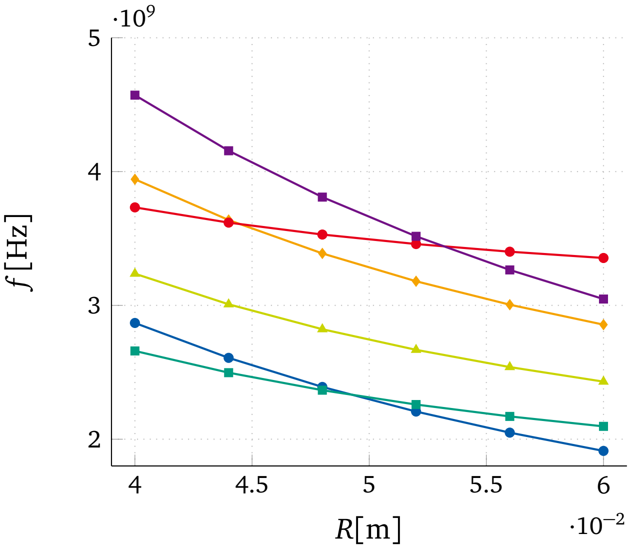

Figure 7.2: Traced eigenvalues in the pill-box cavity.

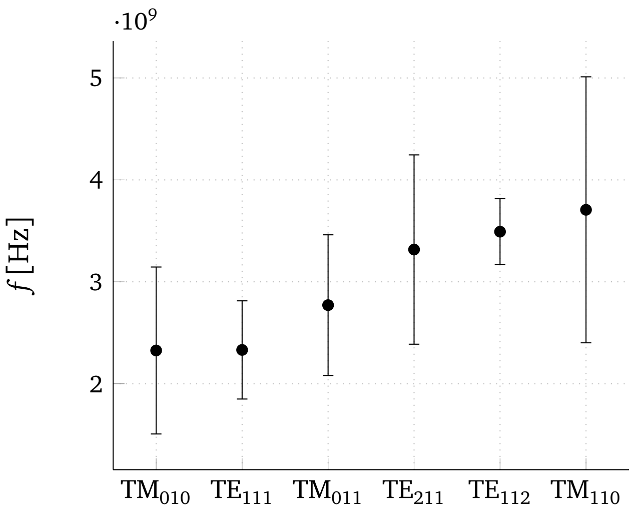

Figure 7.3: Expectations and 3σ-intervals for the eigenfrequencies in the pill-box cavity with uncertain radius R.

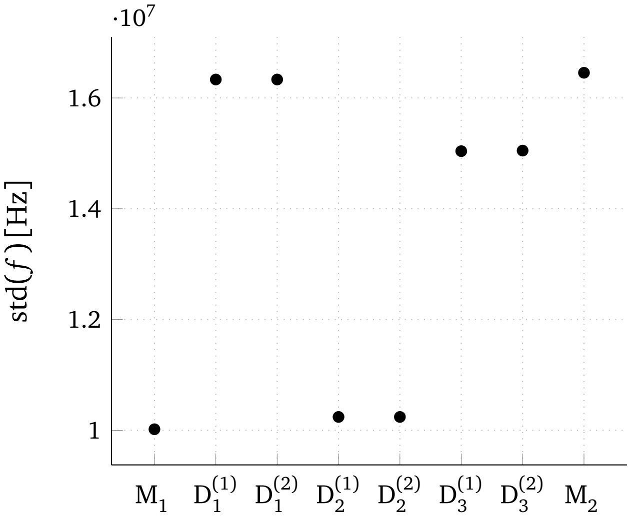

Figure 7.4: Standard deviation for the frequencies in the 1-cell TESLA cavity with uncertain design parameters.

its cylindrical shape for any value R_i, the electric field distribution can be used to uniquely identify the modes as TM_{mnp} or TE_{mnp} and the degenerate modes remain degenerate in any configuration such that it is irrelevant to distinguish them. However, this is not possible for general deformed cavities where more complicated deformations may disrupt the classification into TE and TM modes and separate or unify degenerated solutions, rendering the distinction between them relevant.

For this example, we substitute the algebraic homotopy (4.19) with the physical system matrices $\mathbf{K}(R)$ and $\mathbf{M}(R)$ such that all eigenvalue problems correspond to the actual deformed geometries. In this case, the derivatives $\mathbf{K}'$ and $\mathbf{M}'$ are obtained by applying finite differences. Figure 7.2 demonstrates the results of tracking eigenvalues and is able not only to correctly identify the change in fundamental mode, but also the crossing of the HOMs.

To determine the first two statistical moments of the 6 lowest eigenfrequencies at the midpoint $r = 0.5$ we create a one dimensional grid of $N = 5$ Clenshaw-Curtis collocation points and use Gaussian quadrature as explained in section 4.3.2. The results are depicted in Fig. 7.3. The relative errors of the numerical estimates with respect to the closed form reference solution are below $3.5 \cdot 10^{-4}$ for both expectation values and standard deviations.

The same tracking technique is applied for the sensitivity analysis of the first 8 frequencies in the 1-cell TESLA cavity under different kinds of shape uncertainties. First we consider the 7 design parameters (see Table 2.1) to be uncertain. The deviations with respect to the nominal value are uniformly distributed in the range of $\pm 1\,\text{mm}$, i.e. $\sim \mathscr{U}(-1\,\text{mm}, 1\,\text{mm})$. A Clenshaw-Curtis grid of level 2 is constructed for a total of 113 collocation points. The eigenvalue problem is solved for one deformed configuration which is used as reference for the construction of the homotopies to the other points in the parameter domain. For each of these points and for every mode, the algorithm in Fig. 4.3 is used and the computed frequencies are used to evaluate the mean value and the standard deviation using equations (4.17). The results (see Fig. 7.4) show that the first monopole mode M_1 and the second dipole mode D_2 are less sensitive than the other ones. It is also worth noticing that since the random input does not affect the cylindrical symmetry of the cavity, both polarisations of the dipole modes behave in the same way.

As a second case, we introduce three dimensional effects by disrupting the axisymmetry of the cavity. Given the design parameters that outline the wall of the cavity, instead of a straightforward revolution around the cavity axis, we consider a revolution along an elliptical path

$$x = a\cos(t) \tag{7.1}$$

$$y = b\sin(t), \tag{7.2}$$

with a and b uniformly distributed. In particular $a, b \sim R_{\text{eq}} + \mathscr{U}(-2\,\text{mm}, 2\,\text{mm})$. Using a level 3 Clenshaw-Curtis grid (29 collocation points in total) we repeat the analysis as in the previous case. In fig. 7.5a it is possible to notice that the standard deviations for all the modes are similar, but in this instance the second dipole mode is the most affected. Although the geometry changes the rotational symmetry, since parameters a and b have the same distribution, the behaviour of the different polarisation of dipole modes remains symmetric.

As a consequence, as a final test, we consider only parameter a to be uncertain. The results depicted in Fig. (7.5b) show the different impact of the shape deformation on the different polarisation of the first and second dipole modes. It is important to mention that without the tracking method, it would be extremely difficult to differentiate between the two polarisations since a visual verification for all the computed modes would be required.

7.2 9-cell TESLA Cavity with Eccentric Cells

The final application example we consider is derived from real cavity measurements obtained from the DESY database [40]. The database contains measurements of different shape parameters for several hundreds of cavities produced for the FEL FLASH, both before and after welding of the half-cells. In particular we consider the measures of the position of each of the cell's centres with respect to the ideal axis of the cavity (see Fig. 7.6).

We consider 18 variables, corresponding to the displacement of the nine cell's centres in the x and y direction and we collect approximately 700 observations for each of them in a matrix $\mathbf{T}$. The deformations appear to be normally distributed, but they also show correlation between each other. To obtain uncorrelated variables for the UQ process, and to reduce the size of the parameter space, the truncated Karhunen–Loève decomposition introduce in section 4.2 is applied. This allows for the reduction from 18 to 7 variables.

Given the vector of mean values

$$\boldsymbol{\mu} = \begin{bmatrix} \mu_x^1 & \dots & \mu_x^9 & \mu_y^1 & \dots & \mu_y^9 \end{bmatrix}, \tag{7.3}$$

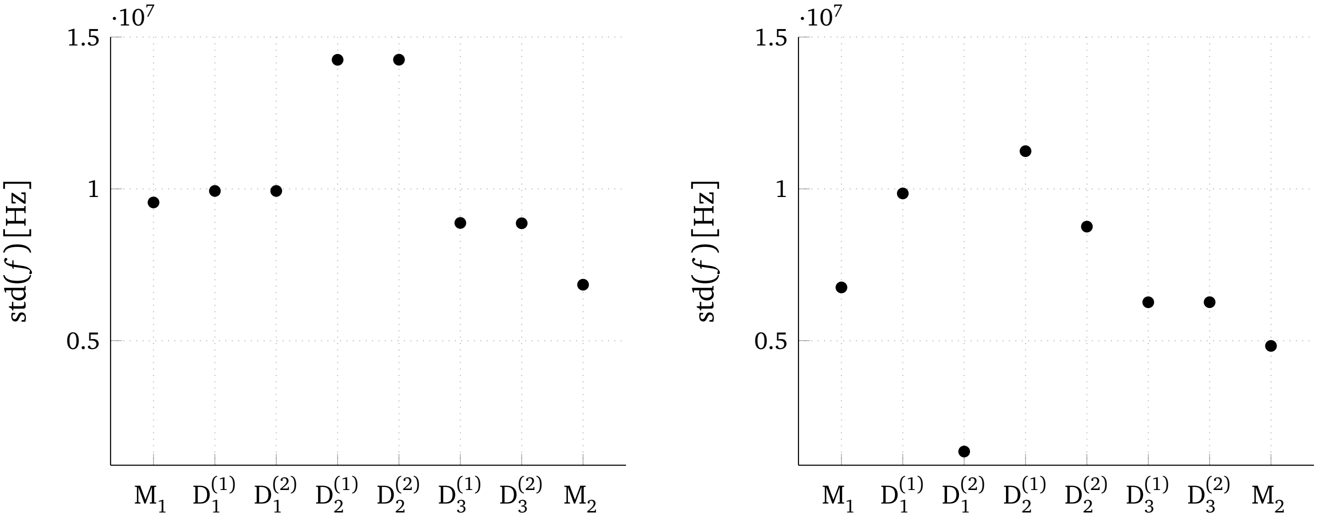

(a) Both a and b are uncertain.

(b) Only a is uncertain.

Figure 7.5: Standard deviation for the frequencies in the 1-cell TESLA cavity with uncertain elliptic shape. On the left both axis a and b of the ellipse are random variables with uniform distribution, on the right only the a axis is varying.

with μ_x^i and μ_y^i the mean values for the x and y displacement of the centre of the i-th cell respectively, and the coordinates of the centres of the cells z^i, we create the set of points

$$\mathbf{Q}_\mu = \begin{bmatrix} \mu_x^1 & \dots & \mu_x^9 \\ \mu_y^1 & \dots & \mu_y^9 \\ z^1 & \dots & z^9 \end{bmatrix}, \tag{7.4}$$

which represent the expected centres of the cells. Given these points it is possible to construct the interpolating B-Spline curve $\mathbf{C}_\mu$ [83, chapter 9], with control points $\mathbf{P}_\mu$. By knot insertion [83, chapter 5], we can ensured that the curve $\mathbf{C}_\mu$ has the same number of control points that the TESLA cavity geometry has in the z direction.

In an analogous way, we consider the columns $\mathbf{z}_1, \dots, \mathbf{z}_7$ of the eigenvalue decomposition matrix $\mathbf{Z}_{\mathrm{tKL}}$ (see Eq. (4.9)) and we create the points $\mathbf{Q}_{\mathrm{KL}}^j$, for each column $j = 1, \dots, 7$, which do not have a physical interpretation any more, other than being a representation of the variability of the j-th Karhunen–Loève mode. A set of interpolating B-Spline curves $\mathbf{C}_{\mathrm{KL}}^j$, with control points $\mathbf{P}_{\mathrm{KL}}^j$, is constructed.

The collocation points for the numerical quadrature are created with a Smolyak grid of level 2, with 3 Gaussian points along each direction, for a total of 127 points. For a given collocation point $\mathbf{y}_m$ it is possible to use Karhunen–Loève expansion (4.10) and the curves $\mathbf{C}_\mu$ and $\mathbf{C}_{\mathrm{KL}}^j$ to build the deformation curve $\mathbf{C}_\mathrm{y}$ which has control points

$$\mathbf{P}_\mathrm{Y} = \mathbf{P}_\mu + \sum_{j=1}^{7} y_j \mathbf{P}_{\mathrm{KL}}^j, \tag{7.5}$$

where we have exploited the fact that both curves have the same basis (see Eq. (3.24)). Since $\mathbf{C}_\mathrm{y}$ belongs to the same space as the TESLA geometry mapping, it is possible to easily deform the domain shape to obtain the deformed cavity at point $\mathbf{y}$. In Fig. 7.8 the deformed domain is shown.

The results for the standard deviations of the 9 modes in the first TM_{010} passband are depicted in Fig. 7.7. These correspond to deformations 50 times bigger than the measured once in order to be able to catch the variability with a reasonable accuracy without needing a hugely refined mesh. It is noticeable how the last two modes in the passband are more than 4 times more sensitive than the other ones.

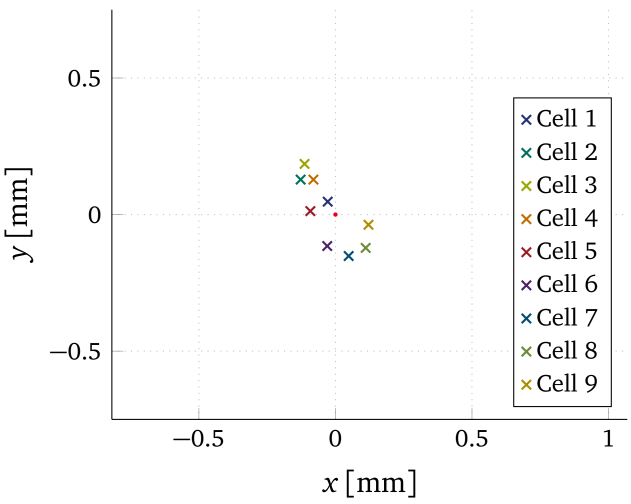

Figure 7.6: TESLA cells eccentricity measurements.

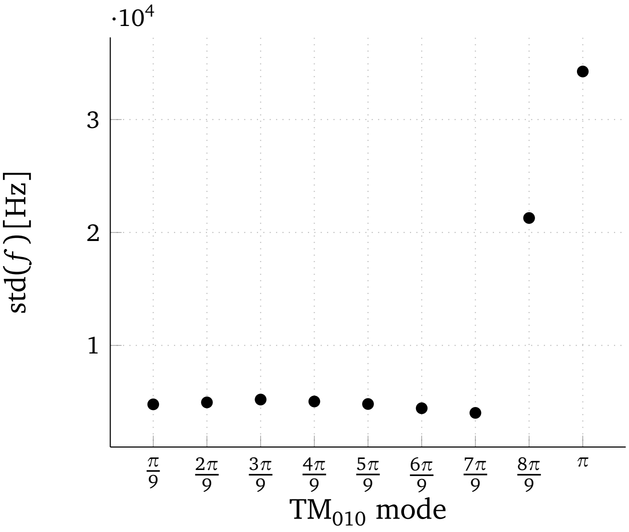

Figure 7.7: Standard deviation of the TM_{010} mode in the TESLA cavity with eccentric cells. The results are obtained with deformations 50 times bigger than the measured ones.

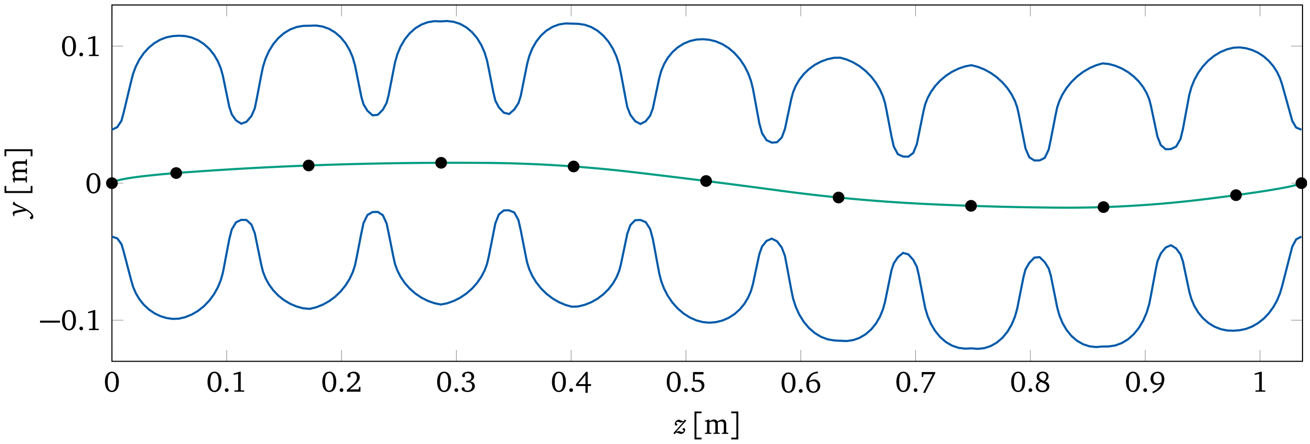

Figure 7.8: Outline of a TESLA cavity with eccentric cells. The deformation is enhanced of a factor 500. In black the offsetted centres of the cells, in green the interpolating curve and in blue the deformed cavity.

8 Cavity Substructuring

Some test I will show you below,
to ensure that the methods don't blow.
Both Mortar and SSC
on this point can agree:
that the beta should reach a plateau.

In this chapter we present some tests of the applicability of the two substructuring methods introduced in section 5. First we consider the Mortar method both in the case of a single patch and of a multipatch geometry. Then 2 TESLA cavity cells are coupled together and the results are compared to the simulation of the complete geometry. The inf-sup condition (5.20) is evaluated numerically and the stability is verified. The SSC method is then considered in section 8.2. Finally the simulation results for a full TESLA cavity, including the HOMs, obtained by combining both methods is presented.

8.1 Mortar Method

In this section we first test the simple case of a single patch to single patch coupling and then the multipatch case in section 8.1.2 and 8.3.

8.1.1 Single Patch

The first test performed is a single patch-to-patch coupling. A cubic domain Ω is split in half along the z direction into Ω_1 and Ω_2 (see Fig. 8.1). We call Γ the interface between the two. Maxwell's eigenvalue problem (2.28) is solved using the Mortar approach described in section 5.3. In Ω_1 we choose an IGA curl-conforming discretisation with degree $p_{\text{IGA}} = 4$ and high regularity $r_{\text{IGA}} = 3$, while in Ω_2 a FEM discretization with Nédélec type hexahedral elements is used with degree p_{FEM} between one and three. This is accomplished in GeoPDEs by setting the regularity of the basis function space to $r_{\text{FEM}} = 0$. The grids on the two sides are chosen in such a way that they never match.

On the interface Γ we build the space of Lagrange multipliers with $p_\Gamma = 1, 2, 3$ and $r_\Gamma = p_\Gamma - 1$, using space (5.12). The mesh used for the quadrature is given by the intersection of the meshes on both sides which is easy to compute given the tensor product nature of the IGA hexahedral grid.

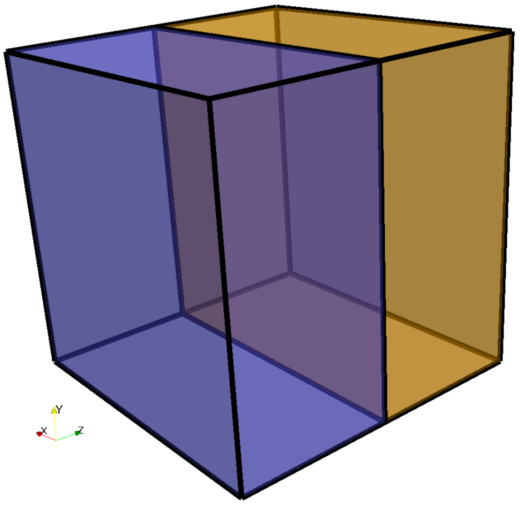

Figure 8.1: Mortar coupling between two patches Ω_1 (in blue) and Ω_2 (in orange).

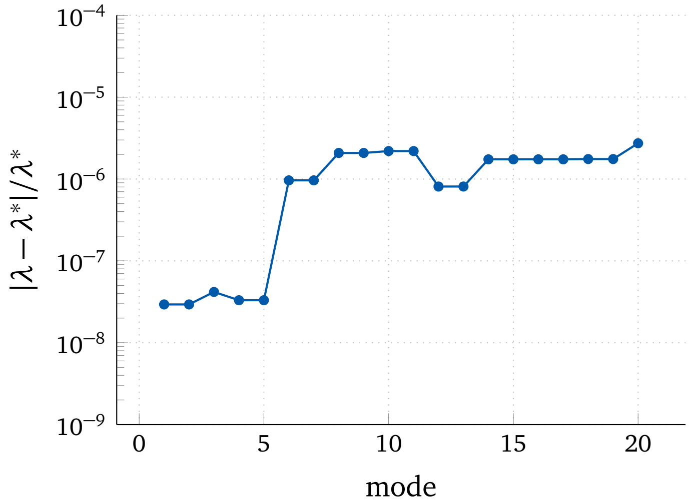

Figure 8.2: Mortar coupling between two patches. Relative error of the first 20 eigenvalues with $p_{\mathsf{IGA}}=4$, $p_{\mathsf{FEM}}=3$, $p_\Gamma=3$, $N_{\mathrm{dof}}=21\,160$.

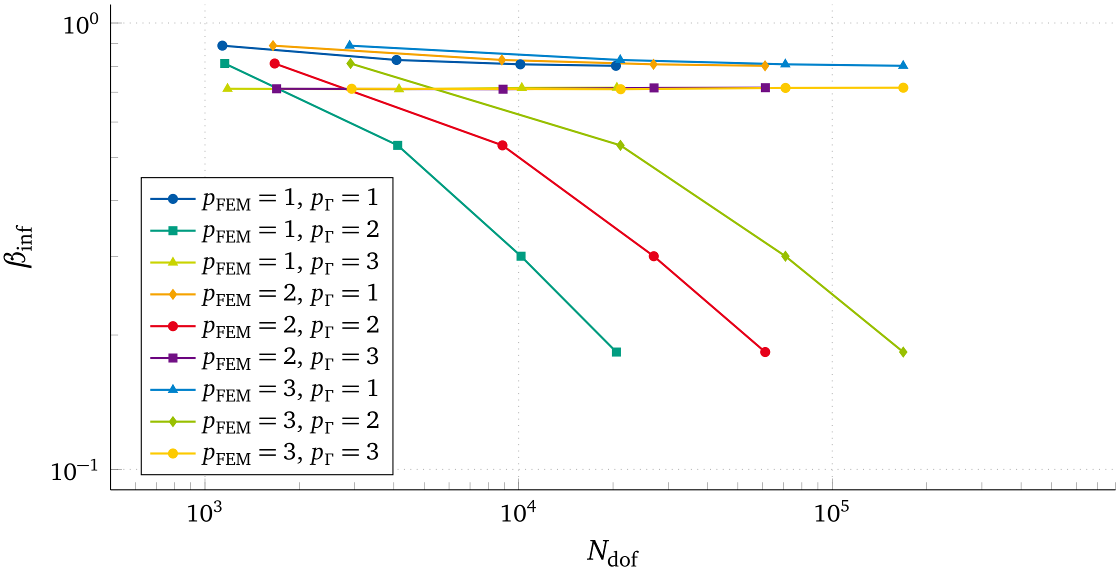

Figure 8.3: Mortar coupling between two patches: β_{inf} constants for different space choices. When $p_\Gamma=p_{\mathsf{IGA}}-2$, β_{inf} goes to zero.

Given a, b and c the dimensions of the cube along each direction, the eigenvalues can be computed analytically by the formula [61]

$$\lambda=\omega^2=\left(\frac{m\pi}{a}\right)^2+\left(\frac{n\pi}{b}\right)^2+\left(\frac{p\pi}{c}\right)^2 \tag{8.1}$$

$\forall m,n,p\geq 0$ with at most one index equal to zero. The first 20 eigenvalues and the numerical estimates for the inf-sup constant β_{inf} (see section 5.3.2) are computed for varying discretisation choices on the two subdomains by solving generalised eigenvalue problem (5.21). In Fig. 8.2 the relative errors of those eigenvalues with respect to the closed form solution are reported for the case of $p_{\mathrm{FEM}}=3$, $p_\Gamma=3$ and with a total number of degrees of freedom $N_{\mathrm{dof}}=21\,160$.

In Fig. 8.3 the inf-sup constants with increasing mesh refinement are shown for fixed $p_{\mathrm{IGA}}=4$ and different combinations of p_{FEM} and p_Γ. As expected from the theory [26] the saddle-point problem is unstable when $p_\Gamma=p_1-2$.

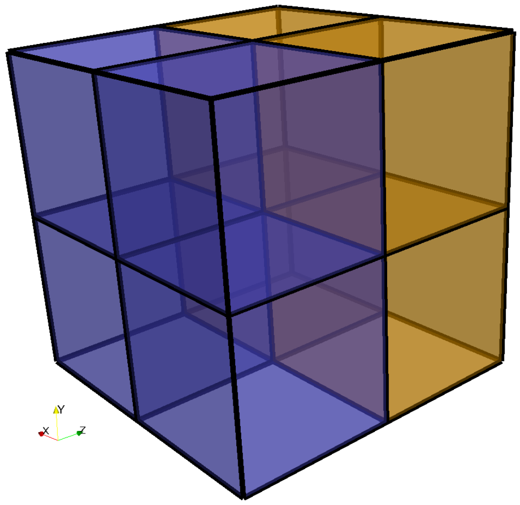

Figure 8.4: Mortar coupling between two multipatch domains Ω_1 (in blue) and Ω_2 (in orange).

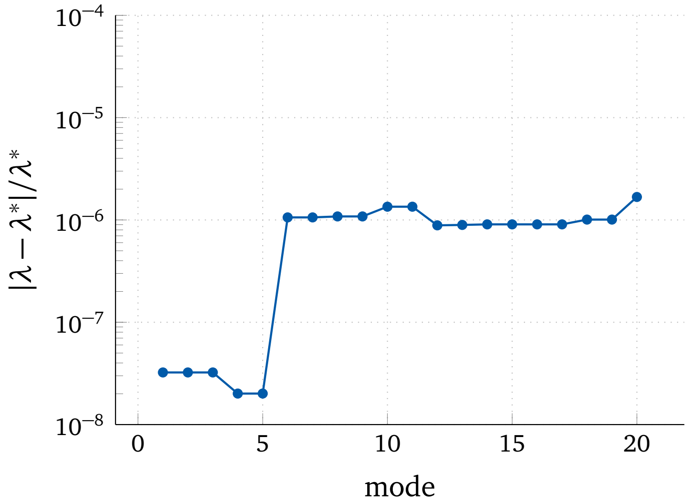

Figure 8.5: Mortar coupling between two multipatch domains. Relative error of the first 20 eigenvalues with $p_{\text{IGA}} = 4$, $p_{\text{FEM}} = 3$, $p_\Gamma = 3$, $N_{\text{dof}} = 26\,298$.

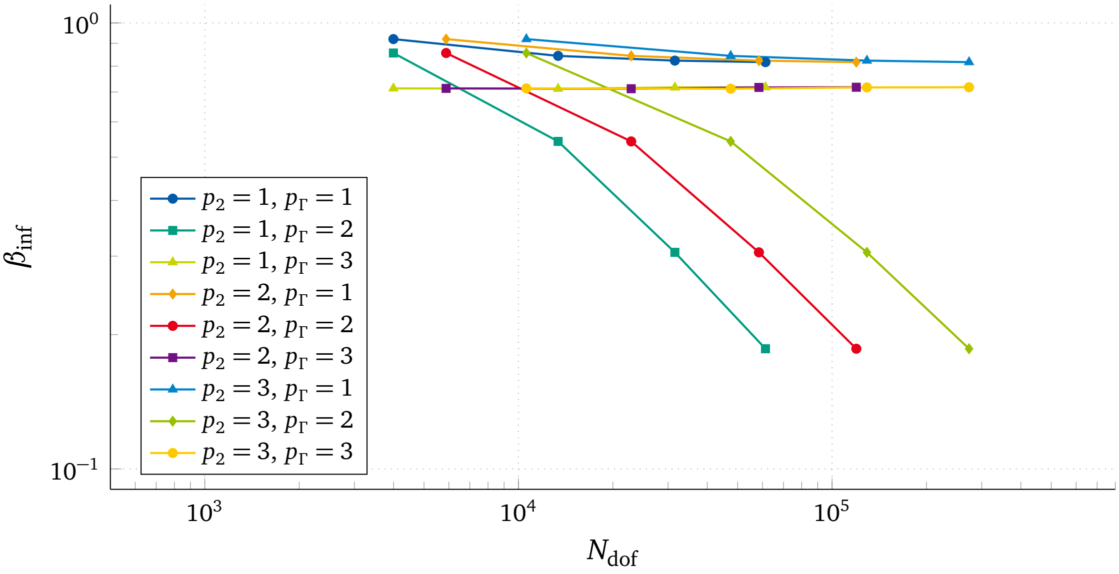

Figure 8.6: Mortar coupling between two multipatch domains: β_{inf} constants for different space choices. When $p_\Gamma = p_{\text{IGA}} - 2$, β_{inf} goes to zero.

8.1.2 Multipatch

In the case of multipatch geometries two tests are shown. In the first case we start from the same geometry as in section 8.1.1 but the two subdomains Ω_1 and Ω_2 are further split into four patches (see Fig. 8.4). The discretisation spaces on both sides are constructed following the classical multipatch approach (see section 3.6) such that degrees of freedom lying on adjacent interfaces are glued together. The Lagrangian multipliers basis is given by the union of the basis of the four patches subdividing the interface Γ. Analogous results as in the previous section are depicted in Fig. 8.5-8.6 and show the same behaviour of the two patches case.

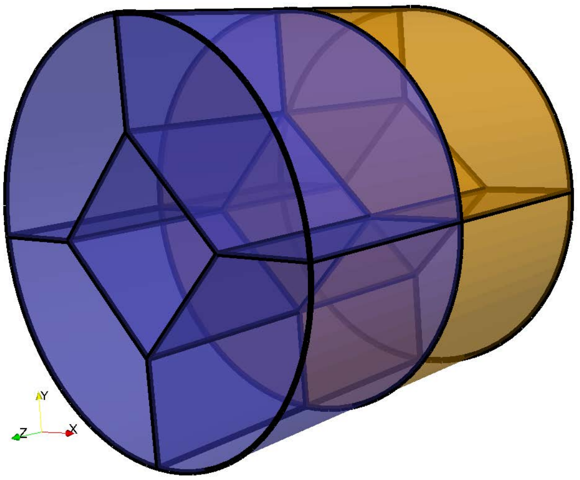

Figure 8.7: Mortar coupling between two pill-box multipatch domains Ω_1 (in blue) and Ω_2 (in orange).

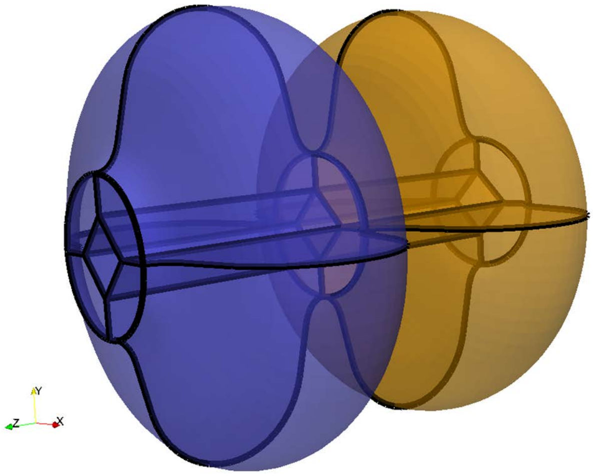

Figure 8.8: Mortar coupling between two TESLA cells Ω_1 (in blue) and Ω_2 (in orange).

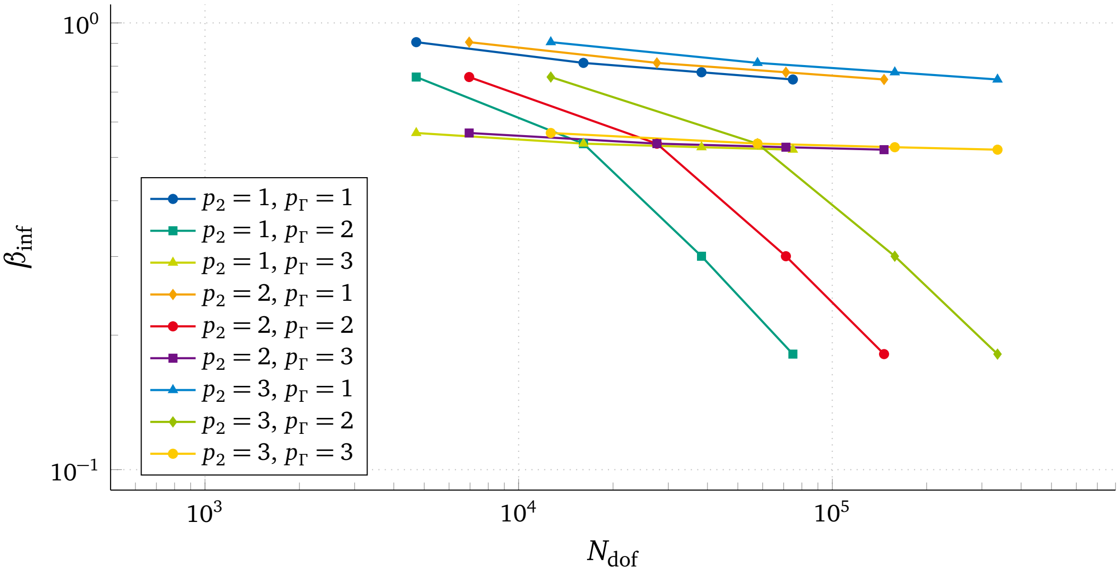

Figure 8.9: Mortar coupling between two multipatch pill-box domains: β_{inf} constants for different space choices. When $p_\Gamma = p_{\text{IGA}} - 2$, β_{inf} goes to zero.

The same test was performed on a cylindrical cavity (see Fig. 8.7) filled with vacuum. The closed form expressions for the eigenfrequencies in a cylinder of radius R and height L are given by [61]

$$f_{TM} = \frac{c}{2\pi}\sqrt{\left(\frac{\chi_{nm}}{R}\right)^2 + \left(\frac{p\pi}{L}\right)^2} \qquad \forall m \geq 0, n \geq 1, p \geq 0 \tag{8.2}$$

$$f_{TE} = \frac{c}{2\pi}\sqrt{\left(\frac{\chi'_{nm}}{R}\right)^2 + \left(\frac{p\pi}{L}\right)^2} \qquad \forall m \geq 0, n \geq 1, p \geq 1. \tag{8.3}$$

In Fig. 8.9 the results for the inf-sup constant are shown.

For the SSC method we perform similar tests as for the Mortar case. For the SSC algorithm we are particularly interested in studying the behaviour of the solution with respect to the number of waveguide modes selected as Lagrange multipliers.

Let us consider the two-patch geometry in Fig. 8.1. Given the interface is a square, the waveguide eigenmodes φ_k are computed analytically using equation (2.24) and the coupling matrices are obtained using (5.28). Figure 8.10 shows the convergence of the first and tenth eigenvalue to the exact solution for the case of matching and non-matching grids, and for different choices of the discretisation degrees, while keeping fixed the number of waveguide modes $N_\Gamma = 18$.

In Fig. 8.11 we present the relative errors of the first 20 computed eigenfrequencies in the cube obtained with a fixed the B-Spline discretisation on both sides ($p_1 = 3$, $r_1 = 2$ and $p_2 = 2$, $r_2 = 1$ with non-matching grids on the interface) while increasing the number of analytical waveguide modes on the interface. It is noticeable how N_Γ influences the spectral approximation, in particular, when not enough modes are chosen, since some eigenfunctions can not be represented by the Lagrange multiplier, some of the higher order modes are not correctly captured. However the size of the coupling space can not be taken arbitrarily big since the saddle-point becomes unstable. This is illustrated in Fig. 8.12, where the β_{inf} constant is computed for different choices of N_Γ using the numerical test introduced in section 5.3.2. It is evident that increasing N_Γ causes the method to fail if the two subdomains are not refined accordingly.

As mentioned in section 5.4, the SSC coupling allows for straightforward coupling of completely different grids, since the construction of the coupling matrices $\mathbf{B}_1$ and $\mathbf{B}_2$ is completely independent. In Fig. 8.13 the convergence of the first eigenvalue in the cube for an IGA-FEM coupling is shown.

Similarly to the Mortar case, we consider now the pill-box geometry showed in Fig. 8.7. The interface Γ is a circle, thus the closed form solutions (2.26) and (2.27) can be used to exactly evaluate the waveguide modes φ_k. We use both the TE and TM modes as the basis. The results for the computed eigenfrequencies are reported in Table 8.1 along with the exact values. It is evident that some spurious modes appear in

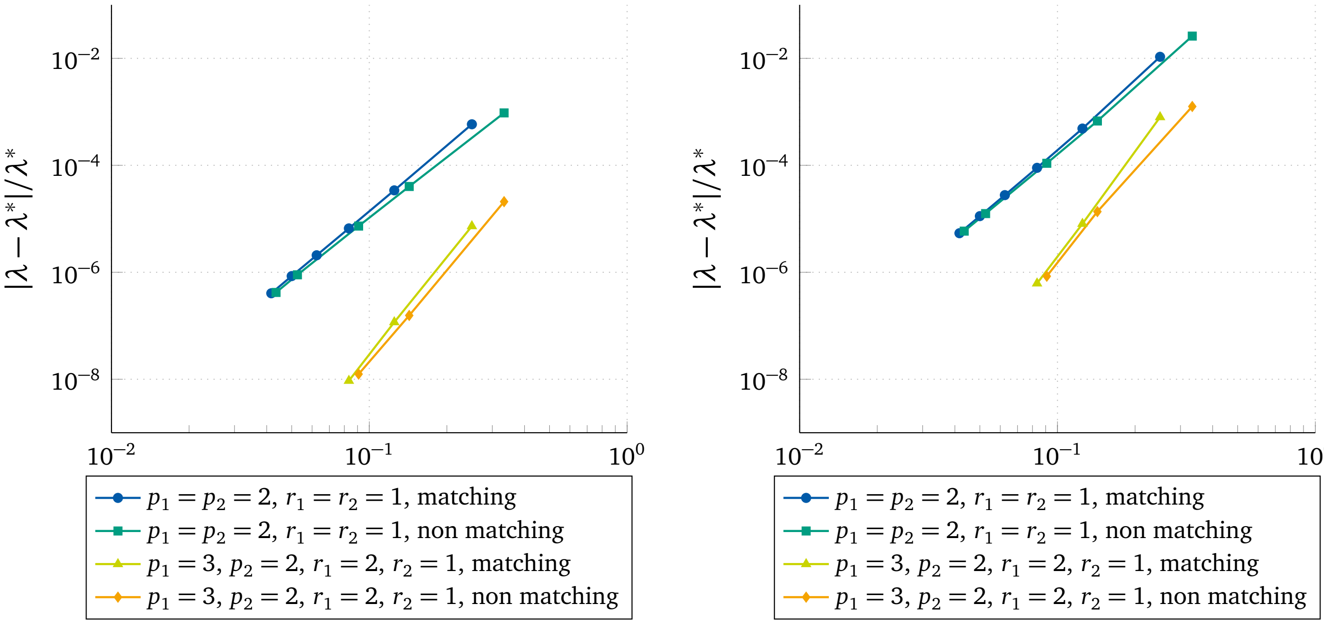

(a) Convergence of the first eigenvalue

(b) Convergence of the tenth eigenvalue

Figure 8.10: SSC coupling on a multipatch cube: eigenvalue convergence for different choices of the discretisation degrees and for matching and non matching grids on Γ. The number of waveguide modes is fixed to $N_\Gamma = 18$.

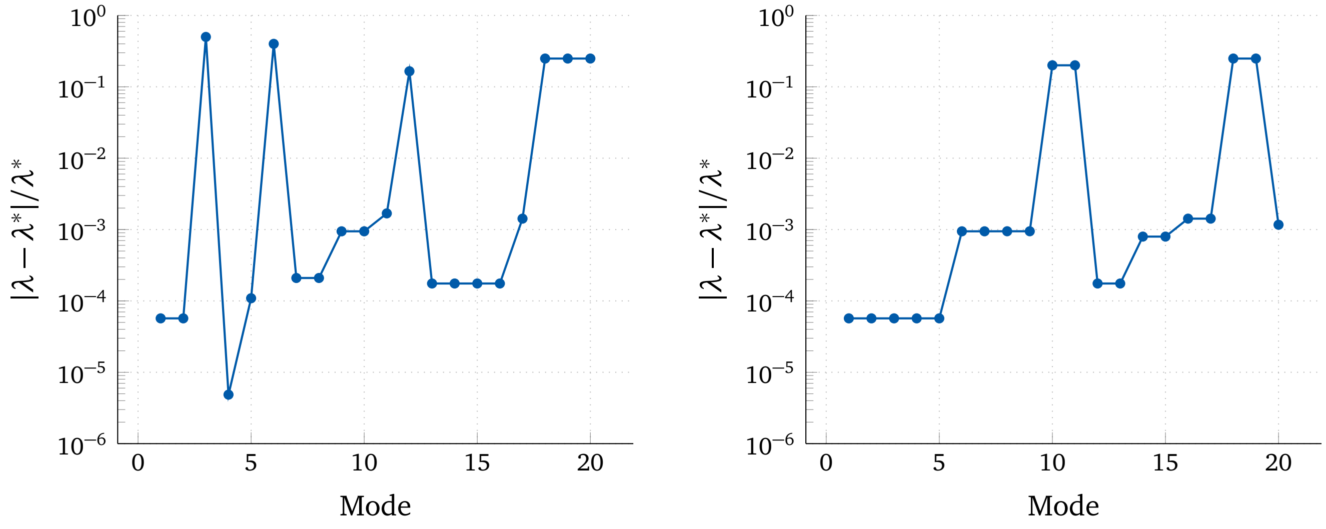

(a) Number of waveguide modes $N_\Gamma = 2$.

(b) Number of waveguide modes $N_\Gamma = 6$.

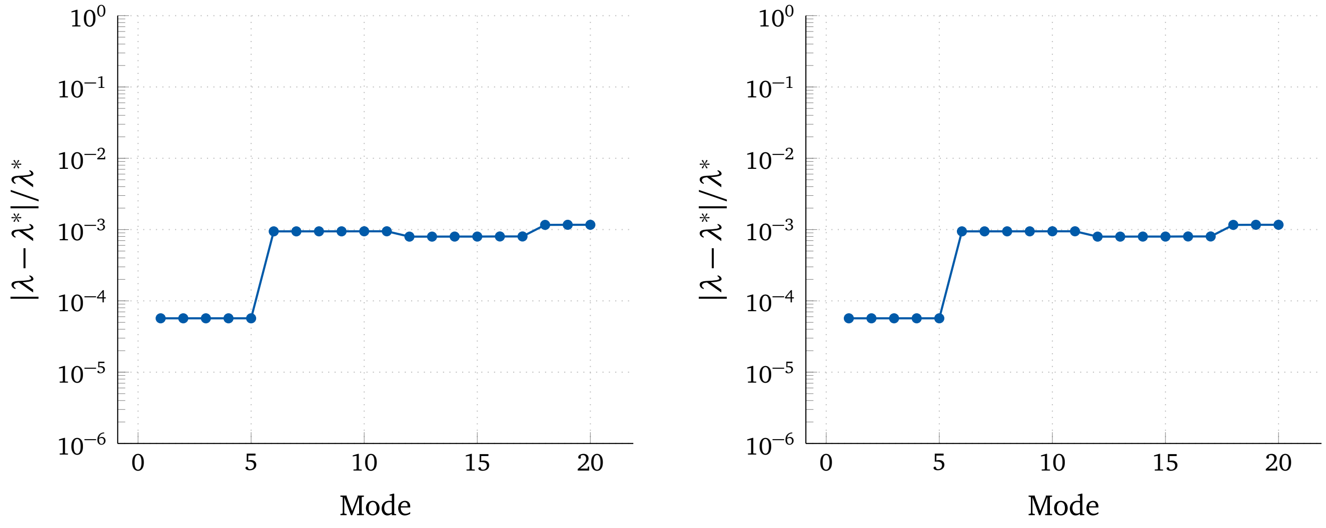

(c) Number of waveguide modes $N_\Gamma = 18$.

(d) Number of waveguide modes $N_\Gamma = 34$.

Figure 8.11: SSC coupling on a multipatch cube: convergence of the first 20 eigenvalues for a fixed discretisation on the two subdomains and an increasing number of waveguide modes N_Γ.

the spectrum as a consequence of the coupling due to non-physical charges appearing on the interface Γ. As mentioned above, these modes can be eliminated by imposing the divergence free condition (2.4b).

8.3 2-cell Coupling

Given the modularity of RF cavities, the proposed coupling methods can be used as a substructuring method to reduce the computational cost during matrix construction. As shown in Table 2.1, of the nine cells the TESLA cavity is made of, the central seven are identical, whereas the two end cells are slightly different. It is then possible to discretise the three types of cells only once and subsequently couple them together in a block-diagonal system through mortaring.

As a test case, in Fig. 8.8 we show the example of a fictitious 2-cell TESLA cavity. We solve Maxwell's eigenproblem with PEC boundary condition on the walls and PMC boundary condition on the outgoing irises. The single cell parametrisation is constructed in such a way that the left and right iris are not symmetric, in order to get non-conforming grids on the interface Γ. The cell is discretised only once to

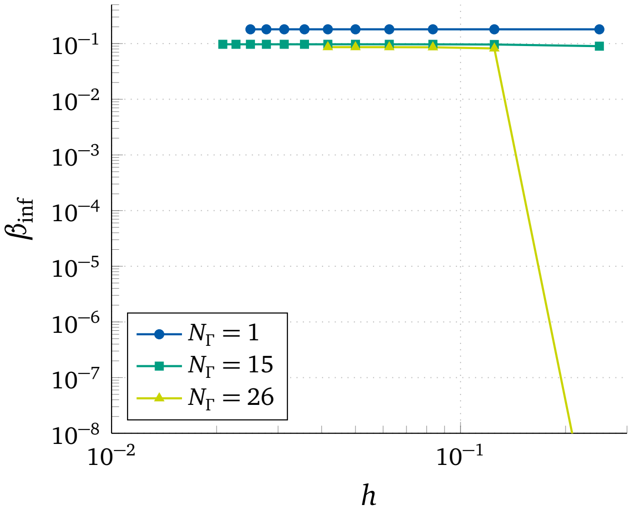

Figure 8.12: SSC coupling on a multipatch cube: β_{inf} constants for an increasing number of waveguide modes. When too many waveguide modes are chosen with respect to space discretisation, β_{inf} goes to zero.

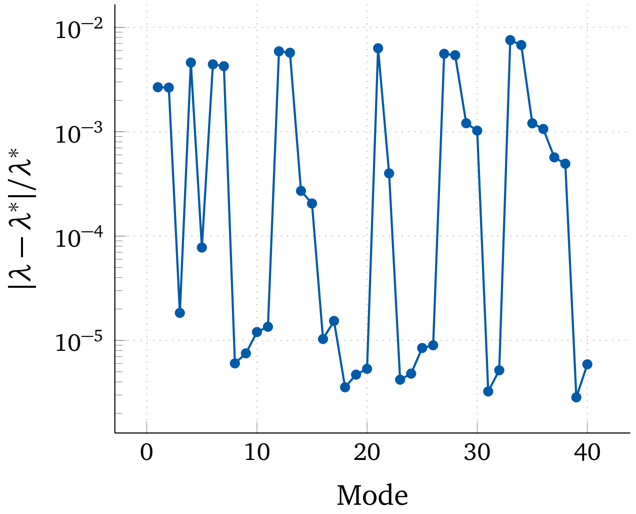

Figure 8.13: SSC coupling on a multipatch cube: spectrum approximation. On one side an IGA discretisation with $p_1 = 3$ and reglarity $r_1 = 2$ is used, while on the other side classical first order tetrahedral edge elements FEM is used.

$f_{\mathrm{exact}}[\mathrm{GHz}]$	$f\,[\mathrm{GHz}]$
	0.035 857
	0.035 857
	0.577 485
	0.584 617
	1.841 232
	1.841 232
	2.253 919
	2.254 197
2.373 958	2.373 968
2.373 958	2.373 968
2.705 705	2.704 475
2.705 705	2.704 475
2.942 116	2.942 116
3.036 078	3.036 078
3.182 680	3.182 785
3.182 680	3.182 785
	3.214 081
	3.214 081
3.301 959	3.301 962
3.702 910	3.702 994
3.749 870	3.753 896
3.749 870	3.753 896
3.811 044	3.811 201
3.811 044	3.811 263

Table 8.1: Comparison between the exact eigenfrequencies in the pill-box cavity and the ones computed using the SSC method. One subdomain is discretised using second order IGA basis functions, the other with hexahedral FEM. Some spurious modes are present in the spectrum (see Section 8.2).

obtain the curl-curl and mass matrices (respectively **K** and **M**) and the two matrices are coupled together through mortaring in order to get

$$\mathbf{K}_{\mathrm{cpld}} = \begin{bmatrix} \mathbf{K} & 0 & \mathbf{B}_1 \\ 0 & \mathbf{K} & -\mathbf{B}_2 \\ \mathbf{B}_1^{\mathrm{T}} & -\mathbf{B}_2^{\mathrm{T}} & 0 \end{bmatrix} \qquad \mathbf{M}_{\mathrm{cpld}} = \begin{bmatrix} \mathbf{M} & 0 & 0 \\ 0 & \mathbf{M} & 0 \\ 0 & 0 & 0 \end{bmatrix} \tag{8.4}$$

where $\mathbf{B}_i$ are the coupling matrices given by the coupling between the three-dimensional IGA space constructed on Ω_i and the two-dimensional space of Lagrange multipliers on the connecting interface Γ (see equation (5.17) and (5.28)).

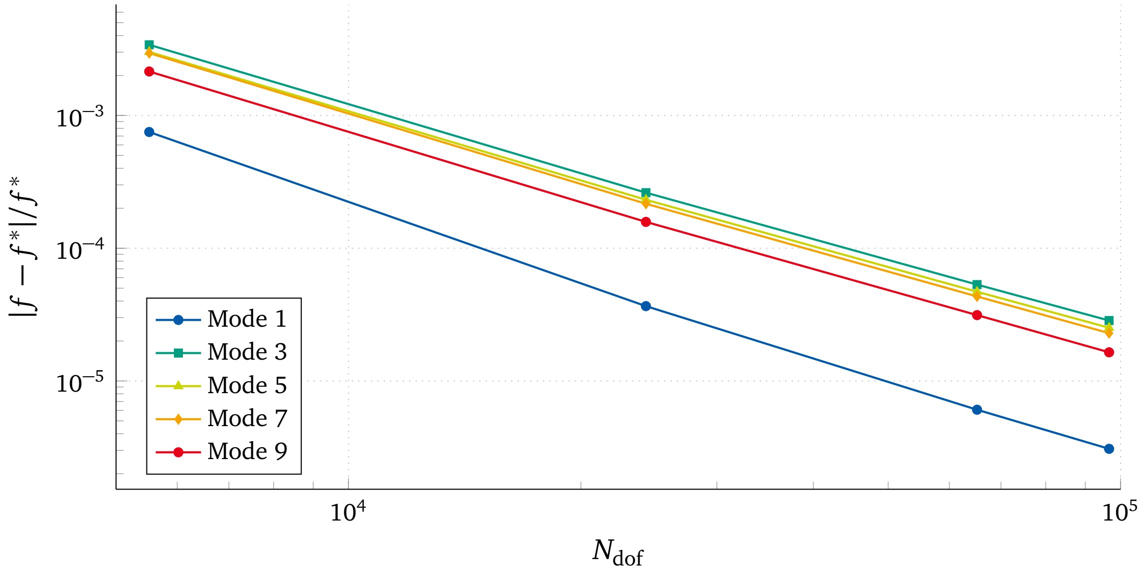

Figure 8.14: Convergence of the first five eigenmodes to a highly refined solution obtained with no substructuring.

		Mortar			**SSC** ($N_\Gamma = 25$)			**Full Discretisation**		
Ref. Lev.	N_{dof}	$t_{\text{mat}}[\text{s}]$	$t_{\text{sol}}[\text{s}]$	$t_{\text{tot}}[\text{s}]$	$t_{\text{mat}}[\text{s}]$	$t_{\text{sol}}[\text{s}]$	$t_{\text{tot}}[\text{s}]$	$t_{\text{mat}}[\text{s}]$	$t_{\text{sol}}[\text{s}]$	$t_{\text{tot}}[\text{s}]$
2	~ 5000	3.65	1.28	4.93	2.62	1.34	3.96	24.98	1.25	26.23
4	$\sim 25\,000$	20.48	10.01	30.49	17.54	9.87	27.41	90.61	7.57	98.19
6	$\sim 65\,000$	61.45	43.40	104.85	56.79	72.31	129.10	250.55	36.02	286.57

Table 8.2: Substructuring method efficiency.

In Fig. 8.14 some of the eigenvalues computed with the Mortar method for different level of mesh refinement (with $p = 2$, $r = 1$) are compared to a finer solution of the same problem obtained with no substructuring and the order of convergence is in agreement with the theory. A comparison of the efficiency of the two substructuring approaches with respect to the solution of the full problem is reported in Table 8.2. For the SSC method a fixed number of waveguide modes $N_\Gamma = 25$ is used. It can be appreciated how the modular construction of the matrices takes less than half the time than the full discretisation. The solution of the saddle-point matrices of the coupled system scales worse with respect to the complete simulation, but the overall computational time is still significantly lower.

8.4 Simulation of a full TESLA cavity

As a final example of the applicability of the two coupling methods to RF cavity simulation, we consider the TESLA cavity, including the two HOM couplers at both ends (see Fig. 5.1). We consider the cavity as if composed by 11 blocks (7 of which are identical mid cells which can be discretised only once) separated by 10 circular interfaces. The coupling between the cells is performed using Mortar. The two beampipes with the HOMC are instead triangulated and the discrete matrices are assembled using lowest order Nédélec Finite Elements through an in-house code. The coupling of the cavity with the beampipes is performed using the SSC technique since, as showed before, it is easier to construct the coupling matrices without the necessity of an intersection mesh. In Fig. 5.2 the enforced subdivision is highlighted.

As a proof of concept we apply PEC as boundary conditions at the couplers (for a real application specific port boundary conditions would need to be imposed). The results are reported in Table 8.3 where it is possible to see the presence of some spurious modes at the beginning of the spectrum.

Mode	$f\,[\mathrm{GHz}]$	Mode	$f\,[\mathrm{GHz}]$
1	0.049 932	21	1.629 433
2	0.269 500	22	1.629 452
3	0.274 693	23	1.641 527
4	0.296 580	24	1.641 594
5	0.301 146	25	1.658 129
6	0.464 058	26	1.658 379
7	0.494 598	27	1.678 763
8	0.509 495	28	1.679 235
9	0.529 445	29	1.702 588
10	1.277 173	30	1.703 258
11	1.279 250	31	1.728 442
12	1.282 478	32	1.729 246
13	1.286 496	33	1.754 965
14	1.290 818	34	1.755 841
15	1.294 900	35	1.781 015
16	1.298 226	36	1.782 023
17	1.300 387	37	1.800 734
18	1.301 132	38	1.800 779
19	1.622 122	39	1.823 147
20	1.622 139	40	1.824 116

Table 8.3: First 40 computed eigenfrequencies in the TESLA cavity including the HOMC. The simulation is performed exploiting both the Mortar and the SSC substructuring methods. Some spurious modes appear at the beginning of the spectrum (see Section 8.2).

8.5 Model Order Reduction

As mentioned in chapter 5.4, the original SSC method combined the Input/Output formulation with MOR techniques to reduce the computational effort of simulating long cavity chains [48]. The idea is to construct a reduced basis for each subdomains such that

$$\mathbf{K} = \begin{bmatrix} \mathbf{V}_1^\top \mathbf{K}_1 \mathbf{V}_1 & 0 \\ 0 & \mathbf{V}_2^\top \mathbf{K}_2 \mathbf{V}_2 \end{bmatrix} \qquad \mathbf{M} = \begin{bmatrix} \mathbf{V}_1^\top \mathbf{M}_1 \mathbf{V}_1 & 0 \\ 0 & \mathbf{V}_2^\top \mathbf{M}_2 \mathbf{V}_2 \end{bmatrix} \qquad \mathbf{B} = \begin{bmatrix} \mathbf{V}_1^\top \mathbf{B}_1 \\ -\mathbf{V}_2^\top \mathbf{B}_2 \end{bmatrix} \tag{8.5}$$

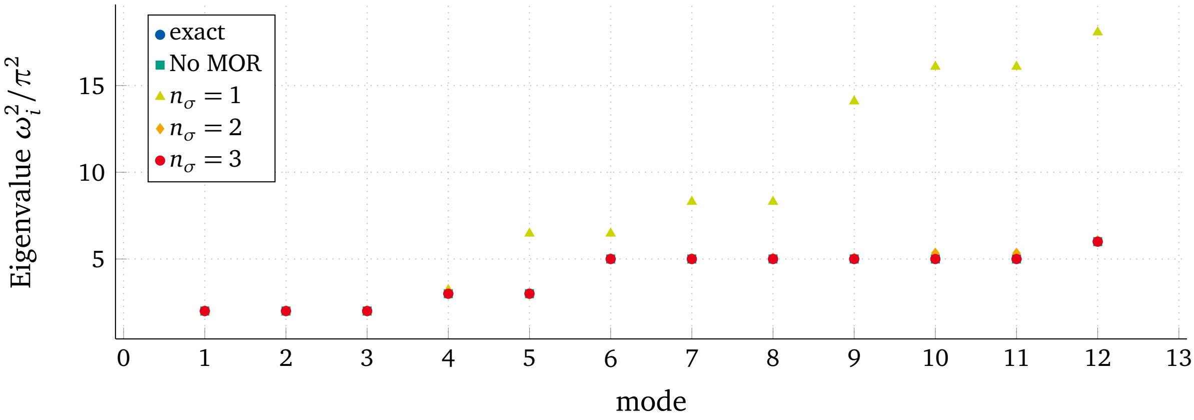

Figure 8.15: SSC coupling on a multipatch cube using Model Order Reduction (MOR): approximation of the first 12 modes for an increasing number of eigenvalue samples n_σ.

where $\mathbf{V}_s \in \mathbb{R}^{N_{\mathrm{dof}} \times n}$, with $n \ll N_{\mathrm{dof}}$.

We favour a multipoint reduced basis approach where, given a guess on the eigenvalues σ_i $(i = 1, ..., n_\sigma)$, we solve for $\mathbf{X}_{s,i}$ each linear equations system

$$\big(\mathbf{K}_s - \sigma_i \mathbf{M}_s\big)\mathbf{X}_{s,i} = \mathbf{B}_s, \tag{8.6}$$

in order to obtain a matrix $\mathbf{C}_s = [\mathbf{C}_{s,1}, \dots, \mathbf{C}_{s,i-1}, \mathbf{C}_{s,i}]$. To obtain a reduced orthonormal basis it is possible to compute the transformation matrices $\mathbf{V}_s$ in (8.5) as the collection of the left eigenvectors of $\mathbf{C}_s$ through, e.g., an SVD decomposition.

We test the proposed method in the case of the cubic geometry in Fig. 8.1 in the case of non-matching discretisation on the interface Γ and a fixed amount of analytical waveguide modes ($N_\Gamma = 18$). For this test we exploit the a-priori knowledge on the exact eigenvalues and choose $\sigma_1 = 2\pi^2$, $\sigma_2 = 3\pi^2$, $\sigma_3 = 5\pi^2$. In Fig. 8.15 the spectrum approximation is shown for an increasing number of chosen samples $n_\sigma = 1, 2, 3$. From a complete system of 6148 degrees of freedom, the MOR reduces significantly the system dimension to 54, 90 and 126 degrees of freedom respectively.

The application of this MOR method to more complicated geometries and problems where the exact eigenvalues are unknown is underway.

9 Shape Optimization of a Stern-Gerlach Magnet

If you have a Stern-Gerlach device,
you would like the B field to be nice.
If the gradient is strong
you can never be wrong,
and the measure will be more precise.

We now consider a different type of application, where the purpose of the electromagnetic field is not the acceleration of the particles, but their separation into different trajectories. In particular we are interested in the simulation and shape optimisation of the so called Stern-Gerlach magnet, which is an experimental setup used to prove and measure the quantisation of the angular momentum of atoms [86]. A Stern-Gerlach magnet operates by generating a magnetic field with a strong spatial gradient in one direction. The magnetic field causes a precession of the magnetic dipoles whereas its gradient invokes a deflection of the particles. In order to obtain a sufficiently large deflection, this magnetic field gradient needs to be both large and homogeneous in the area between the magnet poles.

The structure of this chapter is as follows. First we give an introduction to the model used for this application and motivate the choice of IGA for the discretisation. Then we introduce the quantities of interest in the beam area that are the target of optimisation and finally we present the results of the optimisation scheme.

9.1 Model for the Stern-Gerlach Magnet

We consider a magnet that is already in operation at KU Leuven in Belgium, which uses a Rabi type design of the pole-shoe shapes [69] (see Fig. 9.1). The design requirements for the field are a field gradient in the x-direction greater than $200\,\mathrm{T\,m^{-1}}$ and a field inhomogeneity of maximum $5\,\%$. Both objectives were achieved, however there is interest in further improvements for future upgrades.

To reduce the computational costs, the optimisation is carried out using a linearised 2D model of the magnet's cross section. Furthermore only the pole region is spatially discretised, while the coils and the yoke are substituted by a magnetic equivalent circuit. For a more in depth discussion on the modelling we refer to [79]. To further speed up the computation, the non-linear saturation is frozen, i.e., a constant but

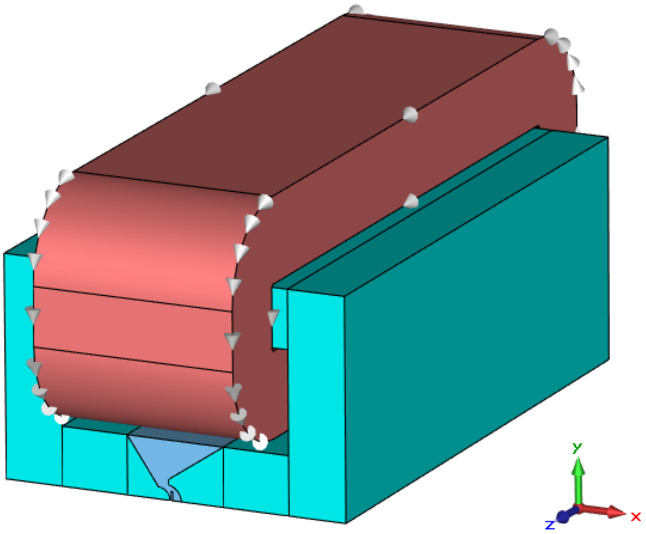

Figure 9.1: 3D model of one half of the Stern-Gerlach magnet (modelled with CST EMS®).

inhomogeneous permeability $\mu = \mu(\mathbf{B}^0)$ is used where $\mathbf{B}^0$ is evaluated as a post-processing step from a non-linear computation of the full model.

In the pole region we solve magnetostatic problem (2.12), which can be further simplified given the 2D assumption to get

$$\Delta A_z^* = -\mu J_z, \tag{9.1}$$

with A_z^* and J_z the longitudinal components of the magnetic vector potential and of the applied current density respectively. At the boundary we impose a Robin type boundary conditions given by the magnetic equivalent circuit [79].

The application of an Isogeometric approach allows for the description of the poles' shape with a small number of control points, which reduces the number of optimisation parameters while, at the same time, maintaining a certain freedom in the shape. Moreover, the global geometry mapping of IGA alleviates the burden of mesh transformation or remeshing in each step of the process. Finally, given the higher smoothness across element boundaries that is achievable using B-Spline and NURBS basis functions, we expect the evaluation of the magnetic field gradient to be more accurate.

9.2 Optimisation of the Pole Shape

Using GeoPDEs [94], the geometry of the pole tips is constructed utilising three patches, one for the gap region and two for the left and right pole respectively. The boundary control points responsible for the shape of the pole tips are then used as variables for the optimisation procedure (see Fig. 9.2). The internal parametrisation has been optimised using the Winslow functional [56], and follows automatically the deformations of the boundary such that no remeshing or further mesh transformation is necessary.

To define the objective function for the optimisation we introduce the magnetic field gradient in the x direction $\tau = \mathrm{d}|\mathbf{B}|/\mathrm{d}x$ which can be evaluated from the solution for A_z^* by post-processing. The average magnetic field gradient in the beam area Ω_{beam} is

$$\tau_{\text{av}} = \frac{1}{|\Omega_{\text{beam}}|} \int_{\Omega_{\text{beam}}} \tau(x,y)\, \mathrm{d}\Omega, \tag{9.2}$$

and the inhomogeneity of the magnetic field gradient is given by

$$\epsilon = \sqrt{\frac{1}{|\Omega_{\text{beam}}|} \int_{\Omega_{\text{beam}}} \left(\frac{\tau(x,y)}{\tau_{\text{av}}} - 1 \right)^2 \mathrm{d}\Omega}. \tag{9.3}$$

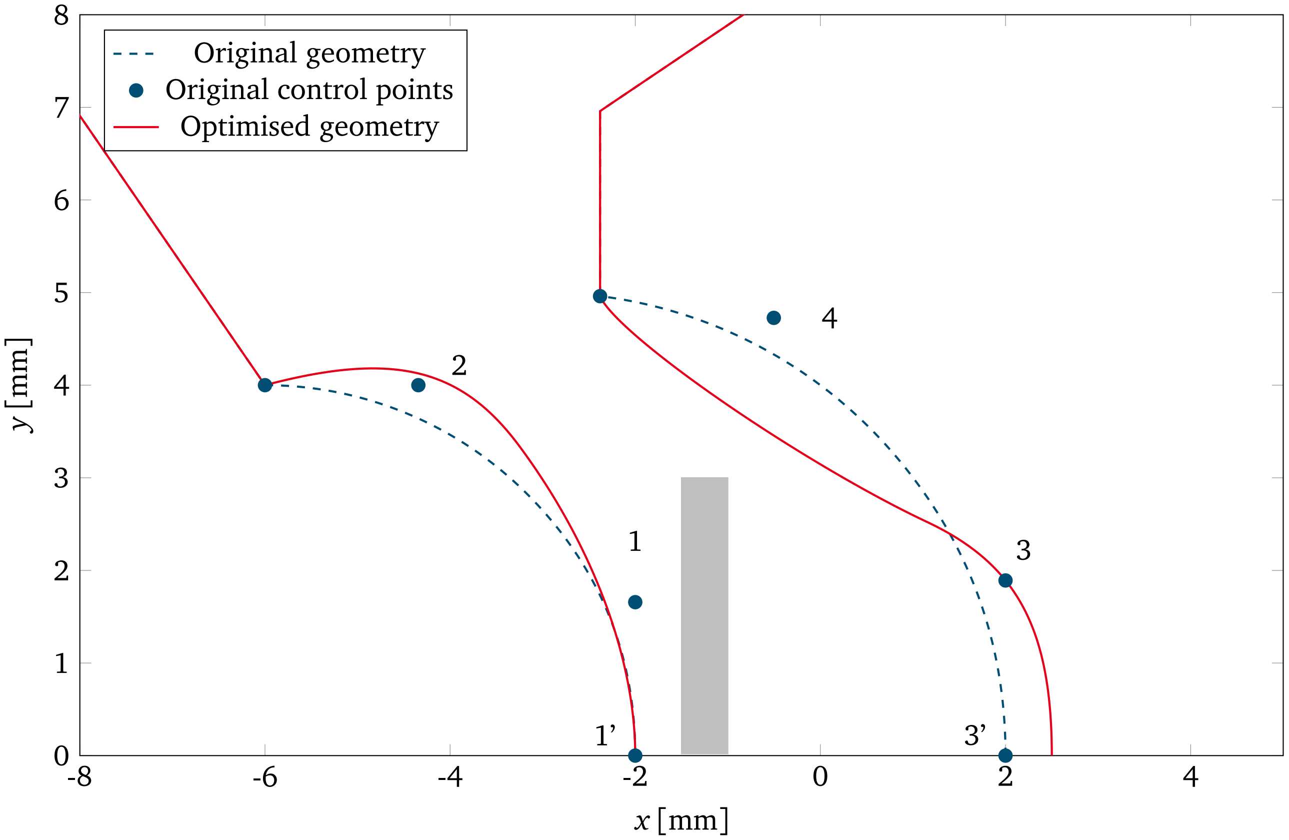

Figure 9.2: Design geometry (in blue) and optimised geometry (in red) of the pole tips. In grey the beam area is highlighted.

The objective function for the optimisation is chosen in such a way that both the requirement for a high average magnetic field gradient $\tau_{\mathrm{av}} = \tau_{\mathrm{av}}(\mathbf{x}, \mathbf{y}, \mathbf{w})$ and a low inhomogeneity factor $\epsilon = \epsilon(\mathbf{x}, \mathbf{y}, \mathbf{w})$, where we denote with $\mathbf{x} = \{x_i\}$, $\mathbf{y} = \{y_i\}$ and $\mathbf{w} = \{w_i\}$ the vectors of geometrical degrees of freedom (x-coordinates, y-coordinates, weights) of the control points that generate the pole shapes (see Fig. 9.2). The objective function to be minimised is

$$J_{\mathrm{obj}} = \frac{\tau_{\mathrm{w}}}{|\tau_{\mathrm{av}}|} + \epsilon - \frac{\tau_{\mathrm{w}}}{|\tau_{\mathrm{av}}|}\epsilon, \tag{9.4}$$

where τ_{w} is a weight which is set to $8\,\mathrm{T\,m^{-1}}$ in such a way that the average magnetic field gradient is as high as possible without however compromising its homogeneity [79]. The constraints on the control points are

$$\begin{aligned}
&x_1 \in [-3; -2]\,\mathrm{mm}, && y_1 \in [1.66; 2]\,\mathrm{mm}, && w_1 = 0.85\\
&x_2 \in [-5; -2]\,\mathrm{mm}, && y_2 \in [2.5; 4.5]\,\mathrm{mm}, && w_2 \in [0.35; 2.85]\\
&x_3 \in [1.5; 2.5]\,\mathrm{mm}, && y_3 \in [1.89; 2.5]\,\mathrm{mm}, && w_3 = 0.87\\
&x_4 \in [-2; 2]\,\mathrm{mm}, && y_4 \in [4; 5.5]\,\mathrm{mm}, && w_4 \in [0.37; 2.87].
\end{aligned}$$

Moreover, in order to guarantee perpendicularity at the symmetry plane of the magnet, the lowermost control points 1' and 3' (see Fig. 9.2) of the pole tips are coupled in x-direction to the control points 1 and 3 above them.

For the optimisation a hierarchical approach is chosen: first, starting from the design geometry, the pattern search algorithm `GPSPositiveBasis2N` from Matlab's optimisation Toolbox [70] is used. Being a

	GeoPDEs (2D)			CST® 3D		
	Ω_{start}	Ω_{opt}	Improvement	Ω_{start}	Ω_{opt}	Improvement
τ_{av}	$-240\,\mathrm{T\,m^{-1}}$	$-282\,\mathrm{T\,m^{-1}}$	12.2 %	$-237\,\mathrm{T\,m^{-1}}$	$-266\,\mathrm{T\,m^{-1}}$	17.5 %
ϵ	0.0477	0.0122	74.4 %	0.0503	0.0201	60.0 %

Table 9.1: Stern-Gerlach magnet optimisation results for the average magnetic field gradient τ_{av} and the inhomogeneity ϵ.

global method, the convergence is ensured regardless of the starting point. In a second step, a gradient based optimisation scheme is used. To ensure smooth representations of the magnetic field gradients, which require the computation of two derivatives of the solution A_z^*, the order of the basis functions for the approximation space is set to 5.

The optimised geometry is depicted in Fig. 9.2. The control points and the weights for the new pole tips configuration are given by

$$
\begin{aligned}
x_1 &= -2.00\,\text{mm}, & y_1 &= 1.66\,\text{mm}, & w_1 &= 0.85,\\
x_2 &= -4.11\,\text{mm}, & y_2 &= 4.50\,\text{mm}, & w_2 &= 1.25,\\
x_3 &= 2.50\,\text{mm}, & y_3 &= 1.90\,\text{mm}, & w_3 &= 0.87,\\
x_4 &= -2.00\,\text{mm}, & y_4 &= 4.00\,\text{mm}, & w_4 &= 0.37.
\end{aligned}
$$

The results for the average magnetic field gradient and for the homogeneity are verified through conventional 3D FEM simulations in CST EM STUDIO (CST EMS®). Table 9.1 shows the two values before and after optimisation computed with GeoPDEs and CST EMS®. The discrepancies are to be attributed to the 2D approximation and to the frozen saturation in the IGA code. However, both show a significative improvement.

The magnetic field gradient τ computed from the 3D FEM simulation are shown in Fig. 9.3c for the starting and the optimised geometry. In Fig. 9.3f the analogous results are shown for the IGA simulation. It is worth noticing that the magnetic field gradient from the GeoPDEs simulation exhibits a higher smoothness thanks to the use of high order B-Spline functions. Both figures show that the average gradient reaches a higher absolute value and has a flatter behaviour. The different results for the GeoPDEs simulation and the CST® one are to be attributed to the border effects of the full 3D simulation and to the fact that the particular model adopted with the field circuit coupling considers the material to be frozen and discards the non-linearity.

The overall gain in performance is however significant with an average magnetic gradient 17.5 % higher and an inhomogeneity approximately 60.0 % lower.

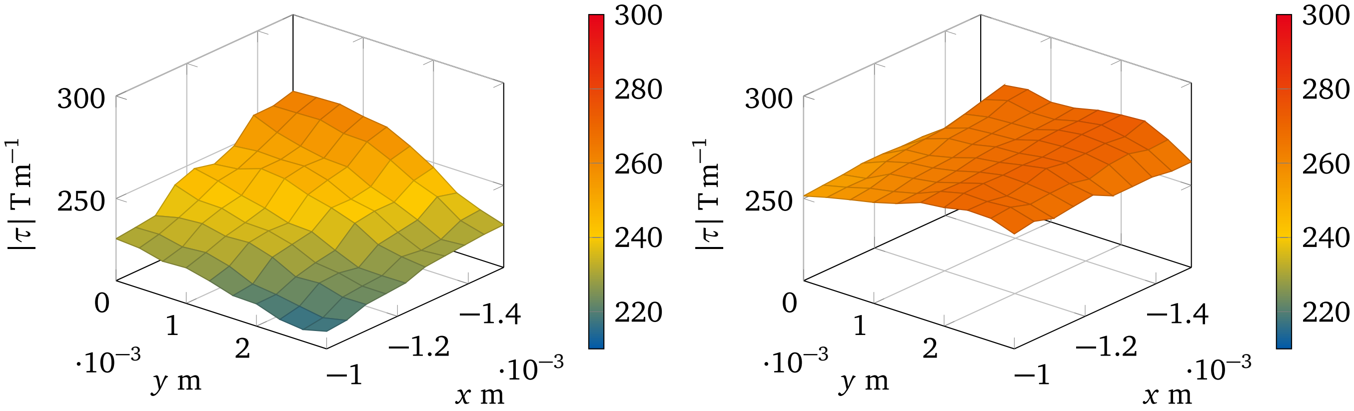

(a) Starting geometry

(b) Optimised geometry

(c) Comparison of the gradient τ in the air gap before and after the optimisation with a 3D FEM simulation using CST EMS®.

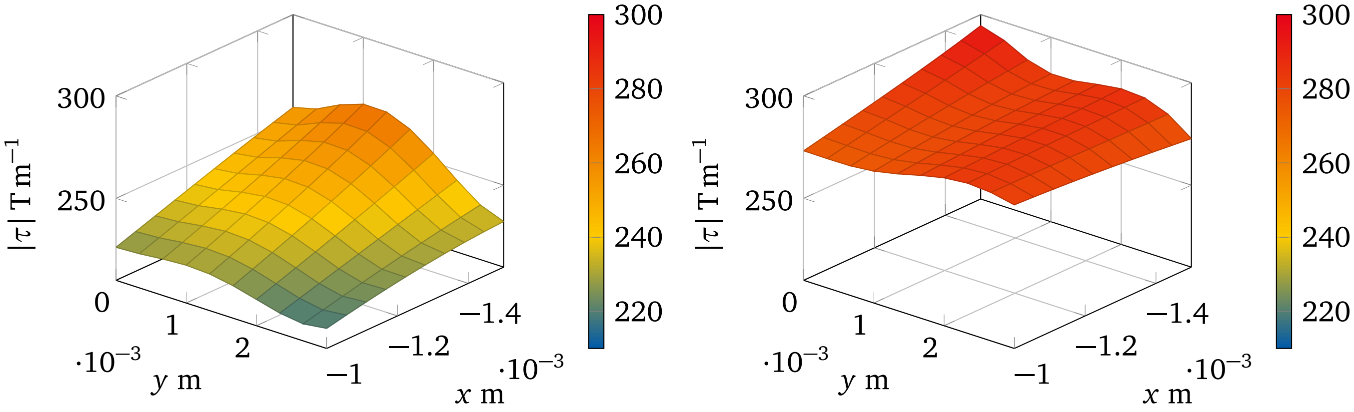

(d) Starting geometry

(e) Optimised geometry

(f) Comparison of the gradient τ in the air gap before and after the optimisation with a 2D IGA simulation using GeoPDEs.

10 Conclusions and Perspectives

Now the time has come for the end,
you're almost done reading, my friend.
A summary of the text,
a word on what's next.
All is left is for me to defend!

In this work the applicability of IGA to the simulation of real world electromagnetic devices has been addressed. Particular attention was given to those devices whose performance is mainly or significantly determined by their geometry such as particle accelerator RF cavities or separation magnets. By exploiting the properties of B-Spline and NURBS basis functions, the IGA discretisation allows for the exact parametrisation of the computational domains and for the construction of approximation spaces that guarantee a higher regularity of the solutions fields with respect to traditional FEM approaches.

The inherent properties of the Isogeometric method allow for the accurate description of small geometry deformations through a comparatively small number of control points. This proved to be beneficial both when dealing with the coupled electromagnetic-mechanical problem used for the evaluation of Lorentz detuning in TESLA cavities and for shape optimisation procedures. The boundary deformation, in particular, naturally extends in the interior of the domain, without the need for a remeshing step which would introduce undesired noise on the solution.

Given the high sensitivity of these type of devices to geometrical changes, UQ methods based on stochastic collocation were applied. NURBS basis functions proved to be particularly useful for the creation of uncorrelated deformation modes arising from discrete Karhunen–Loève decomposition and for the deformation of the geometry according to those modes. Given the possibility of eigenvalue crossings in the parameter space, an eigenvalue tracking method was proposed based on the definition of a homotopy between the points in the parameter space. The method gave very good results even in the presence of degenerate modes splitting.

Finally, two substructuring methods based on domain decomposition approaches were introduced. One is a Mortar method that exploits the properties of IGA spaces to easily define the trace spaces on the connecting interfaces and the space of Lagrange multipliers. For this method a stability result is given. The second one is based on the coupling of Input/Output system through the definition of an analytical basis as the Lagrange multipliers space. Both methods are cast within the common framework of the three-field method. The combination of the two approaches allowed for the simulation of the TESLA cavities by coupling an Isogeometric discretisation in the cavity cells with a classical FEM in the couplers.

Several interesting and important aspects, however, could not be covered in this thesis. In operation each cavity goes through a tuning process that aims at getting a high field flatness and perfect tuning of the frequency of the accelerating mode. When applying UQ to evaluate the shape sensitivities, in order to get more realistic results, the tuning should be applied to each deformed configuration in the parameter space. A complete shape optimisation for each of the collocation points is clearly unfeasible, but a simplified model (similar to what is done for the real cavities) could be used.

Another interesting topic for the accelerator facilities is the study of an inverse problem where, given the field and frequency changes with respect to the expected behaviour, one wants to obtain the geometry deformations that generated it. The proper mathematical formulation of such a problem is complicated since it is not even clear if the solution would be unique. A first step in this direction is currently under consideration in the context of the Deutsche Forschungsgemeinschaft (DFG) network *Uncertainty quantification techniques and stochastic models for superconducting radio frequency cavities*.

Another promising research direction is related to the substructuring methods. A mathematical proof for the SSC saddle-point stability is currently under study. Moreover, the application of model order reduction on each block, that was proposed in the original SSC method, deserve further investigation both in terms of the choice of the reduced basis and in terms of stability.

Finally, a research project is currently under way at TU Darmstadt on the applicability to RF cavity simulation of IGA in conjunction with Boundary Element Method (BEM).

To conclude, we care to mention that IGA interesting properties could be exploited for other types of electromagnetic devices. At the present time, e.g., the application of IGA to electrical machines simulation is under study [10].

Acronyms and Abbreviations

BEM	Boundary Element Method
BOBYQA	Bounded Optimisation BY Quadratic Approximation
B-Rep	Boundary Representation
BVP	Boundary Value Problem
CAD	Computer Aided Design
CSC	Coupled S-Parameter Calculation
CST®	Computer Simulation Technology
CST EMS®	CST EM STUDIO
CST MPS®	CST MPHYSICS STUDIO
CST MWS®	CST MICROWAVE STUDIO
DDM	Domain Decomposition Method
DESY	Deutsches Elektronen-Synchrotron
EBW	Electron Beam Welding
FE	Finite Element
FEL	Free-Electron Laser
FEM	Finite Element Method
FLASH	Free-electron LASer in Hamburg
gPC	generalised Polynomial Chaos
HOM	Higher Order Mode
HOMC	Higher Order Mode Coupler
IGA	Isogeometric Analysis
i.i.d.	independent and identically distributed
IRLM	Implicitly Restarted Lanczos Method
LHC	Large Hadron Collider
LINAC	LINear ACcelerator
MC	Monte Carlo
MOR	Model Order Reduction
NURBS	Non-Uniform Rational B-Splines
PCA	Principal Component Analysis
PDE	Partial Differential Equation
PEC	Perfect Electric Conducting
PMC	Perfect Magnetic Conducting

RF	Radio Frequency
ROM	Reduced Order Model
S-DALINAC	Superconducting-DArmstadt-LINear-ACcelerator
SIBC	Surface Impedance Boundary Condition
SQP	Sequential Quadratic Programming
SSC	State Space Concatenation
SVD	Singular Value Decomposition
TE	Transverse Electric
TEM	Transverse Electric and Magnetic
TESLA	TeV-Energy Superconducting Linear Accelerator
TM	Transverse Magnetic
TTF	TESLA Test Facility
UQ	Uncertainty Quantification

Symbols and Notation

Spaces

Symbol	Description
C^0	space of continuous functions
C^p	space of continuous functions with p continuous derivatives
$H^1(\Omega)$	Sobolev space of functions with integrable gradient
$\mathbf{H}(\mathbf{curl};\Omega)$	Sobolev space of functions with curl in $L^2(\Omega)$
$\mathbf{H}_0(\mathbf{curl};\Omega)$	Sobolev space of $\mathbf{H}(\mathbf{curl};\Omega)$ functions with vanishing trace
$\mathbf{H}_{0,\Gamma_D}(\mathbf{curl};\Omega)$	Sobolev space of $\mathbf{H}(\mathbf{curl};\Omega)$ functions with vanishing trace on Γ_D
$\mathbf{H}(\mathrm{div};\Omega)$	Sobolev space of functions with divergence in $L^2(\Omega)$
$\mathbf{H}_0(\mathrm{div};\Omega)$	Sobolev space of $\mathbf{H}(\mathrm{div};\Omega)$ functions with vanishing trace
$H^k(\Omega)$	Sobolev space of functions in $L^2(\Omega)$ with k-th order derivatives in $L^2(\Omega)$
$\mathbf{H}^k(\Omega)$	Sobolev space of functions in $\mathbf{L}^2(\Omega)$ with k-th order derivatives in $\mathbf{L}^2(\Omega)$
$H^{-1/2}(\mathrm{div}_\Gamma;\Gamma)$	trace space of $\mathbf{H}(\mathbf{curl};\Omega)$ on Γ
$\mathbf{H}\left(\mathrm{div}^0;\Omega\right)$	Sobolev space of integrable functions with zero divergence
$L^2(\Omega)$	Lebesgue space of square integrable scalar functions
$\mathbf{L}^2(\Omega)$	Lebesgue space of square integrable vectorial functions
Λ_δ^s	space of Mortar Lagrange multipliers
$L^p(\Omega)$	Lebesgue space of order p (scalar functions)
$\mathbf{L}^p(\Omega)$	Lebesgue space of order p (vectorial functions)
S^0	$H^1(\Omega)$ conforming B-Spline approximation space
S^1	$\mathbf{H}(\mathbf{curl};\Omega)$ conforming B-Spline approximation space
S^2	$\mathbf{H}(\mathrm{div};\Omega)$ conforming B-Spline approximation space
S^3	$L^2(\Omega)$ conforming B-Spline approximation space
$S_{\boldsymbol{\alpha}}^p$	one dimensional B-Spline space of degree p and regularity $\boldsymbol{\alpha}$
$S_{\boldsymbol{\alpha}_1,\boldsymbol{\alpha}_2,\boldsymbol{\alpha}_3}^{\mathbf{p}}$	tensor product B-Spline space of degrees $\mathbf{p}$ and regularity $\boldsymbol{\alpha}_d$ along each direction
V	infinite dimensional space
V_δ	global approximations space for the Mortar method
V_δ^c	global approximations space for the Mortar method with tangential (weak) continuity
V_δ^s	restriction of V_δ to subdomain s
V_h	finite dimensional subspace approximating V
V_h^s	curl-conforming finite dimensional space on subdomain s
W	$H^1(\Omega)$ conforming NURBS approximation space

Physical Quantities

Symbol	Units	Description
α_i	V	modal voltages
$\mathbf{B}$	T	magnetic induction

Symbol	Units	Description
β_i	A	modal currents
c	m/s	speed of light
$\mathbf{D}$	C/m^2	electric displacement
$\mathbf{E}$	V/m	electric field
$\mathbf{e}$	V/m	degrees of freedom for the electric field
E_{acc}	MV/m	accelerating gradient of a RF cavity
$\mathbf{E}_h$	V/m	discretised electric field
$\underline{\mathbf{E}}$	V/m	electric field phasor
ε_0	F/m	electric permittivity of vacuum
ε	F/m	electric permittivity
η	GPa	second Lamé parameter (shear modulus)
f	Hz	frequency
$\mathbf{H}$	A/m	magnetic field
$\underline{\mathbf{H}}$	A/m	magnetic field phasor
$\mathbf{J}$	A/m^2	electric current density
$\underline{\mathbf{J}}$	A/m^2	electric current density phasor
$\mathbf{J}_s$	A/m^2	applied electric current density
k	1/m	wave number
κ	GPa	first Lamé parameter (elastic modulus)
μ	H/m	magnetic permeability
μ_0	H/m	magnetic permeability of vacuum
P_c	W	power loss in a RF cavity
$\mathbf{r}$	m	position vector
R_a	Ω	shunt impedance of a RF cavity
ρ	C/m^3	electric charge induction
$\underline{\rho}$	C/m^3	electric charge induction phasor
σ	S/m	electric conductivity
$\boldsymbol{\sigma}$	GPa	Cauchy stress tensor
t	s	time
U	J	stored energy
$\mathbf{u}$	m	displacement
V_c	V	longitudinal voltage in a RF cavity
ω	rad/s	angular frequency
ω_h	rad/s	computed angular frequency

Other Symbols

Symbol	Units	Description
$\boldsymbol{\alpha}_i$		vector of regularities at each knot
$\mathrm{J}_m(\cdot)$		Bessel function of first kind of order m
$\mathrm{J}'_m(\cdot)$		derivative of the Bessel function of first kind of order m
χ'_{mn}		n-th zero of the derivative of the Bessel function of first kind of order m
χ_{mn}		n-th zero of Bessel function of first kind of order m
β		velocity relative to the speed of light
β_{inf}		inf-sup stability constant
B_i^p		i-th B-Spline basis function of degree p

Symbol	Units	Description
$\mathbf{C}$		B-Spline or NURBS curve
$\mathbf{c}$		normalisation vector
$\cdot^*$		complex conjugate operator
cov		covariance
$\nabla\times$	1/m	curl operator
d_i		eigenvalues of the covariance matrix
$\nabla\cdot$	1/m	divergence operator
$\mathbf{D}$		eigenvalue matrix (section 4.2)
$\mathbf{D}_\mathrm{t}$		truncated eigenvalue matrix (section 4.2)
$\mathbb{E}$		expected value
$\boldsymbol{\epsilon}$		white noise vector
$\boldsymbol{\epsilon}_\mathrm{t}$		truncated white noise vector
$\mathbf{e}_r$		unit vector along the radial direction
$\mathbf{e}_\theta$		unit vector along the azimuthal direction
$\mathbf{e}_x$		unit vector along the x direction
$\mathbf{e}_y$		unit vector along the y direction
$\mathbf{e}_z$		unit vector along the z direction
$\mathbf{F}$		B-Spline or NURBS parametrisation
$D\mathbf{F}$		Jacobian of the B-Spline or NURBS parametrisation
$\mathbf{F}_s$		B-Spline or NURBS parametrisation for subdomain s
Γ		surface
Γ_D		boundary with Dirichlet boundary condition
Γ_N		boundary with Neumann boundary condition
$\gamma_\mathbf{n}$		trace operator for the $\mathbf{H}(\mathrm{div};\cdot)$ space
γ_t		tangential trace operator for the $\mathbf{H}(\mathbf{curl};\cdot)$ space
Γ_wg		waveguide section
∇	1/m	gradient operator
$\nabla_\perp$	1/m	transverse gradient operator
$\imath$		imaginary unit
ι_0		gradient preserving pull-back function
ι_1		curl preserving pull-back function
ι_2		divergence preserving pull-back function
ι_3		integral preserving pull-back function
$\mathbf{K}$		curl-curl matrix
Δ	$1/\mathrm{m}^2$	Laplace operator
$\Delta_\perp$	$1/\mathrm{m}^2$	transverse Laplace operator
$\mathbf{M}$		mass matrix
m		azimuthal index for the classification of the eigenmodes
$\boldsymbol{\mu}$		vector of expected values
n		azimuthal index for the classification of the eigenmodes
N_dof		number of degrees of freedom
N_i^p		i-th NURBS basis function of degree p
N_mp		number of patches
P		probability measure
p		azimuthal index for the classification of the eigenmodes
$\mathbf{P}_i$		i-th control point
$\boldsymbol{\Phi}$		superposition of waveguide modes
$\boldsymbol{\varphi}$		waveguide modes

Symbol	Units	Description
$\mathbf{p}$		vector of degrees along each direction of B-Spline basis functions
$\mathcal{Q}$		quantity of interest
Q_0		quality factor
$\mathbb{R}^3$		space of real numbers in three dimensions
r		radial polar coordinate
$\mathbb{R}^d$		space of real numbers in d dimensions
$\mathscr{R}\{\cdot\}$		real part operator
r_i		i-th knot multiplicity
$\frac{R_a}{Q_0}$		R over Q
s		homotopy parameter
$\cdot$		scalar product
$(\cdot,\cdot)$		L^2 scalar product
$\mathbf{\Sigma}$		covariance matrix
std		standard deviation
$\mathbf{T}$		matrix of observations
$\mathbf{\Theta}$		sample space
θ		angular polar coordinate
$\tilde{\cdot}$		first order Taylor approximation
$\mathbf{V}$		B-Spline or NURBS volume
σ^2		variance
$\|\cdot\|_{L^p(\Omega)}$		L^p norm
$\mathbf{V}_\mathrm{t}$		truncated orthonormal right eigenvectors matrix
w_i		i-th NURBS basis function weight
Ξ		knot vector
ξ_i		i-th knot
Y		random parameter
$\tilde{\mathbf{y}}$		Karhunen–Loève expansion
$\tilde{\mathbf{y}}_\mathrm{t}$		truncated Karhunen–Loève expansion
$\mathbf{Y}$		vector of random parameters
$\mathbf{y}$		vector of realisations
Ω		Lipschitz polyhedral domain
$\partial\Omega$		boundary of Ω
$\mathbf{Z}_\mathrm{KL}$		Karhunen–Loève decomposition matrix
$\mathbf{Z}_\mathrm{tKL}$		truncated Karhunen–Loève decomposition matrix
Ω_s		s-th subdomain
$\hat{\cdot}$		reference domain quantity
$\underline{\cdot}$		time harmonic quantity

Bibliography

[1] C Antoine, M Foley and N Dhanaraj. *Physical Properties of Niobium and Specifications for Fabrication of Superconducting Cavities*. Tech. rep. Fermi National Accelerator Laboratory (FNAL), Batavia, IL, 2011.

[2] B. Aune et al. «Superconducting TESLA cavities». In: *Physical Review Special Topics-Accelerators and Beams* 3.9 (2000), p. 092001.

[3] F Auricchio et al. «A fully "locking-free" isogeometric approach for plane linear elasticity problems: A stream function formulation». In: *Computer Methods in Applied Mechanics and Engineering* 197.1–4 (2007), pp. 160–172.

[4] Andrea Bartezzaghi, Luca Dedè and Alfio Quarteroni. «Isogeometric Analysis of high order Partial Differential Equations on surfaces». In: *Computer Methods in Applied Mechanics and Engineering* 295 (2015), pp. 446–469.

[5] Volker Barthelmann, Erich Novak and Klaus Ritter. «High dimensional polynomial interpolation on sparse grids». In: *Advances in Computational Mathematics* 12.4 (2000), pp. 273–288.

[6] Yuri Bazilevs et al. «Isogeometric fluid-structure interaction: theory, algorithms, and computations». In: *Computational mechanics* 43.1 (2008), pp. 3–37.

[7] Lourenco Beirão da Veiga, D. Cho and Giancarlo Sangalli. «Anisotropic NURBS approximation in isogeometric analysis». In: *Computer Methods in Applied Mechanics and Engineering* 209–212 (2012), pp. 1–11.

[8] F Ben Belgacem, Annalisa Buffa and Yvon Maday. «The mortar finite element method for 3D Maxwell equations: first results». In: *SIAM Journal on Numerical Analysis* 39.3 (2001), pp. 880–901.

[9] Michele Benzi, Gene H. Golub and Jörg Liesen. «Numerical solution of saddle point problems». In: *Acta Numerica* 14.1 (2005), pp. 1–137.

[10] Prithvi Bhat. «Isogeometric Analysis of a Permanent Magnet Synchronous Machine». MA thesis. Darmstadt: Technische Universität Darmstadt, May 2017.

[11] Daniele Boffi. «Finite element approximation of eigenvalue problems». In: *Acta Numerica* 19 (May 2010), pp. 1–120.

[12] Carl de Boor. *A Practical Guide to Splines*. rev. Vol. 27. Applied Mathematical Sciences. New York: Springer, 2001.

[13] Frédéric Bouillault et al. «The mortar edge element method in three dimensions: application to magnetostatics». In: *SIAM Journal on Scientific Computing* 24.4 (2003), pp. 1303–1327.

[14] K. Brackebusch, T. Galek and U. van Rienen. *Automated Mode Recognition Algorithm for Accelerating Cavities*. 2014.

[15] Franco Brezzi and Michel Fortin. *Mixed and hybrid finite element methods*. Vol. 15. Springer Science & Business Media, 2012.

[16] Franco Brezzi and L. Donatella Marini. «A three-field domain decomposition method». In: ed. by Alfio Quarteroni et al. Vol. 157. American Mathematical Society, 1994, pp. 27–34.

[17] Annalisa Buffa and Snorre H. Christiansen. «A dual finite element complex on the barycentric refinement». In: *Mathematics of Computation* 76.260 (2007), pp. 1743–1769.

[18] Annalisa Buffa, Martin Costabel and Dongwoo Sheen. «On traces for H(curl,Ω) in Lipschitz domains». In: *Journal of Mathematical Analysis and Applications* 276.2 (2002), pp. 845–867.

[19] Annalisa Buffa, Carlo de Falco and Giancarlo Sangalli. «IsoGeometric Analysis: Stable elements for the 2D Stokes equation». In: *International Journal for Numerical Methods in Fluids* 65.11-12 (2011), pp. 1407–1422.

[20] Annalisa Buffa and Carlotta Giannelli. «Adaptive isogeometric methods with hierarchical splines: error estimator and convergence». In: *Mathematical Models and Methods in Applied Sciences* 26.01 (2016), pp. 1–25.

[21] Annalisa Buffa and Ralf Hiptmair. «Galerkin boundary element methods for electromagnetic scattering». In: *Topics in computational wave propagation*. Ed. by Mark Ainsworth et al. Springer, 2003, pp. 83–124.

[22] Annalisa Buffa and Francesca Rapetti. «A sliding mesh-mortar method for a two-dimensional eddy currents model of electric engines». In: *Mathematical Modelling and Numerical Analysis* (1999).

[23] Annalisa Buffa, Giancarlo Sangalli and Rafael Vázquez. «Isogeometric analysis in electromagnetics: B-splines approximation». In: *Computer Methods in Applied Mechanics and Engineering* 199 (2010), pp. 1143–1152.

[24] Annalisa Buffa, Giancarlo Sangalli and Rafael Vázquez. «Isogeometric methods for computational electromagnetics: B-spline and T-spline discretizations». In: *Journal of Computational Physics* 257, Part B (2013), pp. 1291–1320.

[25] Annalisa Buffa et al. «Isogeometric Discrete Differential Forms in Three Dimensions». In: *SIAM Journal on Numerical Analysis* 49.2 (2011), pp. 818–844.

[26] Annalisa Buffa et al. «Substructuring Methods for Electromagnetic Simulation using Isogeometric Analysis». English. 2017. In preparation.

[27] Elena Bulgarello and Sara Frizziero. «Isogeometric Simulation of the Perfusion Characteristic in the Liver Tissue». Tesi di Laurea Magistrale. Politecnico di Milano, 2014.

[28] Hans-Joachim Bungartz and Michael Griebel. «Sparse grids». In: *Acta Numerica* 13 (2004), pp. 147–269.

[29] Salvatore Caorsi, Paolo Fernandes and Mirco Raffetto. «On the convergence of Galerkin finite element approximations of electromagnetic eigenproblems». In: *SIAM Journal on Numerical Analysis* 38.2 (2000), pp. 580–607.

[30] Dominique Chapelle and Klaus-Jürgen Bathe. «The inf-sup test». In: *Computers & structures* 47.4-5 (1993), pp. 537–545.

[31] Jacopo Corno. «Isogeometric Simulation of Lorentz Detuning in Superconducting Linear Accelerators». Master's Thesis. Milano, Italy: Politecnico di Milano, 2014.

[32] Jacopo Corno et al. «Isogeometric Analysis Simulation of TESLA Cavities Under Uncertainty». In: *Proceedings of the International Conference on Electromagnetics in Advanced Applications (ICEAA) 2015*. Ed. by Roberto D. Graglia. IEEE, Sept. 2015, pp. 1508–1511.

[33] Jacopo Corno et al. «Isogeometric Simulation of Lorentz Detuning in Superconducting Accelerator Cavities». In: *Computer Physics Communications* 201 (Feb. 2016), pp. 1–7. arXiv: `1606.08209`.

[34] J. Austin Cottrell, Thomas Joseph Robert Hughes and Yuri Bazilevs. *Isogeometric Analysis: Toward Integration of CAD and FEA*. Wiley, 2009.

[35] CST AG. *CST STUDIO SUITE 2016*. Darmstadt, 2016.

[36] Jean Delayen. *Low and Intermediate Beta Cavity Design–A Tutorial*. United States. Department of Energy. Office of Energy Research, 2003.

[37] Marta D’Elia and Max Gunzburger. «Coarse-Grid Sampling Interpolatory Methods for Approximating Gaussian Random Fields». In: *SIAM/ASA Journal on Uncertainty Quantification* 1.1 (2013), pp. 270–296.

[38] Jiansong Deng et al. «Polynomial splines over hierarchical T-meshes». In: *Graphical models* 70.4 (2008), pp. 76–86.

[39] Jeroen Deryckere et al. «Stochastic response surface method for studying microphoning and Lorentz detuning of accelerators cavities». In: *ICAP2012: Proceedings of the 11th International Computational Accelerator Physics Conference*. 2012, pp. 158–160.

[40] *DESY’s XFEL Cavity Database*. `http://xfel.desy.de/cavity_database/`.

[41] G Devanz, M Luong and A Mosnier. «Numerical simulations of dynamic Lorentz detuning of SC cavities». In: *EPAC (2002): Proceedings of the 8th European Particle Accelerator Conference*. 2002.

[42] Josef Dick, Frances Y. Kuo and Ian H. Sloan. «High-dimensional integration: the quasi-Monte Carlo way». In: *Acta Numerica* 22 (2013), pp. 133–288.

[43] Tor Dokken, Tom Johan Lyche and Kjell Fredrik Pettersen. «Locally refinable splines over box-partitions». In: *SINTEF Rapport* (2012).

[44] Michael R Dörfel, Bert Jüttler and Bernd Simeon. «Adaptive isogeometric analysis by local h-refinement with T-splines». In: *Computer methods in applied mechanics and engineering* 199.5 (2010), pp. 264–275.

[45] D.A. Edwards and other. «TESLA test facility linac-design report». In: *DESY Print March* (1995), pp. 95–01.

[46] Jens L Eftang and Anthony T Patera. «A port-reduced static condensation reduced basis element method for large component-synthesized structures: approximation and a posteriori error estimation». In: *Advanced Modeling and Simulation in Engineering Sciences* 1.1 (2014), p. 3.

[47] Thomas Flisgen. «Compact state-space models for complex superconducting radio-frequency structures based on model order reduction and concatenation methods». English. PhD thesis. Universität Rostock, 2015.

[48] Thomas Flisgen, Hans-Walther Glock and Ursula van Rienen. «Compact time-domain models of complex RF structures based on the real eigenmodes of segments». In: *Microwave Theory and Techniques, IEEE Transactions on* 61.6 (2013), pp. 2282–2294.

[49] Thomas Flisgen et al. «Scattering parameters of the 3.9 GHz accelerating module in a free-electron laser linac: A rigorous comparison between simulations and measurements». In: *Physical Review Special Topics - Accelerators and Beams* 17.2 (2014), p. 022003.

[50] Diederik R Fokkema, Gerard LG Sleijpen and Henk A Van der Vorst. «Jacobi–Davidson style QR and QZ algorithms for the reduction of matrix pencils». In: *SIAM journal on scientific computing* 20.1 (1998), pp. 94–125.

[51] H. Gassot. «Mechanical Stability of the RF superconducting Cavities». In: *Proceedings of EPAC 2002, Paris, France*. 2002.

[52] Niklas Georg, Malena Kellermann and Alexander Krimm. «Eigenmode Tracking». Ausarbeitung Projektseminar. Darmstadt: Technische Universität Darmstadt, Aug. 2016.

[53] Carlotta Giannelli, Bert Jüttler and Hendrik Speleers. «THB-splines: The truncated basis for hierarchical splines». In: *Computer Aided Geometric Design* 29.7 (2012), pp. 485–498.

[54] Michael B. Giles. «Multilevel Monte Carlo methods». In: *Acta Numerica* 24 (2015), pp. 259–328.

[55] Erion Gjonaj et al. «Coupler Kicks in the Third Harmonic Module for the XFEL». In: *Proceedings of PAC09*. Vancouver, BC, Canada: PAC09, 2009.

[56] Jens Gravesen et al. «Planar Parametrization in Isogeometric Analysis». In: *Mathematical Methods for Curves and Surfaces*. Ed. by Michael Floater et al. Vol. 8177. Lecture Notes in Computer Science. Springer Berlin Heidelberg, 2014, pp. 189–212.

[57] David A Hill. *Electromagnetic fields in cavities: deterministic and statistical theories*. Vol. 35. John Wiley & Sons, 2009.

[58] Thomas Joseph Robert Hughes, J. Austin Cottrell and Yuri Bazilevs. «Isogeometric analysis: CAD, finite elements, NURBS, exact geometry and mesh refinement». In: *Computer Methods in Applied Mechanics and Engineering* 194 (2005), pp. 4135–4195.

[59] Laura Iapichino. «Reduced basis methods for the solution of parametrized PDEs in repetitive and complex networks with application to CFD». PhD thesis. École Polytechnique Fédérale de Lausanne, 2012.

[60] J. Iversen et al. «Development and Design of a RF Measurement Machine for the European XFEL Cavity fabrication». In: *14th SRF Conference, Berlin*. 2009, p. 786.

[61] J. D. Jackson. *Classical Electrodynamics*. 3rd. New York: Wiley and Sons, 1998.

[62] Hughes Thomas JR, Alessandro Reali and Sangalli Giancarlo. «Duality and unified analysis of discrete approximations in structural dynamics and wave propagation: Comparison of p-method finite elements with k-method {NURBS}». In: *Computer Methods in Applied Mechanics and Engineering* 197.49–50 (2008), pp. 4104–4124.

[63] G.R. Kreps, D. Proch and J. Sekutowicz. «Half-cell and dumb-bell frequency testing for the correction of the TESLA cavity length». In: *9th RF Superconductivity Workshop, Santa Fe*. 1999.

[64] G.R. Kreps, J. Sekutowicz and D. Proch. «Tuning of the TESLA Superconducting Cavities and the Measurement of Higher Order Mode Damping». In: *Proc. XVth Conference on Charged Particle Accelerators, Dubna, Russia*. 1996.

[65] RB Lehoucq, DC Sorensen and C Yang. *ARPACK Users' Guide: Solution of Large-Scale Eigenvalue Problems with Implicitly Restarted Arnoldi Methods*. Software, Environments and Tools. Society for Industrial and Applied Mathematics, 1998.

[66] Cong Liu et al. «Numerical Calculation of Eigenmodes in PETRA 7-cell Cavity under precise Consideration of Coupler Structures». In: *12th Int. Computational Accelerator Physics Conf.(ICAP'15), Shanghai, China, 12-16 October 2015*. JACOW, Geneva, Switzerland. 2016, pp. 122–124.

[67] Jun S. Liu. *Monte Carlo Strategies In Scientific Computing*. Harvard University, 2002.

[68] S. H. Lui, H. B. Keller and T. W. C. Kwok. «Homotopy method for the large, sparse, real nonsymmetric eigenvalue problem». In: *SIAM Journal on Matrix Analysis and Applications* 18.2 (Apr. 1997), pp. 312–333.

[69] Bert Masschaele et al. «Design of a Strong Gradient Magnet for the Deflection of Nanoclusters». In: *IEEE Transactions on Applied Superconductivity* 22.3 (June 2012), pp. 3700604–3700604.

[70] *MATLAB and Statistics Toolbox Release 2012b*. Natick, Massachusetts: The MathWorks Inc.

[71] Peter Monk. *Finite Element Methods for Maxwell's Equations*. Oxford: Oxford University Press, 2003.

[72] Wolfgang Müller. *Private correspondence*.

[73] Dang Manh Nguyen, Jens Gravesen and Anton Evgrafov. «Isogeometric analysis and shape optimization in electromagnetism». PhD thesis. 2012.

[74] Jorge Nocedal and Steve J. Wright. *Numerical optimization*. 2nd ed. Springer Series in Operations Research and Financial Engineering. New York: Springer, 2006.

[75] Erich Novak and Klaus Ritter. «High dimensional integration of smooth functions over cubes». In: *Numerische Mathematik* 75.1 (1996), pp. 79–97.

[76] Erich Novak and Klaus Ritter. «Simple cubature formulas with high polynomial exactness». In: *Constructive approximation* 15.4 (1999), pp. 499–522.

[77] *nurbs package*. `https://octave.sourceforge.io/nurbs/`.

[78] Hasan Padamsee, Jens Knobloch and Tom Hays. *RF Superconductivity for Accelerators*. Wiley, 2008.

[79] Andreas Pels and Jacopo Corno et al. «Optimization of a Stern-Gerlach Magnet by Magnetic Field-Circuit Coupling and Isogeometric Analysis». English. In: *IEEE Transactions on Magnetics* 51.12 (July 2015).

[80] Andreas Pels et al. *Optimization of a Stern-Gerlach Magnet by Magnetic Field-Circuit Coupling and Isogeometric Analysis*. Ed. by David A. Lowther. Montréal, Canada: International Compumag Society, June 2015.

[81] Nicolas Pichoff. «Beam dynamics basics in RF linacs». In: *CERN* 99.12 (1999), p. 145.

[82] Nicolas Pichoff. «Introduction to RF linear accelerators». In: *CERN Accelerator School and DESY Zeuthen: Accelerator Physics*. 2005, pp. 105–128.

[83] Les Piegl and Wayne Tiller. *The NURBS Book*. 2nd ed. Springer, 1997.

[84] Michael JD Powell. «The BOBYQA algorithm for bound constrained optimization without derivatives». In: *Cambridge NA Report NA2009/06, University of Cambridge, Cambridge* (2009).

[85] Alfio Quarteroni and Alberto Valli. *Domain Decomposition Methods for Partial Differential Equations*. Numerical Mathematics and Scientific Computation. Oxford: Oxford University Press, 1999.

[86] Alastair I. M. Rae. *Quantum Mechanics*. 4th ed. Bristol and Philadelphia: Institute of Physics, 2002.

[87] Christian Schmidt et al. «Comparison of Techniques for Uncertainty Quantification of Superconducting Radio Frequency Cavities». In: *Proceedings of the International Conference on Electromagnetics in Advanced Applications (ICEAA) 2014*. Ed. by Roberto D. Graglia. IEEE, Aug. 2014, pp. 117–120.

[88] Ute Schreiber and Ursula van Rienen. «Coupled Calculation of Electromagnetic Fields and Mechanical Deformation». In: *Scientific Computing in Electrical Engineering SCEE 2004*. Ed. by Angelo Marcello Anile, Giuseppe Alì and Giovanni Mascali. Mathematics in Industry 9. Berlin, Germany: Springer, 2006.

[89] M. A. Scott et al. *Isogeometric boundary element analysis using unstructured T-splines*. ICES Report 12-23. The Institute for Computational Engineering and Sciences, The University of Texas at Austin, June 2012.

[90] Thomas W. Sederberg et al. «T-splines and T-NURCCs». In: *ACM Trans. Graph.* 22.3 (July 2003), pp. 477–484.

[91] Jacek Sekutowicz, Chen Yinghua and Wey Yixiang. «A different tuning method for accelerating cavities». In: *Workshop on RF Superconductivity. KEK, Tsukuba*. 1989, pp. 849–857.

[92] Waldemar Singer et al. «Preparation phase for 1.3 GHz cavity production of the European XFEL». In: *IPAC* 10 (2010), pp. 23–28.

[93] *Superconducting Darmstadt Electron Linear Accelerator S-DALINAC*. `http://www.ikp.tu-darmstadt.de/sdalinac_ikp/`.

[94] R. Vázquez. «A new design for the implementation of isogeometric analysis in Octave and Matlab: GeoPDEs 3.0». In: *Computers & Mathematics with Applications* 72.3 (2016), pp. 523–554.

[95] A.-V. Vuong et al. «A hierarchical approach to adaptive local refinement in isogeometric analysis». In: *Computer Methods in Applied Mechanics and Engineering* 200.49–52 (2011), pp. 3554–3567.

[96] Thomas P. Wangler. *RF Linear Accelerators*. Physics Textbook. Wiley, 2008.

[97] Rainer Wanzenberg. *Monopole, dipole and quadrupole passbands of the TESLA 9-cell cavity*. Tech. rep. 2001.

[98] Thomas Weiland. «On the unique numerical solution of Maxwellian eigenvalue problems in three dimensions». In: *Particle Accelerators* 17.227–242 (1985).

[99] IG Wilson, CW Schramm and JP Kinzer. «High Q resonant cavities for microwave testing». In: *Bell System Technical Journal* 25.3 (1946), pp. 408–434.

[100] Dongbin Xiu. *Numerical Methods for Stochastic Computations: A Spectral Method Approach*. Princeton University Press, 2010.

[101] E. Zaplatin et al. «Lorentz Force Detuning Analysis for Low-Loss, Reentrant, and Half-Reentrant Superconducting RF Cavities». In: *Proceedings of LINAC 2006, Knoxville, Tennessee USA*. 2006, pp. 734–736.

Acknowledgements

Finding rhymes is becoming quite hard,
but I do have to send my regards.
So this is for you,
without further ado:
many thanks from this level one bard.

This work was supported by the "Excellence Initiative" of the German Federal and State Governments and the Graduate School of Computational Engineering at Technische Universität Darmstadt.

I would also like to thank DESY for providing us access to their cavity database and for granting us the possibility to present our results.

On a more personal note I would like to thank my supervisors Prof. Carlo de Falco and Prof. Sebastian Schöps. We started collaborating during my Master's thesis and, since then, their help and advice has been invaluable. The co-supervision agreement they put in place allowed me to live a great experience both professionally and personally and I will forever be grateful.

Much gratitude also goes to all those people who provided me with advice and suggestions that were fundamental for the successful completion of this work: Prof. Herbert De Gersem, Dr.-Ing. Wolfgang Ackermann and Dr. phil. nat. Wolfgang Müller from TU Darmstadt, and Prof. Annalisa Buffa and Dr. Rafael Vázquez from EPFL. I am also grateful for the possibility to work together with Niklas Georg on the eigenvalue tracking method he developed together with Malena Kellermann and Alexander Krimm, and for the collaboration with Andreas Pels and Zeger Bontinck on the Stern-Gerlach magnet optimisation (they also managed to endure my presence in the office during these years so that needs to be acknowledged too).

Finally I would like to thank my Temflepuff friends at the Graduate School for the lunches, the jokes, the beers and the games together. They have made my stay in Darmstadt so much more enjoyable and fun than I would have ever expected. Please try not to gain too much German points. It is not a good thing. Really.

Visto che si tratta di un PhD congiunto (e visto che i ringraziamenti sono il capitolo più letto di ogni tesi che si rispetti) mi sembra legittimo cambiare lingua per aggiungere qualche altro commento.

Un pensiero va agli amici del laboratorio del sesto piano al MOX che mi hanno riaccolto al Politecnico e insieme ai quali abbiamo combattuto fiere battaglie sindacali per ottenere un'area pranzo migliore. Se l'intero campus Bonardi verrà rinnovato lo si deve anche a noi.

Ringrazio gli amici di sempre che, seppur a distanza, hanno condiviso con me questi anni e un augurio speciale va a Giuliana e Marco che presto aggiungeranno un nuovo membro al nostro gruppo. E non dimentico Tommaso che è stato così premuroso nei miei confronti da trasferirsi in Germania per farmi compagnia. Grazie per le gite ad Hanau, i pranzi luculliani e le discussioni su D&D.

Infine un grazie di cuore a Giulia, che, nonostante la distanza e le difficoltà, ha accettato di essere così scortese da farmi da compagna. Le lunghe telefonate, le tue visite, e il tuo costante sostegno sono stati e sono più importanti di quanto do a vedere.

Chiudo con un enorme grazie alla mia famiglia che mi ha supportato (o sopportato?) per tutti questi anni e che ha vissuto con emozione la mia partenza per questa avventura. Se sono arrivato a questo traguardo lo si deve soprattutto a voi che mi avete cresciuto e fatto diventare chi sono oggi.

Jacopo Corno - Curriculum Vitae

Graduate School of Compuational Engineering
Dolivostraße 15
DA-64293 Darmstadt, Germany.
Phone: +49 6151 16-76877
Fax: +49 6151 16-4414
email: corno@gsc.tu-darmstadt.de
URL: `http://www.graduate-school-ce.de/index.php?id=619`

Anagraphical Data

Born: December 16, 1988 - Milano, Italy
Nationality: Italian

Current position

Wissenschaftlicher Mitarbeiter	Graduate School of Computational Engineering and Institut für Theorie Elektromagnetischer Felder, Technische Universität Darmstadt, Darmstadt, Germany.

Areas of specialisation

Numerical Mathematics, Isogeometric Analysis, Computational Electromagnetics, Particle Accelerators.

Education

Dec. 2013	M.Sc. in Mathematical Engineering, Politecnico di Milano.
Sept. 2010	B.Sc. in Mathematical Engineering, Politecnico di Milano.

Publications

Nov. 2017	Z. Bontinck, J. Corno, et al., *Recent Advances of Isogeometric Analysis in Computational Electromagnetics*, International Compumag Society, 24 (3), 5–16, 2017.

Sept. 2017	Zeger Bontinck, Jacopo Corno, Sebastian Schöps, Herbert De Gersem, *Isogeometric Analysis and Harmonic Stator-Rotor Coupling for Simulating Electric Machines*, Computer Methods in Applied Mechanics and Engineering, Under Review.
Dec. 2015	J. Corno, C. de Falco, H. De Gersem, S. Schöps, *Isogeometric Simulation of Lorentz Detuning in Superconducting Accelerator Cavities*, Computational Physiscs Communication, 201, 1–7, 2016.
Sept. 2015	J. Corno, C. de Falco, H. De Gersem, S. Schöps, *Isogeometric Analysis simulation of TESLA cavities under uncertainty*, Electromagnetics in Advanced Applications (ICEAA), 2015 International Conference on, pp.1508-1511, 7-11 Sept. 2015, `10.1109/ICEAA.2015.7297375`.
Aug. 2015	A. Pels, Z. Bontinck, J. Corno, H. De Gersem, and S. Schöps, *Optimization of a Stern-Gerlach Magnet by Magnetic Field-Circuit Coupling and Isogeometric Analysis*, IEEE Transaction on Magnetics, 2015, `10.1109/TMAG.2015.2462806`.

Conference Talks and Seminars

Feb. 2017	J. Corno, C. de Falco, S. Schöps, *Domain Substructuring using IGA and FEM with Application to RF Cavity Simulation*, 24th International Conference on Domain Decomposition, Svalbard, Norway
Jun. 2016	J. Corno, C. de Falco, S. Schöps, *Isogeometric State Concatenation Method for Reduced Order Simulation of Complex Accelerator Cavities*, 19th European Conference on Mathematics for Industry ECMI 2016, Santiago de Compostela, Spain
Apr. 2016	J. Corno, C. de Falco, H. De Gersem, S. Schöps, *Isogeometric Analysis Simulation of Accelerator Cavities*, "A day in Applied Mathematics" First Joint Meeting of the PoliMi and SISSA Student Chapters of SIAM, SISSA, Trieste, Italy
Apr. 2016	J. Corno, C. de Falco, H. De Gersem, S. Schöps, *An Isogeometric Framework for the Optimization of Accelerator Cavities*, 10th International Symposium on Electric and Magnetic Fields (EMF 2016), Lyon, France.
Nov. 2015	J. Corno, C. de Falco, *GNU-Octave and OdePkg*, Seminar, Dipartimento di Informatica, Universitá degli Studi di Verona, Verona, Italy.
Sept. 2015	J. Corno, C. de Falco, H. De Gersem, S. Schöps, *Isogeometric Analysis Simulation of TESLA Cavities Under Uncertainty*, International Conference on Electromagnetics in Advanced Applications (ICEAA) 2015, Torino, Italy.
Jul 2014	J. Corno, C. de Falco, H. De Gersem, S. Schöps, *High Order Isogeometric Simulation of Lorentz Detuning in SC Accelerator Cavities*, Seminar at the Felix Klein Zentrum für Mathematik, Technische Universität Kaiserslautern, Kaiserslautern, Germany.

Jun 2014	J. Corno, C. de Falco, H. De Gersem, S. Schöps, *High Order Isogeometric Simulation of Lorentz Detuning in Superconducting Accelerator Cavities*, International Conference on Advanced COmputational Methods in ENgineering (ACOMEN) 2014, Gent, Belgium.
Jul 2014	J. Corno, C. de Falco, H. De Gersem, S. Schöps, *Isogeometric Simulation of Lorentz Detuning in Superconducting Accelerator Cavities*, Conference on Electromagnetic Field Computation (CEFC) 2014, Annecy, France.

Teaching

Mar. 2016 - Jul. 2016	*Calcolo Numerico per Ingegneria Biomedica*, Teaching Assistant.
Mar. 2016 - Jul. 2016	*Fondamenti di Calcolo Numerico per Ingegneria Elettronica*, Teaching Assistant.
Oct. 2015 - Jan. 2016	*Architectural Geometry - Parametric Geometry for Architectural Shape*, Teaching Assistant.

Other Activities

May 2016 - Aug. 2016	**Mentor** for the **Google Summer of Code** project *Exponential Integrators* by Chiara Segala (http://gsoc2016exponentialintegrators.blogspot.it/).
May 2016 - Aug. 2016	**Mentor** for the **Google Summer of Code** project *ode15s in core-Octave* by Francesco Faccio (gsoc2016ode15s.blogspot.it/).
Apr. 2015 - Present	**Maintainer** of Octave *odepkg* (octave.sourceforge.net/odepkg/).
Aug. 2014 - Present	Participation to DFG project *Uncertainty quantification techniques and stochastic models for superconducting radio frequency cavities* (gepris.dfg.de/gepris/projekt/262959891).
Jun. 2014 - Aug. 2014	Participation to **ESA *Summer of Code in Space 2014*** with the project *MATLAB-compatible ODE solvers in core-Octave*.
Sept. 2013 - Present	Contribution to **Octave nurbs package** (octave.sourceforge.net/nurbs/).
Sept. 2013 - Present	Contribution to **GeoPDEs** project (geopdes.apnetwork.it/).